Synthesis and Characterization of II-VI Quantum Dots and Their Assembly into 3D Quantum Dot Superlattices

by

Christopher Bruce Murray

B. S. Chemistry
Saint Mary's University, Halifax N. S. 1989

Submitted to the Department of Chemistry
in Partial Fulfillment of the Requirements
for the Degree of

DOCTOR OF PHILOSOPHY

at the

MASSACHUSETTS INSTITUTE OF TECHNOLOGY

September 1995

Signature of the Author _____
Department of Chemistry
August 17, 1995

Certified by _____
Moungi G. Bawendi
Associate Professor of Chemistry
Thesis Supervisor

Accepted by _____
Dietmar Seyferth
Chairman, Department Committee on Graduate Studies

This thesis has been examined by a commitee of the department of chemistry as follows:

Professor Sylvia T. Ceyer_____
Chairperson

Professor Moungi G. Bawendi_____
Thesis Supervisor

Professor Robert J. Silbey_____

For The Family.

SYNTHESIS AND CHARACTERIZATION OF II-VI QUANTUM DOTS AND THEIR ASSEMBLY INTO 3D QUANTUM DOT SUPERLATTICES

by
CHRISTOPHER BRUCE MURRAY

ABSTRACT

Chapter 1

A general introduction to the emerging field of nanostructured materials is presented highlighting the importance of their small volume and huge surface area. The need for high quality model systems in all areas of nanostructured materials is stressed. Semiconductor nanocrystallites (quantum dots) and 3D nanocrystallite superlattices are presented as systems of value both for fundamental physics and for the production of functional materials. Examples of the control over both the individual crystallite structure and that of the assembled superstructure are provided. Important developments in the synthesis of II-VI nanocrystallites that have contributed to the development of this control are reviewed.

Chapter 2

A simple route to the production of nearly-monodisperse CdE (E = S, Se, Te) semiconductor nanocrystallites is presented. Crystallites from ~17 to 150Å in diameter with uniform size, shape, consistent crystal structure and surface derivatization are prepared in a single reaction. The synthesis is based on the pyrolysis of organometallic reagents by injection into a hot coordinating solvent. This provides temporally discrete nucleation and permits controlled growth of macroscopic quantities of the nanocrystallites. Size selective precipitation of crystallites from portions of the growth solution isolates samples monodisperse to the limit of atomic roughness ($\leq$4% rms in diameter).

Chapter 3

The room temperature optical properties of II-VI semiconductor nanocrystallites are displayed. A monodisperse series of CdSe nanocrystallite samples reveals the evolution of optical absorption spectra as the average crystallite diameter is increased one lattice plane at a time. Band-edge and deep-trap emission are mapped out as a function of crystallite size. Measurements show that room temperature quantum yield for band edge emission approach 0.2 in high quality samples. Spectra sharpen significantly at low temperature (10K) and the quantum yield approaches unity.

Chapter 4

A detailed structural model of the semiconductor nanocrystallite core is developed by combining the results of several independent structural probes. The results of transmission electron microscopy (TEM) and extended X-ray absorption fine structure (EXAFS) studies are combined through simple computer modeling to fit simultaneously the experimental wide angle X-ray scattering (WAXS) and small angle X-ray (SAXS) patterns. Crystallites are shown to be fragments of the bulk lattice with a relaxed surface layer. The importance of crystallite shape, internal defects, and surface relaxation are investigated. We find that structural evolution of CdSe is rapid and is dominated by the local highly directional nature of polar covalent bonding. Little evidence for an isotropic lattice contraction is found.

Chapter 5

Room temperature ^{31}P magic angle spinning (MAS) nuclear magnetic resonance (NMR) is used to study the phosphine chalcogenide species coordinating the surface of CdSe nanocrystallites. Two surface species are identified: trioctylphosphine oxide (TOPO) and trioctylphoshine selenide (TOPSe). The chemical removal of TOPSe ligands by reaction with an excess of TOPO provides nanocrystallites passivated exclusively with TOPO. A double resonance experiment (^{31}P and ^{77}Se) characterizes the TOPSe species. Quantitative studies indicate coordination of nearly all surface cadmium atoms producing a close packed monolayer of trialkylphosphine chalcogenide on the surface of the crystallites. Methods are developed for the facile exchange of the native surface passivation for a diverse array of chemical functionalities including both Lewis bases coordinating Cd sites and Lewis acid caps for surface Se sites. Surface derivatization is shown to have a profound effect on nanocrystallite luminescence, with efficient surface passivation essential for high quantum yields.

Chapter 6

Close packed quantum dot (QD) solids present tremendous potential for new collective physical phenomena. A general methodology for the production of QD glasses by controlled evaporation of stable QD dispersions is outlined. Specific methods produce QD glasses as single monolithic structures and as uniform optical films. Evidence of new collective optical phenomena is observed in a red shift of the luminescence from the close packed films. A model of average structure in the glasses is developed by a combination of electron microscopy and small angle X-ray scattering studies. Methods for controlling the chemical nature and dimension of the inter particle spacing layer are demonstrated. Fundamentally new inorganic superstructures are prepared by self-organizing surface capped crystallites and then removing the capping groups. Close-packed solid films of crystallites are cross linked with bifunctional ligands to produce thermally and mechanically robust close-packed, nanocrystalline thin films.

The critical parameters in the transition form short-range to long-range order are identified: glassy solids are obtained if the particles maintain a repulsion as the dispersion is concentrated, conversely a gently increasing net attraction during evaporation allows crystallites to self-organize into 3D superlattices.

Conditions for self-organization of CdSe nanocrystallites into 3D QD superlattices (colloidal crystals) are optimized. The size and spacing of the crystallites are controlled with near-atomic precision. Fcc superlattices are prepared in two distinct morphologies, faceted colloidal crystals and oriented epitaxial thin films. Epitaxial assembly has the added benefit that both the superlattice and the individual crystallites can be oriented in the lab frame.

Thesis Supervisor: Dr. Moungi G. Bawendi

TABLE OF CONTENTS

Chapter 1

General Introduction

1.0 Nanocrystallites and Mesoscopic Phenomena

When atoms or molecules organize into condensed systems, new collective phenomena develop. These cooperative interactions produce the physical and electronic properties we recognize as characteristic of bulk materials. Nanometer sized crystals are a "mesoscopic" or intermediate state of matter that display properties present in neither bulk nor molecular systems.[1] These structures do not have enough atoms to exhibit full delocalized properties and thus their physical and electronic properties are strongly dependent on size (number of atoms).[2]

Many important physical phenomena in both organic and inorganic materials have natural length scales between 1 and 100 nm (10^2 to 10^7 atoms). The prefix *nano* has become synonymous with the development of new mesoscopic phenomena. Efforts to explore complex structures on the nanometer size scale unite the frontiers of chemistry, physics and engineering. It is in the design and characterization of advanced materials that the importance of new interdisciplinary studies may first be realized.[3] Studies of nanometer sized semiconductors,[4] metals,[5] and refractories (nanoceramics)[6] provide powerful examples of how control of particle size can optimize material performance.

As the size of a structure decreases, the percentage of the remaining atoms residing on the surface of the crystallite increases dramatically. These atoms experience coordination environments and display chemical reactivities dramatically different from both the bulk and extended, macroscopic surfaces. It is the interfacial properties of nanostructured materials that have been most effectively exploited. Catalysts for many important industrial processes are nanometer sized metal particles and nanoporous zeolites. Efforts continue to enhance efficiency and specificity of these catalysts by tailoring their structure and morphology at an atomic level.[7] The performance of ceramics and composite materials is determined by interfacial phenomena and physical

interactions between particles (adhesion and packing) rather than the internal structure of each particle.[6] Thus control of particle structure on nanometer size scales is already of importance in advanced materials research. Novel mesoscopic phenomena and the increasing role of the surface combine to endow nanostructured materials with properties tunable by precisely controlling particle size and surface chemistry. Economically important thin films and composite materials have critical structural features on nanometer length scales. Precise control of structure is inherent to the optimization of their performance.

The ability to engineer materials and assemble devices on the nanometer size scale are goals in fields as diverse as opto-electronics,[2] catalysis,[5] ceramics,[6] and magnetic storage.[8] Engineering at the nanometer scale is the search to find how many atoms it takes to get the job done efficiently. The job may be switching the path of a laser pulse, catalyzing a chemical reaction, protecting valuable surfaces from heat and shock with resistant coatings, or storing one bit of information. Each area of study has its own specific requirements and yet all face several common challenges. Size dependent materials properties must be clearly mapped for systems of interest if issues of efficiency and utility are addressed.

The mapping of size dependent nanocrystallite properties is our general goal and that of many other researchers.[1, 2, 6, 8] To contribute to this emerging field of nanostructured materials we have attempted to fully develop a single model system, cadmium selenide (CdSe). In this way we hope to show the benefits of a concerted synthetic, spectroscopic, and structural investigation. We have developed methods for the preparation and systematic characterization of high quality nanocrystalline systems. To distinguish true size dependent evolution from simple sample inhomogeneities and defects, we produced a series of homologous samples spanning the size range of interest. When samples are nearly monodisperse the ensemble average of the properties observed is representative of the properties of each individual crystallite. We systematically synthesize and characterize samples with a combination of chemical and structural probes. We unite the results of these independent probes in simple computer models, and thus assure a self-consistent description of the material. General procedures have allowed

us to describe the structure and properties of these mesoscopic structures with a precision comparable to many conventional macromolecules. Once we have established control over the individual nanocrystallites and their properties, we assemble these tailored nanocrystalline building blocks into fundamentally new materials.

To produce functional materials and devices, nanocrystals must be organized into solid superstructures while maintaining and enhancing their novel mesoscopic properties. In addition to this general requirement there are formidable practical constraints. Materials must display mesoscopic phenomena at or near room temperature and be robust both chemically and mechanically. In addition, materials must be produced by cost effective methods. These challenges must be met to transform scientific curiosities into technological advances. We combine the versatility and precision of organometallic synthesis with the established methodology of colloidal self-organization to address many of these practical issues.

1.1 Semiconductor Nanocrystallites (Quantum Dots)

Studies of nanometer size semiconductor structures allow us to explore new physical phenomena reaching beyond the frontiers of conventional technology.[2,3] There is a pressing need to understand the ultimate limits of miniaturization in electronic materials. Mass fabrication techniques employing efficient combinations of lithography, deposition, and etching are pushing toward structural features on the nanometer size scale. Each generation in miniaturization of electronic devices has, to date, been a linear reduction of the existing technology. Fundamental limits for this simple extrapolation are on the horizon.

When the natural delocalization length of electronic excitations, the Bohr radius, is larger than the volume available, the bulk band structure breaks down. Nanocrystallites of metals open up band gaps[1] and semiconductor energy levels shift to resemble bulk insulators.[2] With dimension comparable to the wavelength of an electron, quantum mechanical phenomena negligible in bulk materials come to dominate electronic and optical properties. Powerful techniques like molecular beam epitaxy (MBE) and electron beam and X-ray lithography allow the fabrication of many structures displaying mesoscopic optical and electronic properties. Within these structures, excitations experience spatial confinement in one dimension (quantum wells), two dimensions (quantum wires), and ultimately in all three dimensions (quantum dots, QDs). Esaki provides a review of nanofabricated quantum well structures.[9] MBE allows the fabrication of structures with near atomic resolution, precise to the limit of interfacial roughness. Although these materials and devices display fascinating physical effects, the cost prohibits commercial production. Inexpensive fabrication techniques that allow us to capture some of these novel mesoscopic properties are essential for practical materials.

Figure 1.1A depicts a quantum dot as an excised fragment of the bulk semiconductor lattice. An internal crystalline core is surrounded by atoms of low coordination. Figure 1.1B presents the electronic ramifications of spatial confinement. The HOMO-LUMO gap shifts to higher energy and discrete electronic states emerge from

the continuum of the bulk bands.[2] This blue shift is referred to as quantum confinement. In addition to these delocalized states there are many sources of localized energy levels. Shallow and deep trap states must be understood and controlled in both bulk and nanocrystalline material.

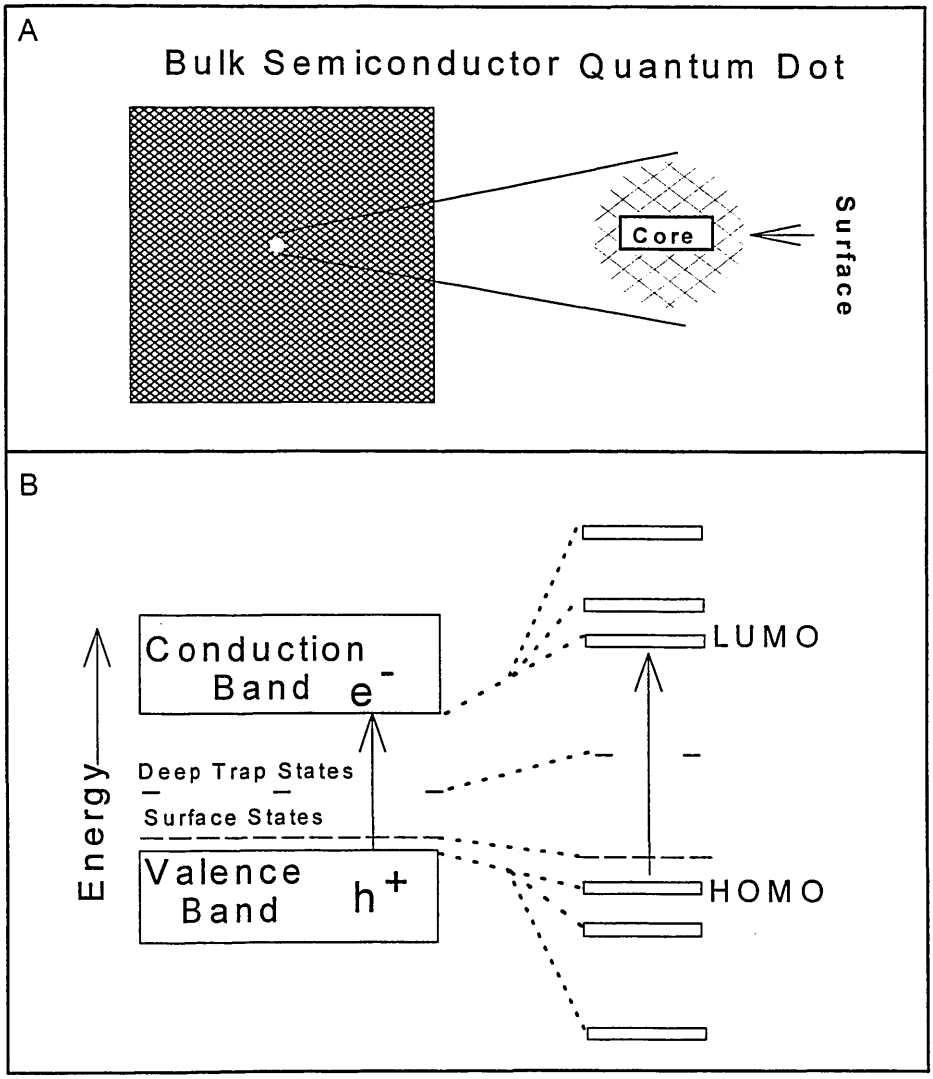

FIG. 1.1A Cartoon depicts a quantum dot as an excised fragment of the bulk lattice with a crystalline core and low coordination atoms (surface).

FIG. 1.1B Cartoon presents the energetic effects of the spatial confinement of excitations in the quantum dot (after reference 2).

Semiconductor nanocrystallites (QDs) have been the subject of intense study as models of the evolution of material properties with size and as promising opto-electronic materials in their own right.[3] Electronic states are strongly dependent on the size of the structure and are modeled in zero'th order as "particle-in-a-spherical box" quantum mechanical states. A cartoon shows our box, a chemically synthesized semiconductor nanocrystallite, (figure 1.2A). This CdSe QD has a crystalline core throughout which an excitation can be delocalized. A monolayer of CdSe is depicted as relaxed with surface atoms partially rehybridizing to minimize the surface free energy. A close packed monolayer of ambiphilic trioctylphosphine chalcogenide molecules assembles on the surface. This surface "capping layer" has several critical roles. Chemical bonding of the head group to the surface permits high luminescence efficiency by passivating a manifold of surface states that would act as non-radiative pathways. Organic tails provide an insulating layer that maintains the electronic isolation of the particles and sterically stabilizes dispersions of the crystallites in a variety of solvents and polymer matrixes.

In figure 1.2B a high resolution transmission electron (HRTEM) micrograph shows a "real box", a 130Å diameter CdSe nanocrystallite. The crystalline core displays the characteristic hexagonal pattern of a wurtzite crystal structure viewed along the <002> axis. The relaxed surface and the capping groups provide little contrast. This crystallite is just larger than the 120Å Bohr diameter of an exciton and exhibits electronic properties approaching the bulk limit. How do the discrete properties of atoms and molecules merge into the collective phenomena of bulk solids as this structure is built one plane of atoms at a time? As chemists, we have chosen to demonstrate the simplicity and efficiency of chemical synthesis in answering this question.

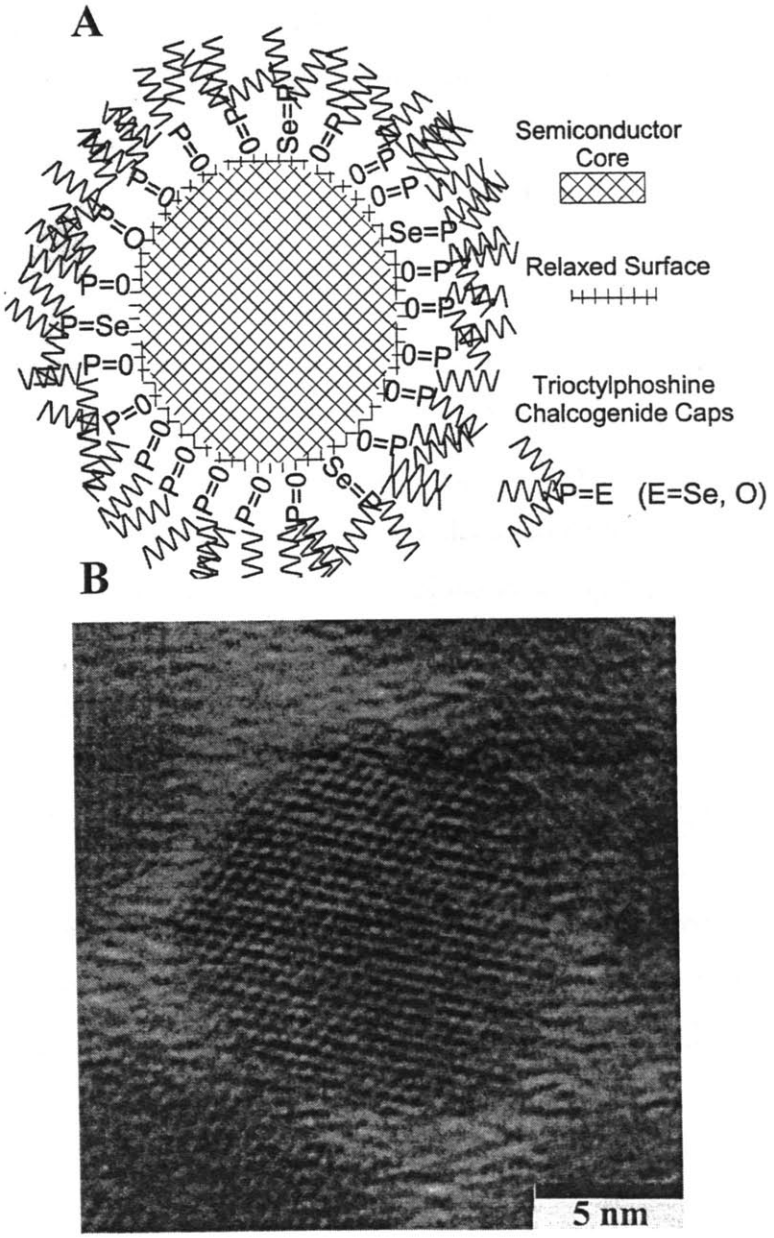

FIG. 1.2A Cartoon depicts a chemically synthesized CdSe nanocrystallite with a crystalline core and a relaxed surface coordinated by a close packed monolayer of trioctylphoshine chalcogenide capping groups.

FIG. 1.2B HRTEM of a 130Å diameter CdSe nanocrystallite viewed along the <002> wurtzite axis.

Figure 1.3A shows the evolution of the optical absorbance of CdSe nanocrystallites as we increase the average size by one lattice plane at a time. We achieve near-atomic precision by combining organometallic chemistry and classic principles of colloid science. Figure 1.3B shows an enlarged view of every fifth sample to emphasize the sharp structure observed in each sample. We observe this dramatic quantum mechanical phenomena with a bench-top spectrometer at ambient temperature and pressure. The series of samples in panel (B) is representative of the material we can isolate from a single 4 hour preparation.[10]

Bulk CdSe is black with an absorption edge at ~716 nm. Its absorbance increases smoothly throughout the visible (similar to the 150Å spectrum). Quantum confinement concentrates the bulk oscillator strength in a few discrete transitions. On average, in the bulk, each photo-excited electron hole pair is delocalized over a region ~120Å in diameter. If however we divide the same volume of semiconductor into 216 particles each 20Å in diameter, this material could support 216 isolated excitations. This enormous increase in the absorbance could be critical in optical applications where the photon penetration depths and physical confinement of photons are important (thin film applications, nearfield optics). As seen in figure 1.3, the oscillator strength is restricted to narrow spectral regions that are tunable with particle size.

Each sharp optical resonance can be described with labels analogous to atomic states and thus quantum dots are referred to as "artificial atoms".[13] The electronic states are delocalized over the volume of the particle and are highly polarizable. Coupling these highly polarizable states to external electric or magnetic fields is an active area of investigation.[14,15] This unique combination of strong discrete transitions and highly polarizable electronic states raises the potential of significant nonlinear optical activity.[16]

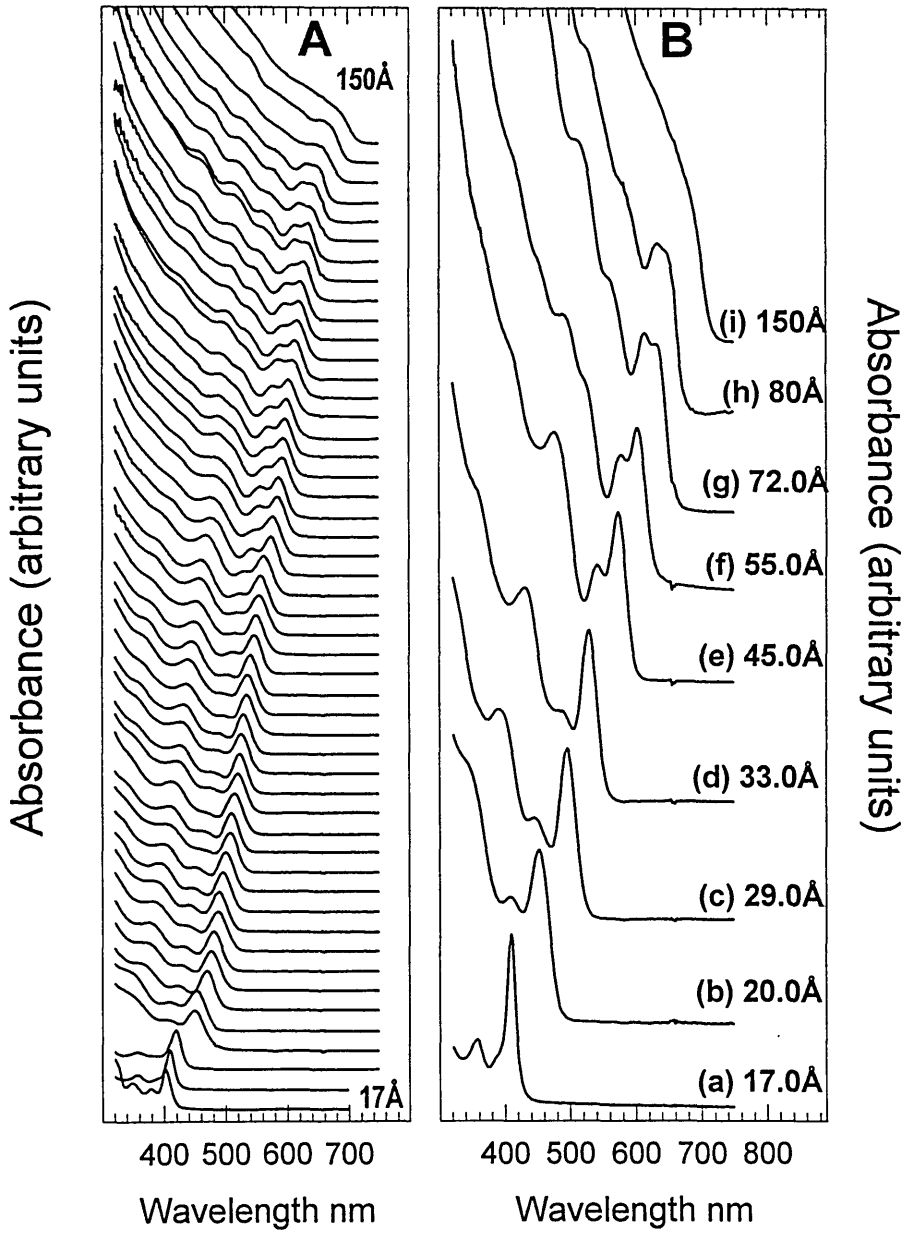

FIG. 1.3A Room temperature optical absorbance spectra of CdSe nanocrystallites from ~17Å up to 150Å in diameter in increments of ~1 atomic plane.

FIG. 1.3B Room temperature optical absorbance spectra represent the range of material we isolate in a single reaction.

In addition to their striking absorption features these crystallites are robust inorganic chromophores displaying photo-emission efficiencies approaching 20% at room temperature. With high quantum yields these particles potentially provide extraordinarily high densities of emitters. We can smoothly tune the emission wavelength throughout the visible by selection of crystallite size. Electroluminescent devices have been developed with these CdSe nanocrystals as chromophores.[11,12]

Isolated nanocrystallites allow the exploration of fascinating mesoscopic phenomena, but they do not, in themselves, constitute a device or a functional material. To exploit their properties we must rationally assemble the individual crystallites into extended solid state structures that preserve and indeed enhance desirable properties. Dramatic enhancements in the optical density (concentration of oscillator strength) are lost in dilute dispersions in host matrixes. Significant enhancements in optical nonlinearities have been however predicted for 3D close packed arrays of quantum dots.[17] We direct our attention to the assembly of close packed solids containing only individual nanocrystallites and their intimate capping shell.

The phenomenology of organizing colloidal particles into close-packed "colloidal crystals" has been extensively studied in both natural and synthetic systems. Combining the general methodology of colloidal self-organization with the versatility of synthetic chemistry results in a straightforward route for the production of 3D quantum dot superlattices.[18] Figure 1.4(A) shows a cartoon of the <101> projection through a face centered cubic (fcc) superlattice of quantum dots. We can tune interparticle spacing in the close-packed monolayer by controlling the steric bulk of the tail groups. Figure 1.4(B) shows a HRTEM image of the <101> projection of a 3D superlattice of quantum dots we have assembled. The internal lattice of each 48Å diameter CdSe nanocrystallite is visible along with the greater periodicity of the superlattice. Figure 1.5 shows a HRTEM image of a portion of a <111> oriented epitaxial film of 64Å diameter CdSe nanocrystallites organized expitaxially on a carbon substrate. The inset small angle electron diffraction pattern displays the lateral perfection of the 2 micron diameter region

surrounding the real space image. This epitaxial domain is coherent over a 100 μm^2 area with a thickness of ~4 planes. Film roughness is limited to steps of 1 particle diameter. We use the epitaxial assembly to control the orientation of both superlattice and the individual crystallites. The external dimensions of this array are comparable to those of conventional micro-machining, while the internal feature size of the individual dots, at ~5 nm, are a factor of 100 smaller than conventional feature sizes. We organize these ordered superlattices by deposition from common solvents. All that is required are monodisperse nanocrystals, a pipette and a flat substrate.

Researchers efficiently employ variations in material composition to engineer the electronic properties of semiconductor materials (ternaries, dopants, etc.). The controlled production of quantum dot solids makes nanocrystallite size, surface derivatization, spacing, and the symmetry and orientation of the superstructure powerful and independent parameters with which to optimize material performance.

This thesis discusses how we synthesize the individual crystallites monodisperse to atomic roughness and how we facilitate their self-organization into extended 3D superlattices with near atomic precision. Building with artificial atoms represents an entirely new class of advanced materials research uniting macromolecular chemistry and low dimensional opto-electronics.

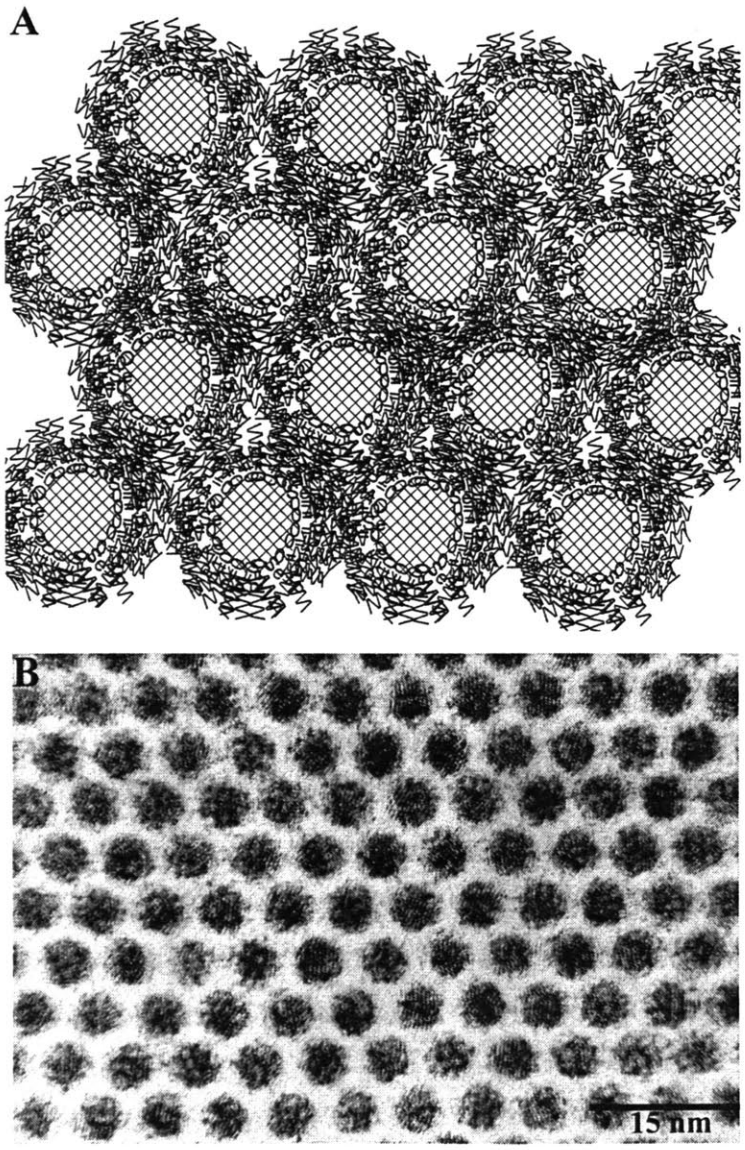

FIG. 1.4A Cartoon of a <101> projection though an fcc superlattice of surface derivatized nanocrystallites.

FIG. 1.4B HRTEM image of an fcc superlattice of 48Å diameter nanocrystallites viewed along the <101> axis. The internal lattice of each crystallite and the periodicity of the superlattice are seen.

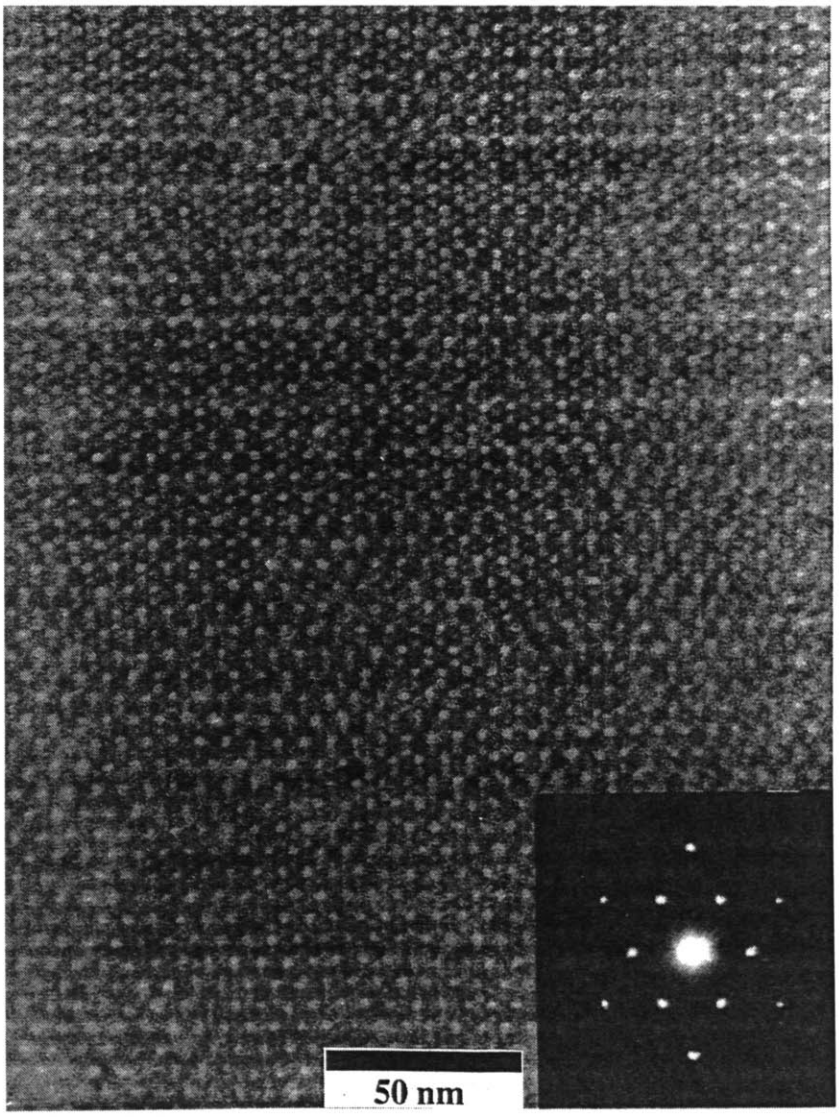

FIG. 1.5 HRTEM image of an fcc superlattice of 64Å CdSe nanocrystallites viewed along the <111> axis of the superlattice. Inset is a small angle electron diffraction pattern of a 2 μm area of the same superlattice.

1.2 Review of Quantum Dot Preparations

The availability of high quality samples has been the limiting factor in mapping out structure property relations in semiconductor nanocrystallites. Significant resources have been directed at the production of uniform semiconductor nanocrystallites. Many materials have been explored but the II-VI semiconductors CdS and CdSe are the most widely studied models of quantum confinement effects in direct gap semiconductors. Indirect gap studies have focused largely on Si[19,20] with recent progress in the production of GaP.[21] With a simple band structure, several convenient methods of preparation, and optical response throughout the visible, the II-VI materials have received the greatest attention while the economic importance of silicon is self evident. Our studies focus on the II-VI materials.

A tremendous variety of methods have been developed for the production of II-VI semiconductor particles. The discussion below is limited to a series of advances which contribute to the methodology presented in the remainder of thesis.

1.2.1 Preparation in Glasses

Semiconductor nanocrystallites are not an entirely modern creation but have been produced and valued for their optical properties for several hundred years. As noted by Koch,[22] early glass workers found that adding Zn and Cd sulfides and selenides to standard glass melts produced glasses with rich yellow orange and red hues. These original recipes do, in fact, contain dilute concentrations of nanometer size semiconductor nanocrystallites varying in size and composition. Many of the unusual optical properties seen in such semiconductor doped glasses are however compositional fluctuations rather than new mesoscopic phenomena.

Researchers have developed more controlled procedures for the production of QDs in glasses. Contributions from Ekimov *et al*[23] are particularly noteworthy. Procedures generally involve dissolving the semiconductor material (e.g., CdSe) in the glass melt at ~1500°C. The melt is quenched by rapid cooling to below 400°C producing a clear glass. Reheating to between 500 and 700°C allows the growth and annealing of semiconductor crystallites in the viscous glass matrix. Particle size is controlled by

careful selection of the initial concentrations, the annealing temperature and time. Particles produced are highly crystalline fragments of the bulk lattice, have relatively narrow size distributions (standard deviation in diameter σ ~10%) and are roughly spherical in morphology. The glass matrix is an excellent stabilizing medium especially for large crystallites (>200Å) that remain inaccessible by other methods. While the glass provides a robust matrix it however prevents any further manipulation of the crystallites after growth. The glass semiconductor interface remains poorly characterized and the particles have low quantum yields and a manifold of poorly understood trap states.

1.2.2 Low Temperature Preparations

A number of low temperature aqueous preparations have been developed. The earliest methods involved uncontrolled precipitation of material from aqueous solutions.[25] Introduction of polymeric stabilizers like hexametaphosphate (Henglein) allows greater control over the growth process and results in the formation of stable colloidal dispersions.[26] Reaction of measured quantity of H_2S gas with an aqueous solution of cadmium salts and stabilizer produces a stable dispersion of small CdS particles. Manipulation of the solution composition allows control of the surface chemistry as well. Making the solution alkaline forms a passivating layer of $Cd(OH)_2$ on the surface of CdS that permits strong, near band edge luminescence. Size distributions permit the first exitonic feature to be seen although generally higher excited states are not resolved.

Particle size can be controlled by growth in restricted environments such as inverse micelles,[27] zeolites, [28] and Nafion(R) resin.[29] The inverse micelle preparation has the advantage that the surface of the crystallites can be passivated or capped in a secondary reaction. The addition of selected surfactants to alkanes containing traces of moisture results in the spontaneous formation of inverse micelles. These inverse micelles are small surfactant aggregates with an aqueous core dispersed in the alkane media. The average size of the micelles is controlled by the ratio of surfactant to water. Micelles serve as small reactor vessels that are loaded with metal salts (Zn^{++} and Cd^{++}). The addition of organically soluble chalcogenide reagents results in the formation of II-

VI semiconductor nanoparticles. Rapid loading of the organic phase is achieved by injection of the chalcogenide reagents directly into the stirred vessel. Temporally discrete nucleation of nanoparticles occurs in the micelles with further growth limited by diffusion of reagents though the micelle interface. The size of the micelle does not physically restrict the size of the particles but rather affects the spatial distribution of reagents (local concentration). The surfactant molecules temporarily coordinate the surface of the particles formed and sterically stabilizing the dispersions. Aryl thiols or selenols added to the dispersion covalently bind the low coordination metal sites producing an organic capping shell around each particle. Subsequent addition of a flocculant, such as pyridine destabilizes the dispersion, allowing the particles to be separated from the solution. The resulting material is a free flowing powder that can be redispersed in a variety of solvents to remove extraneous by-products and to isolate the nanoparticles retaining only their intimate capping shell. The resulting particles are dispersible in a variety of solvents and can be manipulated in convenient forms for further spectroscopic and structural evaluations. Particle sizes are influenced by reaction conditions but are not precisely tunable. Size distributions between 15-20% are possible. Particles, as prepared, have poor crystallinity and have weak structureless luminescence spectra.

Zeolites and Nafion$^{(R)}$ have been loaded with reagents to produce a variety of different semiconductor inclusions.[28] In contrast to the inverse micelle the pore size of the materials does act to physically limit the size of nanoparticles. Material formed in zeolites and nanoporous resins is permanently imbedded in the host. Although these small nanoparticles are believed to be nearly monodisperse in the case of zeolites, optical features remain poorly resolved. Strong interactions with the zeolite matrix significantly perturb the electronic structure of these small species. Although each system is an interesting composite material in its own right, these host guest systems reveal little of the properties inherent to the semiconductor nanoparticles.

The major drawback of all room temperature preparations is poor crystallinity. Particles are generally agglomerates with internal grain boundaries and defects. We reserve the term crystallite specifically for single domain particles. Defects and

impurities dominate the intrinsic properties of many bulk semiconductors and must be carefully controlled to understand the properties of nanoparticles as well.

1.2.3 Lyothermal Colloid Growth

Post synthesis heat treatments allow the particles to anneal out some of the initial defects and grain boundaries, thus producing material with crystal coherence lengths approaching the dimensions of the particle. Heating in coordinating solvents like 4-ethylpyridine has been found to improved the crystal quality of CdS and CdSe particles grown in inverse micelle preparations. The annealing temperatures (~100 - 200°C) are a fraction of the bulk melting temperature but may be aided by the suppression of melting points in low dimensional solids.[30]

Rather than simply annealing out defects after the growth, a methodology of slow growth at higher temperature has the potential to produce improved crystal quality. Separating the synthesis in a low temperature nucleation step and high temperature growth stages allows the production of high quality CdSe quantum dots (Bawendi).[31] Small QDs (~12A) prepared by the inverse micelle method can be redispersed for further growth and annealing at high temperature. Heating small seed QDs in a mixture of tributylphoshine (TBP) and tributylphophine oxide (TBPO) at 200°C allows Ostwald ripening of the dispersion. A natural bottleneck in the growth produces highly monodisperse samples of 32Å$\pm$8% QDs with the bulk wurtzite structure. Coordination of TBPO electronically passivates the surface of QDs and permits strong near band edge luminescence. Extensive optical investigations of these QDs demonstrated the importance of high quality samples in resolving fundamental optical phenomena. The critical elements of this preparation are separation of nucleation and growth, high temperature, and electronic passivation of the surface. This material clearly represented the state of the art in nanocrystallite synthesis at the outset of our investigations. Thus the challenge was to develop techniques that allowed the facile production of a series of nanocrystallite sizes while attaining or surpassing the quality of these 32Å crystallites in each sample.

Recent progress in the high temperature synthesis of CdS has also been reported by Vossmeyer *et al.* [31] This method produces high quality crystallites with sharp absorption and strong emission.

In this thesis we establish general synthetic procedures for the controlled production of nanocrystallites. We systematically investigate the crystalline core (size, shape, and symmetry), surface and organic capping shell (chemical nature, and dimensions), and establish simple methods to engineer characteristics that influence the properties of these materials. Once these methods for control of the individual crystallites are established we move beyond the properties of the isolated individual crystallites. We organize these artificial atoms into closepacked solids both ordered and disordered. Methods for the characterization and manipulation of these novel solids are then established.

1.3 Bibliography and References

N. Ichinose, Y. Ozaki and S. Kashu, *Superfine Particle Techology* (Springer-Verlag, New York 1988)

National Materials Advisory Board, *Research Opportunities of Materials with Ultra Fine Microstructures* (National Academy Press 1989)

L. Banyai and S. W. Koch, *Semiconductor Quantum Dots* (World Scientific, Singapore 1993).

(1) R. Kubo, J. Phys. Soc. Japan 17, 975 (1962).

(2) L. E. Brus, Appl. Phys. A 53, 465 (1991).

(3) B. C. Crandall and James Lewis, Nanotechnology (The MIT Press, Cambridge 1992).

(4) Reviews include (a) A. Henglein, Top. Curr. Chem. 143, 113 (1988) (b) Y. Wang and N. Herron, J. Phys. Chem. *95*, 525 (1991) (c) M. G. Bawendi, M. L. Steigerwald, and L. E. Brus, Annu. Rev. Phys. Chem. 41, 477 (1991).

(5) L. N. Lewis Chem. Rev. 93, 2693 (1993).

(6) R. Freer, Nanoceramics. The Institute of Materials, London, UK (1993).

(7) M. E. Davis, C. Saldarriaga, C. Montes, J. Garces, and C. Crowder, Nature 331, 698 (1988).

(8) (a) David D. Awschalom and David P. Divincenzo, Physic Today 48, no 4, 43 (1995) (b) David, D. Awschalom, David P. Divincenzo, and Joseph F. Smyth Science 258, 414 (1992).

(9) L. Esaki "The Evolution of Semiconductor Quantum Structures in Reduced Dimensionality - Do-It-Yourself Quantum Mechanics", [(J. M. Chaimberlain Electronic Properties of Multilayers and Low Dimensional Semiconductor Structures.(Plenum Press, New York 1990)] Chapter 1.

(10) C. B. Murray, D. J. Norris, and M. G. Bawendi, J. Am. Chem. Soc. 115, 8706, (1993).

(11) V. Colvin, M. Schlamp, and A. P. Alivisatos, Nature 370, 354 (1994).

(12) B. O. Daboussi, M. G. Bawendi, O. Onitsuka, M. F. Rubner, App. Phys. Lett. 66 (11), 1316 (1995).

(13) M. A. Kastner, Physics Today 46(1), 24 (1993).

(14) (a) V. L. Colvin and A. P. Alivisatos J. Chem. Phys. 97, 730 (1992); (b) V. L. Colvin, K. L. Cunningham, and A. P. Alivisatos, J. Chem. Phys. 101, 7122 (1994)

(15) A. Sacra, D. J. Norris, C. B. Murray, and M. G. Bawendi, J. Chem. Phys. (in press).

(16) L. E. Brus, Appl. Phys. A 53, 465 (1991) (and references there in).

(17) T. Takagahara, Optoelectronic Devices Technol. 8(4), 545 (1993). (b) T. Takagahara, Surf. Sci., 267(1-3), 310 (1992).

(18) C. B. Murray, C. R. Kagan, and M. G. Bawendi (submitted).

(19) L. E. Brus, P. F. Szajowski, W. L. Wilson, T. D. Harris, S. Schuppler, and P. H. Citrin, J. Am. Chem. Soc. 117(10) 2915 (1995) .

(20) J. R. Heath Science 258, 13 (1992).

(21) O. Micic, C. J. Curtis, K. M. Jones, J. Sprauge, and A. J. Nozik, J. Phys. Chem. 98, 4966 (1994).

(22) L. Banyai and S. W. Koch *Semiconductor Quantum Dots* (World Scientific Singapore, 1993), chapter 1.

(23) A. I. Ekimov and A. A. Onuschenko JETP Lett. 34, 345 (1981).

(25) R. Rossetti and L. E. Brus J. Phys. Chem. 86, 4470 (1982).

(26) (a) A. Henglein, Chem. Rev. 89, 1861 (1989), (b) A. Heinglein, Top. Curr. Chem. 143, 113 (1988).

(27) M. L. Steigerwald, A. P. Alivisatos, A. P. Gibson, T. D. Harris, R. Kortan, A. Muller, A. M. Thayer, T. M. Duncan, D.C. Douglas, and L. E. Brus, J. Am. Chem. Soc. 111, 4141 (1989).

(28) G. D. Stucky and J. E. Mac Dougall, Science 247, 670 (1990).

(29) Y. Wang and W. Mahler, Opt. Commun. 61, 233 (1987).

(30) A. G. Goldstein, C. M. Echer, and A. P. Alivisatos, Science 256, 1425 (1992).

(31) T. Vossmeyer, L. Kasikas, M. Giersig, I. G. Popovic, K. Diesner, A. Chemsedine, A. Eychmuller, and H. Weller, J. Phys. Chem. 98, 7665 (1994).

Chapter 2

Synthesis and Size Selective Processing of Nanocrystallites

(Much of this chapter has appeared in print: C. B. Murray *et al*, J. Am. Chem. Soc. 115, 8706 (1993))

2.0 Introduction

The spatial confinement of excitations (electronic and vibrational) and the increasing importance of the surface dominate characteristics of nanocrystallites. Study of an appropriately high quality model system is essential in distinguishing novel properties truly inherent to the nanometer size regime from those associated with variations in sample quality, structural heterogeneities or polydispersity. Each sample must display a high degree of monodispersity in size, shape, etc., in both crystallite core structure and surface derivatization.[1]

Injection of organometallic reagents into a hot coordinating solvent produces temporally discrete homogeneous nucleation. Slow growth and annealing allow the size selected isolation of uniform nanocrystalline dispersions from the growth solution. Size selective precipitation fractionates samples on the basis of crystallite size. Material produced is monodisperse to the limit of atomic roughness.

2.1 Synthesis Experimental

2.1.1 General: All manipulations involving alkylcadmium, silylchalcogenides, phosphines, and phoshine chalcogenides are carried out using standard airless procedures. Tri-n-octylphosphine [TOP] and Bis(trimethylsilyl)sulfide [$(TMS)_2S$] are used as received from Fluka. Electronic grade (99.99+%) selenium and tellurium shot are purchased from Alfa. Anhydrous methanol, n-butanol, pyridine and hexane are purchased from a variety of sources. Tri-n-octylphosphine oxide [TOPO] is purchased

from Alfa and purified by distillation, retaining the fraction transferred between 260-300 °C at ~1 torr. Dimethylcadmium [Me_2Cd] was purchased from Strem Chemical Inc. and purified by filtration (0.250 μm). Bis(trimethylsilyl)selenium [$(TMS)_2Se$] and Bis(t-butyl dimethylsilyl)tellurium [$(BDMS)_2Te$] are prepared via literature methods[2,3] and stored at -35 °C in a drybox. Appropriate masses of selenium and tellurium shot are dissolved directly in sufficient TOP to produce 1.0 M stock solutions of trioctylphosphine selenide [TOPSe] and trioctylphosphine telluride [TOPTe].[4]

2.1.2 Method 1: Typical preparation of TOP/TOPO capped CdSe nanocrystallites: 50 g of TOPO is dried and degassed in the reaction vessel by heating to ~200 °C under ~1 torr pressure for ~20 minutes, flushing periodically with argon. The temperature of the reaction flask is then stabilized at ~300 °C under ~1 atm argon.

Solution A is prepared by adding 1.00 ml (13.35 mmoles) of Me_2Cd to 25.0 ml of TOP in the drybox. Solution B is prepared by adding 10.0 ml of the 1.0 M TOPSe stock solution (12.50 mmoles) to 15.0 ml of TOP. Solutions A and B are then combined and loaded into a 50 ml syringe in the drybox.

The syringe containing the reagent mixture is quickly removed from the dry box and its contents delivered to the vigorously stirring reaction flask in a single injection through a rubber septum. The rapid introduction of the reagent mixture produces a deep yellow/orange solution with an absorption feature at 440-460 nm. This is also accompanied by a sudden decrease in temperature to ~250 °C. Heating is restored to the reaction flask and the temperature is gradually raised to between ~280 - ~300 °C.

Aliquots of the reaction solution are removed at regular intervals (5-10 minutes) and absorption spectra taken to monitor the growth of the crystallites. The best quality samples are prepared over a period of several hours by modulating the growth temperature in response to the size distribution, estimated from the absorption spectra, in order to maintain steady growth. The temperature is lowered in response to a spreading of the size distribution and increased when growth appears to stop. When the desired

absorption characteristics are observed a portion of the growth solution is transferred by cannula and stored in a vial. In this way, a series of sizes ranging from ~15 Å to 115 Å in diameter can be isolated from a single preparation.

CdTe nanocrystallites are prepared by Method 1 with the use of TOPTe as the chalcogen source, an injection temperature of ~240 °C and growth temperatures between ~190 and ~220 °C.

2.1.3 Method 2: A second route to the production of CdS, CdSe and CdTe nanocrystallites replaces the phosphine chalcogenide precursors with $(TMS)_2S$, $(TMS)_2Se$ and $(BDMS)_2Te$, respectively, in Method 1. Growth temperatures between ~300 and ~330 °C were found to provide the best CdS samples. The smallest CdS, CdSe, and CdTe species are produced under milder conditions with injection and growth carried out at ~100°C.

NOTE: Procedures outlined are designed to permit the production of an entire size series, containing 10-20 samples in a single reaction. When specific sizes or smaller amounts of material are needed, scaling down the procedures by a factor 5 is highly efficient.

2.1.4 Isolation of Nanocrystallites: A 10 ml aliquot of the reaction solution is removed by cannula and cooled to ~60 °C, slightly above the melting point of TOPO. Addition of 20 mls of anhydrous methanol to the aliquot results in the reversible flocculation of the nanocrystallites. The flocculate is separated from the supernatant by centrifugation. The dispersion of the resulting precipitate in 25 ml anhydrous n -butanol followed by further centrifugation results in an optically clear solution of nanocrystallites and a gray precipitate containing by-products of the reaction. Energy dispersive X-ray and indexing of powder X-ray diffraction peaks indicate the presence of elemental Cd and Se in the precipitate. The precipitate is discarded. The addition of 25 mls of anhydrous methanol to the supernatant produces flocculation of the crystallites and removes excess TOP and TOPO. A final rinse of the flocculate with 50 mls methanol and subsequent vacuum drying produces ~300 mgs of free flowing TOP / TOPO capped CdSe

nanocrystallites. The resulting powder is readily redispersed in a variety of alkanes, aromatics, long chain alcohols, chlorinated solvents and organic bases (amines, pyridines, furans, phosphines).

2.1.5 Size Selective Precipitation: Dispersion of the purified nanocrystallites in anhydrous n-butanol results in an optically clear colored dispersion. Anhydrous methanol is then added dropwise to the stirred dispersion until opalescence persists upon stirring. Separation of supernatant and flocculate by centrifugation produces a precipitate enriched with the largest crystallites in the sample. Redispersion of the precipitate in n-butanol and size selected precipitation with methanol is repeated until no further sharpening of the optical absorption spectrum is noted. Size selected pecipitation can be carried out in a variety of solvent/non-solvent pairs including pyridine/hexane and chloroform/methanol.

Temperature dependent size selective precipitation is carried out by first titrating the dispersion until opalescence presists and then adding one drop of hexane to return to a clear dispersion. The dispersion is then placed in a centrifuge and the temperature is gradually lowered during the centrifugation. The precipitate and the supernatant are separated and the precipitate is redispersed in butanol. The process is repeated until the absorption spectrum indicates that the desired size distribution has been attained. Sorting of the crystallites is non destructive and the supernatant from each fraction can be processed to yield additional samples.

2.2 Results and Discussion

The preparation and phenomenology of monodisperse lyophobic colloids has been investigated since Faraday's production of gold sols in 1857.[5] Classic work by La Mer and Dinegar has shown that the production of a series of monodisperse lyophobic colloids depends on a temporally discrete nucleation event followed by controlled growth on the existing nuclei.[6] Although broadly embraced, La Mer's concepts have undergone some reevaluation. Growth in several important systems, including Faraday's gold sols,

initially associated with the La Mer mechanism, have since been shown to proceed by a competing mechanism.[6b] This mechanism involves the successive aggregation of smaller particles rather than a slow growth from molecular species in solution. The high temperature methods we describe for the production of II-VI semiconductor nancrystallites appear to be consistent with the La Mer model. Temporally discrete nucleation in our synthesis is attained by a rapid increase in the reagent concentrations upon injection, resulting in an abrupt supersaturation which is relieved by the formation of nuclei and subsequent growth on these nuclei. We have transposed these classic colloid concepts for growth at high temperature, in nonaqueous media and with organometallic precursors.

2.2.1 Synthesis: The work of Steigerwald and co-workers on the use of organometallic precursors in the solution phase synthesis of bulk and nanocrystalline materials provides guidance in our selection of reagents.[2,8] Me_2Cd is chosen as the Cd source and $(TMS)_2E$ (E=S, Se, Te) or TOPSe and TOPTe are selected as the chalcogen source. TOPSe and TOPTe are preferred due to their ease of preparation and their stability. Me_2Cd and $(TMS)_2E$ reagents have been shown to undergo dealkylsilylation in a variety of solvents as a route to bulk materials. Trimethylphosphine telluride is known as a good source of Te^0. Mixed phosphine/ phosphine oxide solutions have previously been found to be good solvents for the high-temperature growth and annealing of CdSe crystallites.[10] The coordinating solvent plays a crucial role in controlling the growth process, stabilizing the resulting colloidal dispersion, and electronically passivating the semiconductor surface. The general reaction scheme for II-VI nanocrystallites is shown schematically in figure 2.1.

Oganometallic chemical vapor deposition (OMCVD) involves the high temperature pyrolysis of organometallic reagents at the gas/solid interface. Control of growth rate allows the dimensions of the deposited layer to be controlled with near atomic precision. Slow growth at high temperatures produces crystalline films with well defined structure and morphology. Combining the elements of high temperature organometallic chemistry with established methods for the preparation and stabilization

of monodisperse colloids provides a convenient route to high quality nanocrystallite samples. The apparatus for this reaction is seen in figure 2.2. This common glassware allows what might be termed organometallic liquid phase epitaxy (OMLPE) of nanometer sized semiconductor structures with near-atomic precision.

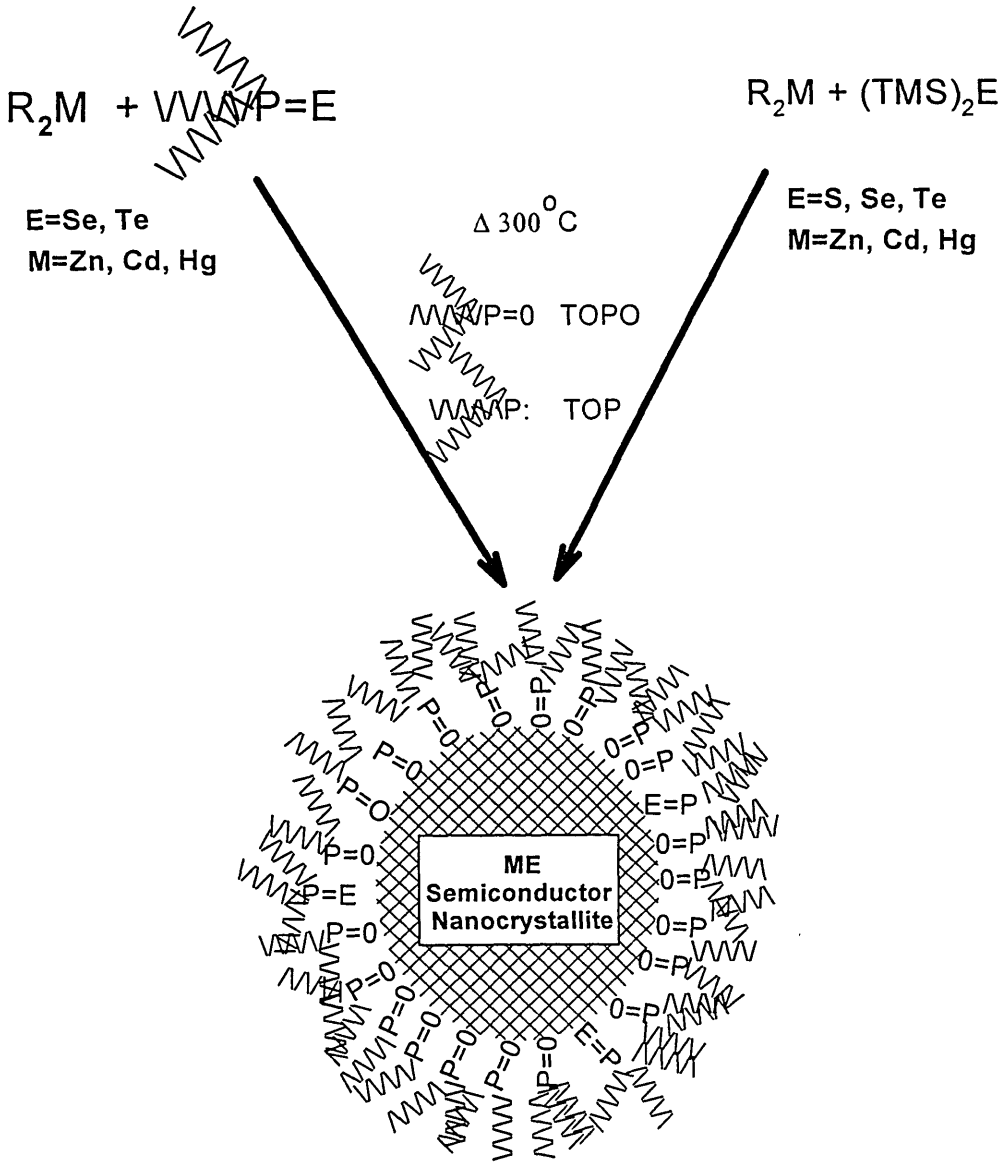

FIG. 2.1 Cartoon of the reaction scheme for the production of monodisperse II-VI nanocrystallites by rapid pyrolysis in coordinating solvents.

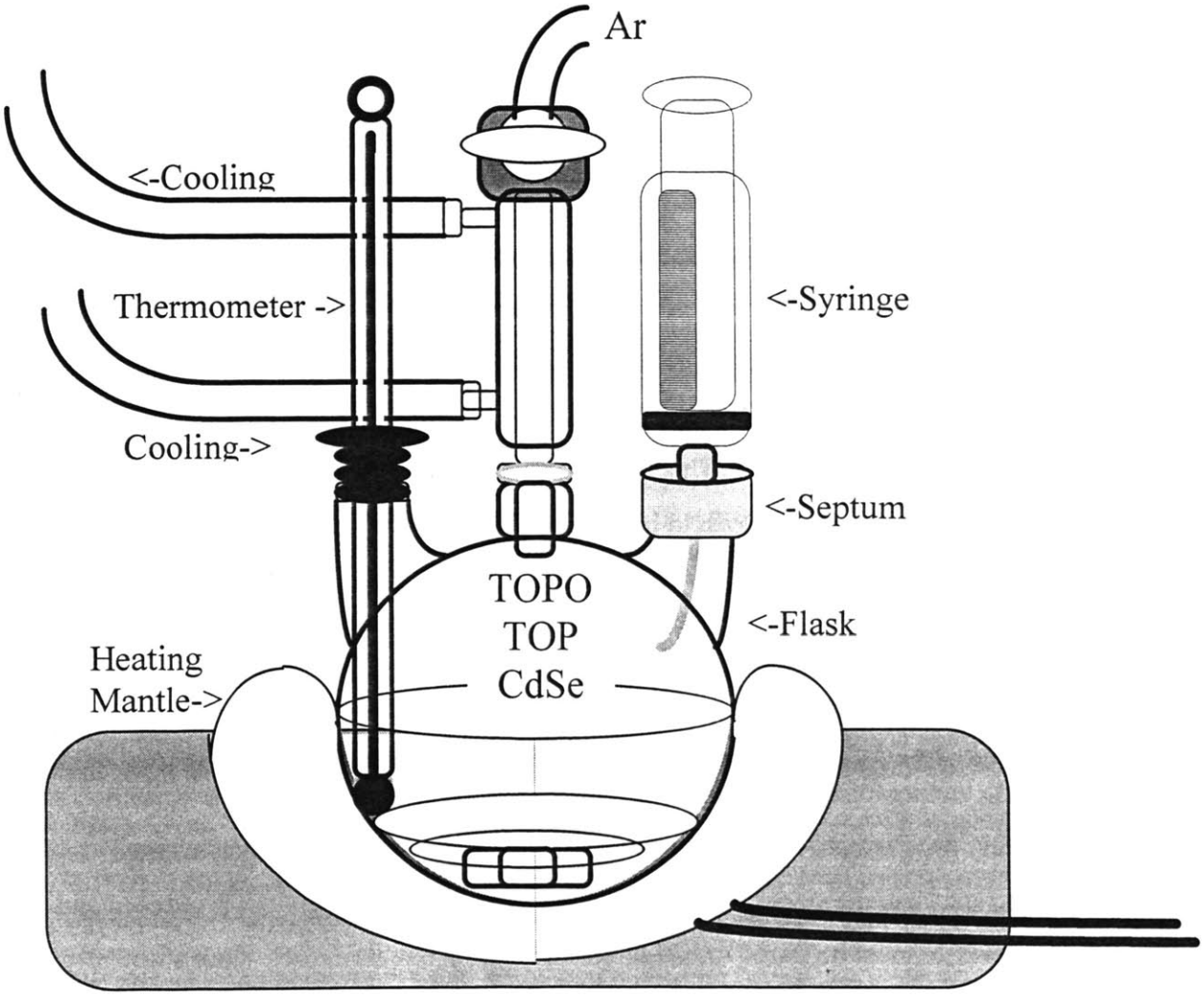

FIG. 2.2 Cartoon of simple synthetic apparatus employed in the growth of monodisperse nanocrystallites.

2.2.2 Nucleation and Growth: Injection of reagents into the hot reaction pot (~320 ^{o}C) results in a short burst of homogeneous nucleation. The depletion of the reagents through nucleation and the sudden temperature drop associated with the introduction of room temperature reagents prevents further nucleation. Reheating the dispersion to ~280 - 300 ^{o}C allows slow growth and annealing of the crystallites. Crystallite growth is consistent with "Ostwald Ripening". The higher surface free energy of small crystallites makes them less stable with respect to dissolution in the solvent than larger crystallites. The net result of the stability gradient within a dispersion is slow diffusion of material from small particles to the surface of the larger particles.[11] Thus as reaction proceeds the average size of the crystallites increases with a compensating decrease in the number of crystallites. Adjustment of the temperature allows the growth rate to be stabilized at ~ 1 atomic plane every 10 minutes. This rate allows a series of samples differing in average size by less than one atomic plane to be isolated. Fig 2.3 shows the progress of our reaction within a general model for monodisperse colloid growth as developed by La Mer. Reiss has shown how growth by this kind of transport can result in the production of monodisperse colloidal dispersions from systems that may initially be polydisperse.[12]

Average crystallite size and the size distribution within a sample are dependent on the growth temperature, consistent with surface energy considerations. The growth temperature necessary to maintain steady growth increases with increasing average crystallite size. As the size distribution sharpens the gradient for growth is reduced and the temperature must be raised to maintain steady growth. Conversely, if the size distribution begins to spread, the temperature necessary to maintain steady growth decreases. Size distributions during growth are crudely estimated from absorption line widths (typically 50 nm fwhm). Modulation of the reaction temperature in response to changes in the absorption spectrum allows maintanance of the shape of the size distribution as the samples grow.

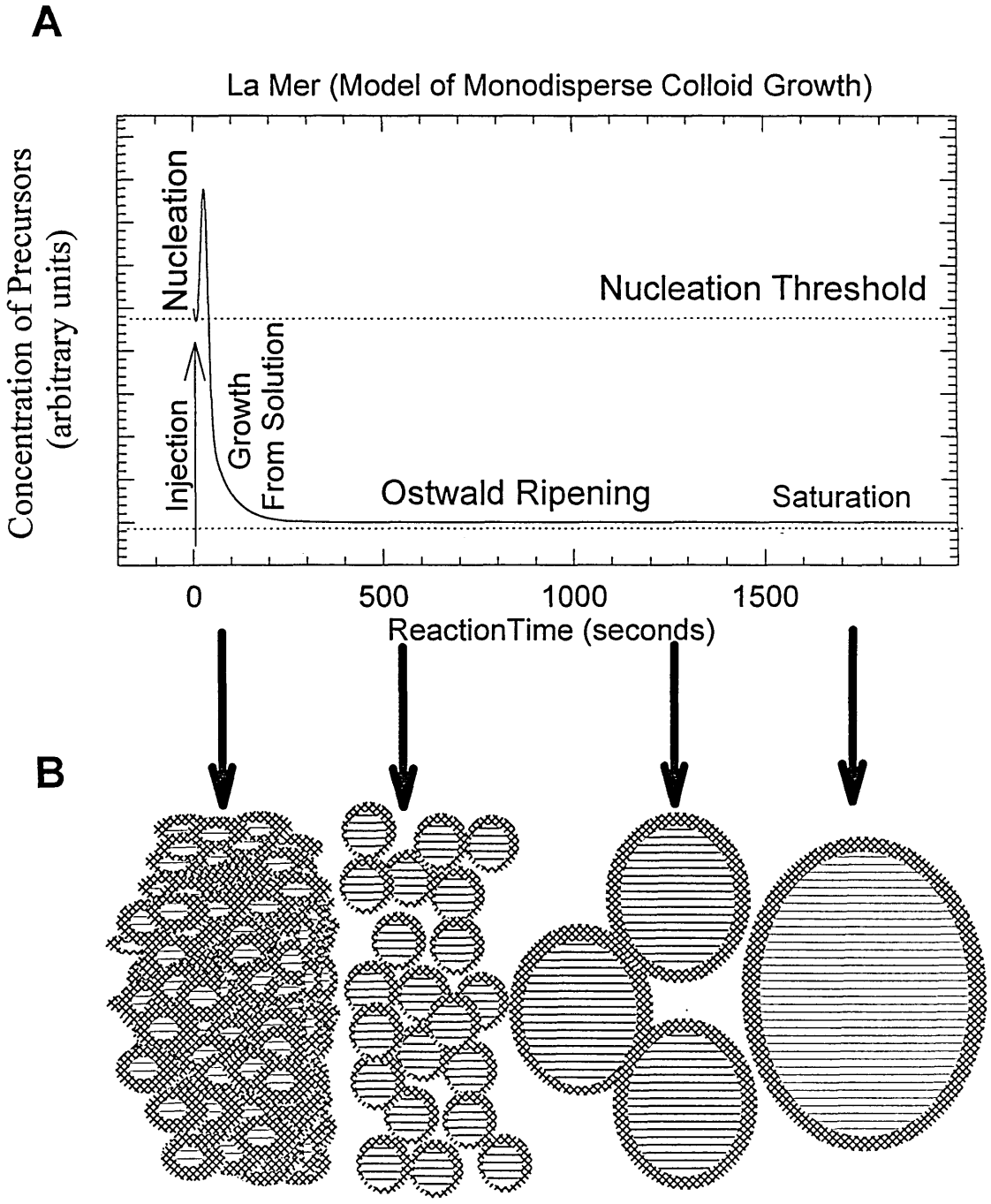

FIG. 2.3A Cartoon of the nucleation and growth of CdSe nanocrystallites in the framework of a "La Mer Growth Model".

FIG. 2.3B Cartoon depicting the isolation of a size series by periodically removing aliquots.

Capping groups present a steric barrier to the addition of material to the surface of a growing crystallite, significantly slowing the growth kinetics. The TOP/TOPO solvent coordinates the surface and permits slow steady growth at temperatures above 300 °C. Replacing the octyl chains with less bulky groups reduces the temperature for controlled growth. Mixed alkylphoshine/phoshine oxide solvents with butyl, ethyl, and methyl groups show uncontrolled growth at 230, 100, and 50 °C respectively. In addition to steric effects, the chemical affinity of the phosphine moiety ($R_3P=O$) for the metal center can be tuned by the choice of the R group, thus further controlling the growth rate. Stronger coordination of the capping group to the metal (i.e. more electron donating) slows the growth. Injections into non-coordinating solvents like hexadecane and mesitylene produce polycrystalline bulk material that precipitates immediately from solution. Steady controlled growth produces particles of uniform size, shape and consistent crystal structure by extracting aliqotes of the growth solution periodically from the reaction mixture. In this way an entire size series containing 10-15 high quality samples can be produced in a single 4 hour preparation.

A notable modification of this general reaction scheme has been developed by Bowen Katari *et al*[13] and has been reproduced in our lab: The temperature of the reaction vessel containing the TOPO is raised to between 350 and 400 °C (boiling) and a small volume of the reagents in TOP are injected. Nucleation and growth occur within the time of the injection. The reaction is allowed cool to room temp without further growth. The nucleation process becomes chaotic under these forcing conditions. Variations of a few degrees in temperature or a few percent in concentration produce dramatically different initial size distibutions. "Successful injections" produce samples with size distributions sharp enough to suppress Ostwald ripening while the reaction vessel is cooling. Average crystallite size can range from 20 to 60Å in diameter but is not easily controlled. A statistically large number of preparations allows a sample series of high quality to be prepared. It should also be noted that the solvent TOPO is not stable above 330 °C and steadily undergoes decomposition to produce an increasingly complex

chemical mixture. The resulting distributions of potential capping groups may contribute to the difficulties in further sharpening the size distribution.

Crystallites isolated from this reation media have formed at temperatures between 350 °C and 400°C, resulting in low stacking fault densities (~1 fault in every 12 planes) and are nearly spherical. Particles have not grown through the slow process of Ostwald ripening that produces a prolate shape in our standard preparation. Thus controlling the percentage of crystallite growth which occurs in the Ostwald ripening regime allows the control of crystallite shape. These results may be important in understanding the influence of stacking faults and crystallite shape in more sophisticated optical investigations.

Preparation of zinc chalcogenides (ZnE) from diethylzinc is straightforward with only minor modifications to the procedures described. The growth of ZnE nanocrystallites must be carried out in a neat TOP or mixtures containing only a few percent oxide. The formation of thermally stable TOPO adducts with Zn provides too great a barrier for growth. Crystallites can be isolated and processed by procedures analogous to those for CdE. Danek *et al* [14] have futher developed the synthesis and handling of nanocrystalline ZnE for production of CdSe overcoated with ZnSe as a passivating layer. HgE nanocrystallites are produced by reaction of dibenzylmercury with chalcogenide reagents at temperatures as low as 100 °C. Particles produced remain largely uncharacterized.

Recently these general procedures have been successfully extended by Micic *et al* to provide high quality III-V nanocrystallites. Pyrolysis of Indium and Gallium halo oxalate precursors with $(TMS)_3P$ in a mixture of TOP / TOPO produces highly crystalline InP[15] with bulk zinc blende structure. Subsequent size selective precipitation allows the narrowing further narrowing of the initial size distribution.

A wealth of potential organometallic precursors and high boiling point coordinating solvents exist. Although phosphine/ phosphine oxide has been found to provide the most controlled growth conditions, a range of coordination solvents can be employed. Injections of reagents into hot alkylphoshites, alkylphosphates, pyridines, alkylamines, and furans all produce nanocrystallites.

2.2.3 Colloid Stabilization and Size Selective Precipitation

The reaction mixture contains a mixture of the nanocrystallites and synthetic by-products. Repeated flocculation and redispersion in a series of solvents allows the isolation of powders containing the desired nanocrystallites and their intimate organic capping layer. Modifications of the general procedure futher allows the isolation of size selected fractions.

Lyophobic colloidal particles attract each other by van der Waals forces. Colloids remain stable with respect to aggregation only if there exists a repulsive force of sufficient strength and range to counteract the van der Waals attraction. Thus colloidal dispersions can be stabilized by supressing the van der Waals interactions or by the introduction of an additional repulsive force. The attraction is an induced-dipole / induced-dipole interaction resulting from correlated fluctuations in the electron density in pairs of atoms from different particles. These van der Waals forces are nearly additive and increase with the increasing size of the particles. The molecular origins of van der Waals interactions in colloid systems are reviewed by Hiemenz.[16]

The presence of an intervening solvent serves to screen these interactions. If the dielectric constant of the solvent is adjusted to be equal to that of the spheres, the Van der Waals attraction is screened. CCl_4 and $CHCl_3$ are high dielectric solvents that screen the interparticle attraction and thus provide good dispersing media.

Chemisorption of ambiphylic species on the surface of the particles gives rise to a steric barrier to aggregation. Steric stabilization results from a combination of both enthalpic and entropic effects.[17] The dispersions of CdSe nanocrystallites are stabilized by a lyophylic coat of alkyl groups anchored to surface Cd sites by phosphine oxide / selenide moieties. The efficiency of the steric stabilization is strongly dependent on the interaction of the the alkyl groups with the solvent. Gradual addition of a nonsolvent or the preferential evaporation of solvent from a solvent / nonsolvent mixture can produce size dependent flocculation of the nanocrystallite dispersion. Figure 2.4 shows a cartoon of the inter-particle potential for fixed paricle size as a nonsolvent is added. The curves are a combination of an attraction of the form βR^{-6} and a steric repulsion of the form αR^{-}

^{12} where R is the center-to-center distance for the particles. In curves a, b, c, and d the efficiency of the steric repulsion (α) is sequentially reduced. The reduction of the steric repulsion is seen to produce a local minimum for the particles in close contact. It is the depth of this well with respect to ambient thermal energy (Brownian motion) that determines whether flocculation will occur.

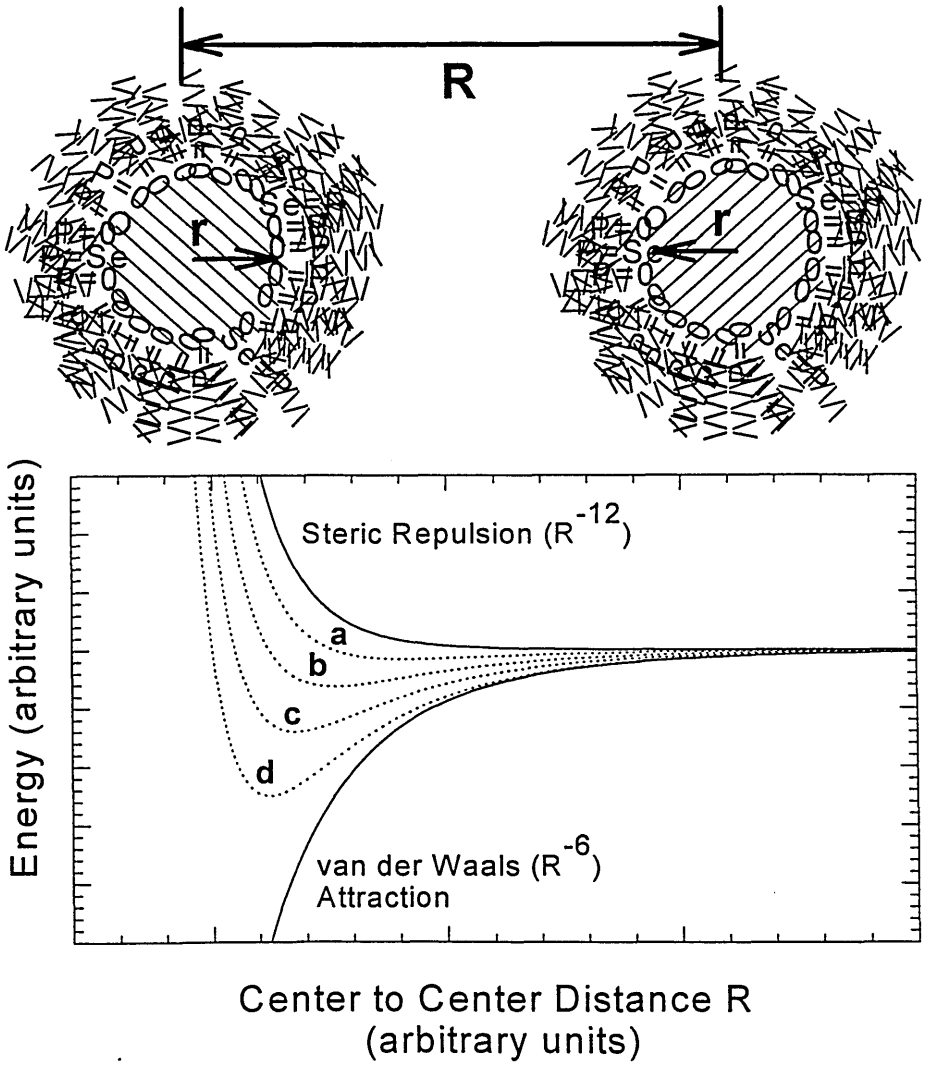

FIG. 2.4 Cartoon of the inter-particle potential, the steric repulsion and the van der Waals attraction. Addition of a nonsolvent to the dispersion reduces the repulsion. The net potential is depicted in curves (a) through (d).

Adjusting the dispersion solvent/nonsolvent composition to near its critical point and then cooling the dispersion results in size dependent flocculation. As the dispersion passes a

critical level of stability aggregates nucleate and grow by addition of primary particles from the bulk of the dispersion. The discrete nucleation and growth results in the formation of nearly monodisperse secondary particles. These spherical aggregates in turn form a network of tertiary stuctures we refer to as flocs. The various stages of this self-similar assembly are seen in figure 2.5. Panel A shows a TEM image of uniform 80Å diameter CdSe nanocrystallites initially dispersed in solution and now aggregated in a secondary particle. Panel B shows the remarkable uniformity of the secondary particles thus formed. These secondary particles then form networks seen in panels C and D to produce structures separated by centrifugation. Similar properties have long been used to fractionate polymers and other macromolecules on the basis of their molecular weight. This general phenomenon can be employed in our nanocrystalline samples to narrow the particle size distribution to the limit of atomic roughness (σ ~4%).

The largest particles in the dispersion experience the greatest attractive forces. When the surface passivation is uniform and the steric repulsion is slowly lowered by the addition of a nonsolvent the larger particles have a deeper potential well and thus are enriched in the flocculate produced. Thus simple titration of a nonsolvent into the dispersion brings about size selective precipitation. The flocculate can be separated by centrifugation. The removal of a specific subset of the particles from the initial size distribution narrows the size distribution in both the supernatant and the flocculate. A bar graph in figure 2.6(A) shows the size distributions (measured by TEM) of CdSe nanocrystallites in the growth solution and after size selective percipitation. The standard deviation of ~4% is 1ess than one atomic plane. Depending on the capping molecules chosen, a number of solvent/nonsolvent pairs can be used in size selective precipitation (e.g. Hexane/Ethanol, Chloroform/Methanol, Pyridine/Hexane). A cartoon in figure 2.6B shows the simple titration apparatus.

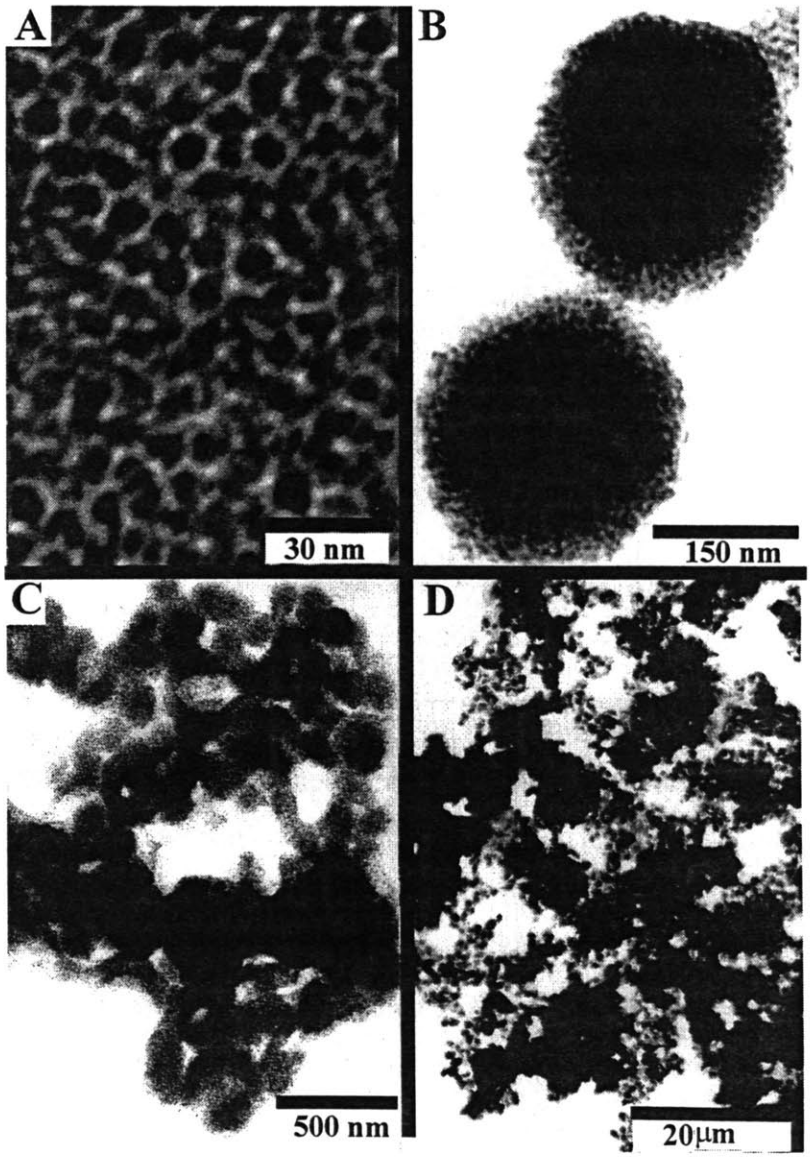

FIG. 2.5 TEM images of the self similar aggregation during size selective precipitation. Panel (A) shows the 80Å crystallites that make up the primary aggregates. Panel (B) highlights the uniformity of the primary aggregates. Panels (C) and (D) show the flocs formed by aggregation into tertiary structures.

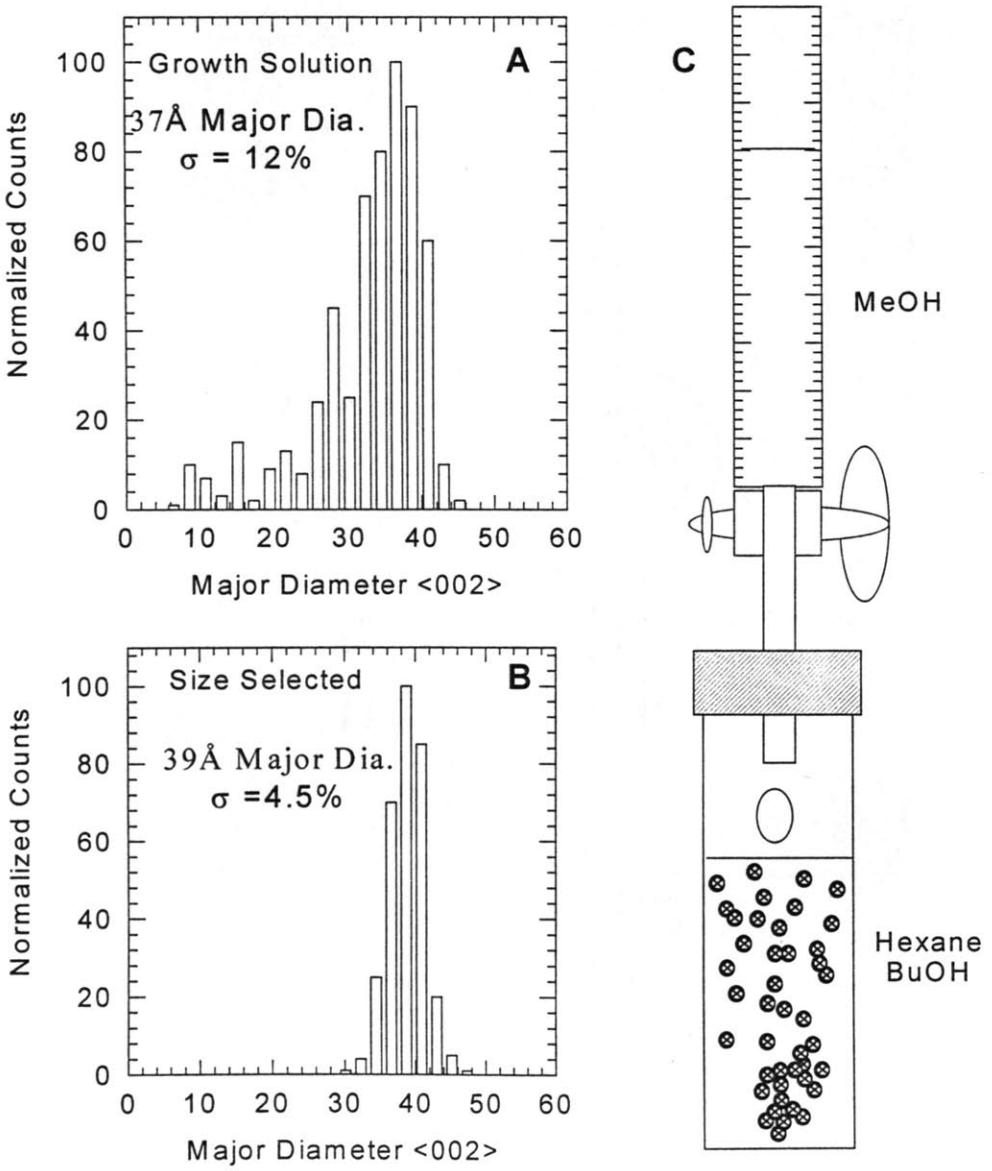

FIG. 2.6 panels (A) and (B) show the results of statistical analysis of TEM images for native and size selected samples, respectively. Panel (C) shows a cartoon of the simple titration process.

Figure 2.7 illustrates the dramatic sharpening of the optical features with size selective precipitation. In panel A the destabilization results from titration of a nonsolvent while panel B employed temperature dependent flocculation.

In panel A, spectrum (a) shows the absorption of the initial growth solution. As seen earlier the positions of the features are strongly size dependent and thus wash out rapidly with increasing polydispersity. The broad absorption feature corresponds to a sample with an average size of 37Å $\pm$ 12% dispersed in 80% hexane / 20% n-butanol. Slow addition of methanol results in the flocculation of the larger particles in the distribution. Spectrum (b) shows the absorption of these particles after redispersion in n-butanol. Titration of sample b with methanol again produces flocculation of the larger particles (spectrum (c)). A final size selective precipitation yields sample d with an average size of 42Å and σ<4%. Spectrum (d) is dramatically sharpened relative to that of the initial growth solution and reveals several transitions previously cloaked by polydispersity. It is important to note that the first absorbance feature in samples with distributions of 10% or greater is actually a convolution of underlying transitions thus introducing a significant error in the esimated HOMO-LUMO gap. For samples with σ less than 8% the assignment of the first transition is unambiguous. For the fractionation process to work well it is crucially important that the shape and surface derivatization of the initial crystallites be uniform and the initial polydispersity in size be relatively small.

The capping molecules are weakly bound to the surface of the particles and maintain a dynamic equilibrium with free species in solution. Repetitive size selective processing gradually strips away these capping groups. This deterioration of the stabilizing shell is entirely reversible with the addition of a small amount of TOP/TOPO to the dispersion. In addition the flocculation process is reversible at any step by addition of fresh solvent. An alternative form of size selective precipitation has been employed by Chemseddine *et al* in the fractionation of CdS dispersions.[18] A mixed solvent / nonsolvent dispersion can be destabilized by preferential evaporation of the solvent from the dispersion (e. g. pentane / ethanol), producing a flocculate enriched in the larger particles.

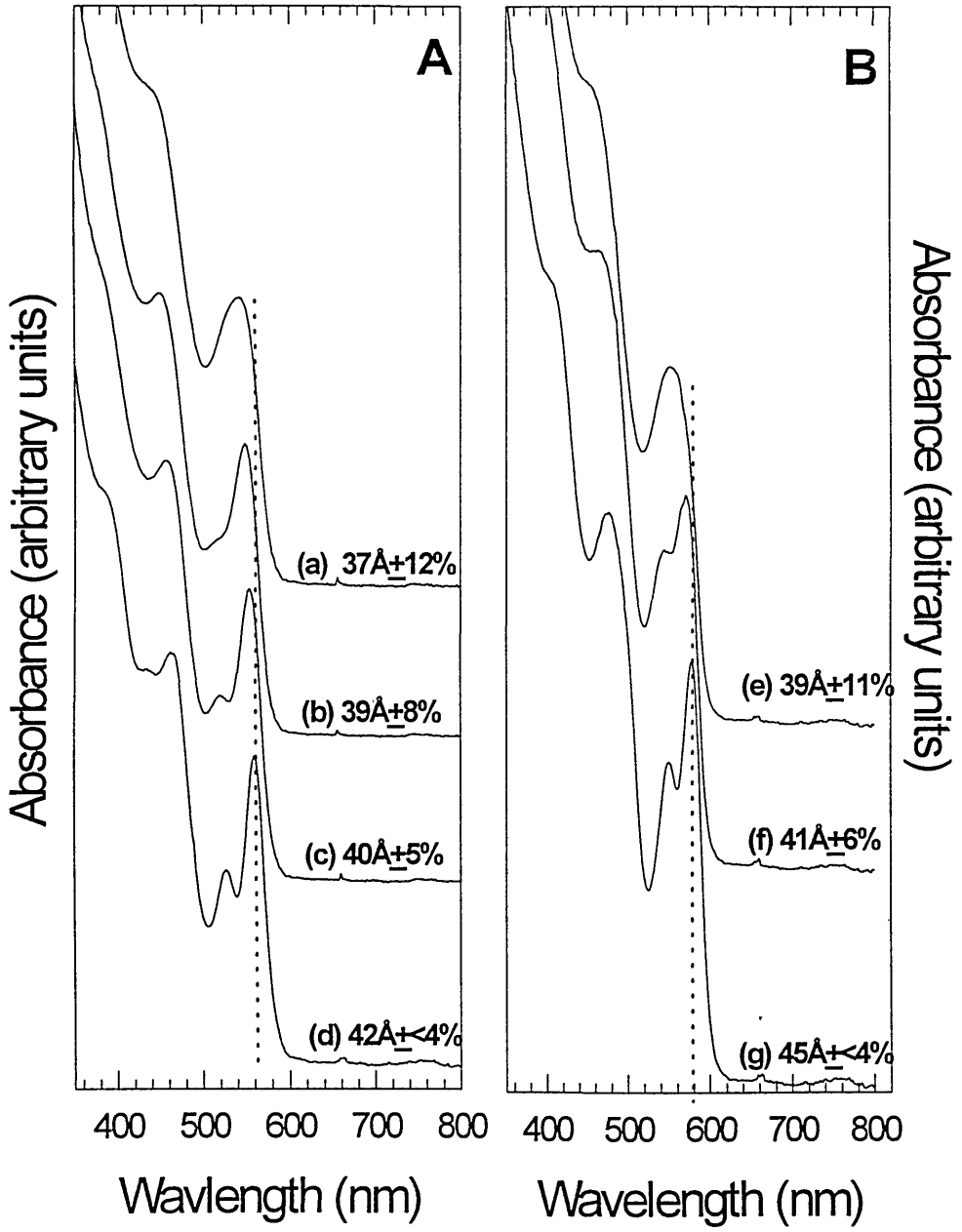

FIG. 2.7 Optical absorption spectra of samples at different stages of the size selection process described in the text. Panel (A) shows the results of size selection using the titration method. Panel B shows the results of sequential processing by temperature dependent size selective precipitation.

Methods of destabilization discussed thus far have focused on altering the solvent composition. However temperature can also be adjusted to produce controlled flocculation. When the dispersion is adjusted to be near its critical flocculation point, gentle cooling of the sample reduces the entropic contributions to the repulsion and the thermal energy available to re-seperate the particles. This destabilization results in flocculation of the largest particles. Gentle cooling of a sample during centrifugation is particularly effective as it avoids local fluctuations in concentration inherent in titrations. Small aggregates are removed as they form. The rapid removal of these aggregates reduces the entrainment of smaller particles in the large networks of flocs. The results of temperature dependent fractionation are shown in figure 2.7B. Spectrum (a) shows the initial growth solution with an average size ~39Å (σ=11%). Solvent composition was adjusted to the critical point at 40° C by titration with methanol and then the dispersion was slowly cooled to 5° C during centrifugation. The precipitate was redispersed in a 80% butanol / 20% hexane solution yielding spectrum (b). Repetition of the temperature dependent flocculation produces the sample seen in spectrum (c) corresponding to an average size of 45Å (σ = 4%). Nanocrystallites are non-destructively sorted on the basis of size, thus a single aliquot of growth solution can be fractionated to yield up to 3 high quality samples (σ =4%).

To first order the additivity of the van der Waals forces results in attractive forces that increase like the volume of the particle (r^3). Steric stabilization increases with the number of attached capping groups and thus scales like the surface area (r^2). For a particular capping group and solvent there is an upper limit to the size of particles that can be stabilized. This is observed experimentally with triethly, tributyl, and trioctyl phosphine moieties displaying limits of ~30Å, 70Å, and 160Å diameter particles respectively in hexane. The efficiency of several capping groups has been measured by SAXS in dilute solutions showing similar results. Small angle X-ray studies in dilute dispersions permit the measurement of thermodynamic properties of macromolecular dispersions to be measured. Studies have been carried out by Mattoussi *et al*[19] to investigate the interparticle potentials of these CdSe dispersions as a function of particle size, solvent composition, and choice of capping functionality.

2.3 Conclusion

Rapid pyrolysis of organometallic reagents in a coordinating solvent produces temporally discrete nucleation. Slow growth by Ostwald ripening allows material to be isolated periodically from the reaction vessel. Thus an entire size series of high quality nanocrystallites can be isolated from a single reaction. Subsequent size selective precipitation allows the samples to be fractionated, producing material monodisperse to the limit of atomic roughness. A systematic investigation of the evolution of material properties is now possible.

2.4 Bibliograghy and References:

F. A Cotton and G. Wilkinson, Avanced Inorganic Chemistry Fifth Edition (John Wiley & Sons, New York 1988).

F. R. Hartley, The Chemistry of Organophosphorous Compounds 2 (Wiley, New York 1992).

P. C. Hiemenz, Principles of Colloid and Surface Chemistry Second Edition (Marcel Dekker, New York 1986).

R. J. Hunter, Foundations of Colloid Science Volume 1 and 2 (Clarendon Press, Oxford 1987).

(1) C. B. Murray, D. J. Norris and M. G. Bawendi, J. Am. Chem. Soc. 115, 8706 (1993).

(2) M. L. Steigerwald, A. P. Alivisatos, J. M. Gibson, T. D. Harris, R. Kortan, A. J. Muller, A. M. Thayer, T. M. Duncan, D. C. Douglas, L. E. Brus, J. Am. Chem. Soc. 110, 3046. (1987).

(3) M. R. Detty, M. D. Seidler, J. Org. Chem. 47, 1354 (1982).

(4) R. A. Zingaro, B. H. Steeves, K. J. Irgorlic, Organometal. Chem. 4, 320 (1965)

(5) J. Th. G. Overbeek, Advances in Colloid and Interface Science 15, 251 (1982)

(6) V. K. LaMer and R. H. Dinegar, J. Am. Chem. Soc. 72, 4847. (1950). (b) E. Matijevic, Langmuir 10, 8 (1994).

(7) T. Fukui, H. Saito, M. Kusu, and S. Ando, J. Crystal Growth 124, 493 (1992)

(8) S. M. Stuczynski, J. G. Brennan, and M. L. Steigerwald, Inorg. Chem. 28, 4431 (1989).

(9) (a) M. L. Steigerwald and C. R. Sprinkle, J. Am. Chem. Soc. 109, 7200 (1987) (b) M. L. Steigerwald, Chem. Mat. 1, 52 (1989).

(10) M. G. Bawendi, A. R. Kortan, M. L. Steigerwald, and L. E. Brus, J. Chem. Phys. 91, 7282 (1989).

(11) A. L. Smith, Particle Growth in Suspensions (Academic Press: London (1973)); pp 3-15.

(12) H. Reiss, J. Chem. Phys. 19, 482 (1951).

(13) J. E. Bowen Katari, V. L. Colvin, and A. P. Alivisatos, J. Phys. Chem. 98, 4109 (1994)

(14) M. Danek, K. F. Jensen, C. B. Murray and M. G. Bawendi (submitted)

(15) O. Micic, C. J. Curtis, K. M. Jones, J. Sprauge and A. J. Nozik, J. Phys. Chem. 98, 4966 (1994).

(16) P. C. Hiemenz Principles of Colloid and Surface Chemistry Second Edition (Marcel Dekker New York 1986) p. 616-632.

(17) T. Sato and R. Ruch, Stabilization of Colloidal Dispersions by Polymer Absorption (Marcel Dekker, New York, 1980); p 46-51.

(18) A. Chemseddine, H. Weller, Ber. Bunsen-Ges. Phys. Chem. 97, 636 (1993).

(19) H. Matoussi (unpublished).

Chapter 3

Optical Characterization

(Much of this chapter has appeared in print: C. B. Murray *et al*, J. Am. Chem. Soc. 115, 8706 (1993))

3.0 Introduction

II-VI semiconductor nanocrystallites have become widely studied as models of 3 dimensional quantum confinement.[1] With direct band gaps in the visible and a relatively simple band structure, these materials allow the evolution of the electronic states to be followed by standard spectroscopic techniques. Optical characterization presented here focuses on simple room temperature measurements as a probe of sample quality. Extensive low temperature investigations have been carried out, mapping in detail the evolution of electronic states in CdSe nanocrystallites in absorption[2-3] and in luminescence.[4]

3.1 Experimental: Room temperature optical absorption spectra were collected on a HP8452 diode array spectrometer using 1 cm quartz cuvettes. Samples were prepared by redispersing washed CdSe nanocrystallites in hexane. Luminescence experiments were carried out on a SPEX Fluorolog DM3000 spectrometer operating in front face collection with 500μm slits. Estimates of quantum yield were obtained by comparing total emission from Rhodamine 590 in methanol and a sample of 30 Å CdSe nanocrystallites dispersed in hexane. A drop of a 1% solution of TOP/TOPO was added to the dispersions to ensure optimal particle stabilization and maximum quantum yield. Concentrations of materials were adjusted to provide optical densities of 0.1 at 400 nm in matched 1 mm quartz cuvettes. Fluorescence spectra were collected between 480 and 800 nm at room temperature with 400 nm excitation. Procedures for the collection of low temperature spectra are detailed elsewhere.[8]

3.2 Results and Discussion

3.2.1 Absorption: Optical absorption spectra of ~20-30Å diameter CdS, CdSe, and CdTe nanocrystallites are shown in figure 3.1. All three clearly show the effect of quantum confinement. CdS, CdSe, and CdTe absorption features are shifted dramatically from their 512, 716, and 827 nm bulk band gaps, respectively. CdSe nanocrystallites show clearly resolved transitions while the CdS and CdTe samples show less structure. We do not believe the difference in the quality of the optical spectra reflects any fundamental material limitations but rather the amount of effort spent in optimizing the growth conditions for each material. Efforts have been focused on CdSe as a model system for the synthesis, processing, and characterization of nanocrystallites.

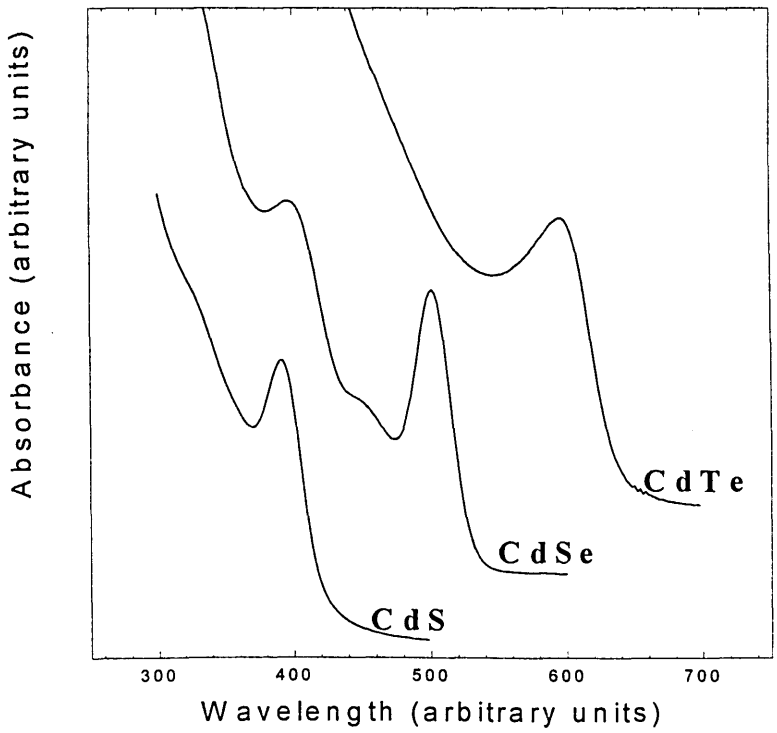

FIG. 3.1 Optical absorbance of 20-30Å diameter CdS, CdSe, and CdTe nanocrystallites.

Synthetic methods produce samples of crystallites ranging in size from ~15 to 150Å with each sample monodisperse to the limit of atomic roughness (~4% rms in diameter). Particles are slightly prolate fragments of the bulk lattice with low defect densities and efficient surface passivation. Results of these optimized procedures are displayed in the room temperature absorption spectra of a series of CdSe QDs (figure 3.2). Panel A shows the evolution of the optical absorption features from the molecular limit to the bulk. Each sample roughly represents an increase in particle diameter of a single lattice plane allowing the optical evolution of CdSe with size to be clearly seen, even at room temperature. Panel B shows an expanded view of every fifth sample to reveal the sharp transitions observable at room temperature.

Extensive structural studies in chapter 4 reveal that our CdSe QDs are slightly prolate. Most theories have considered models of spherical QDs. We compensate for the perturbation of the non-spherical shape by employing an equivalent radius defined as the radius of a sphere of equal volume to that of the ellipsoidal particle.[5] Equation 3.1 defines the equivalent radius R_{eq} (equivalent diameter $D_{eq} = 2R_{eq}$)

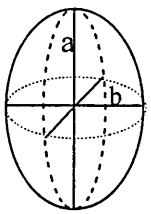

$$(3.1)\quad R_{eq} = \sqrt[3]{ab^2}$$

where a and b are the major and minor radii of the ellipsoid, respectively. Equation 3.2 treats quantum confinement in the effective mass approximation,[1a]

$$(3.2)\quad E^* \cong E_g + \frac{\hbar^2\pi^2}{2R^2}\left[\frac{1}{m_e} + \frac{1}{m_h}\right] - \frac{1.8e^2}{\varepsilon R}$$

where E^* is the confinement energy, E_g is the bulk band gap, R is the radius of the quantum dot and m_e and m_h are the effective masses of the electron and hole, respectively.

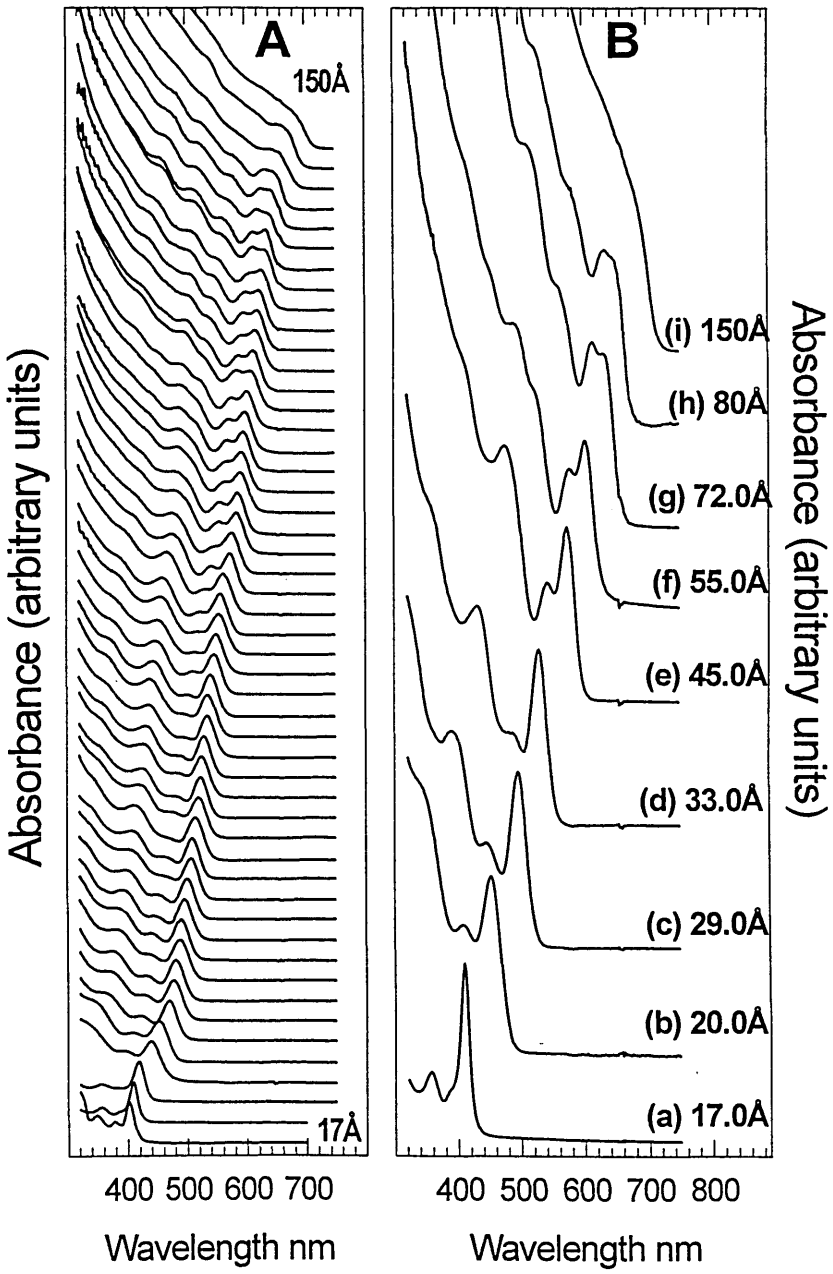

FIG. 3.2(A) Optical absorbance spectra of CdSe nanocrystallites ranging from ~17Å to 150Å in diameter in increments of one atomic plane.

FIG. 3.2(B) Optical spectra representing the range of sizes that can be isolated form a single preparation.

Figure 3.3 shows the prediction of the effective mass model as a solid line and the experimental data as solid triangles. Although experiment and theory agree reasonably well at large sizes, divergence of the simple theory from experimental values for small sizes is expected from the non-parabolicity of the bands at higher wave vectors and the presence of a finite potential barrier at the surface of the particles. More advanced treatments by Lippens and Lannoo[6] provide much better agreement with experimental results.

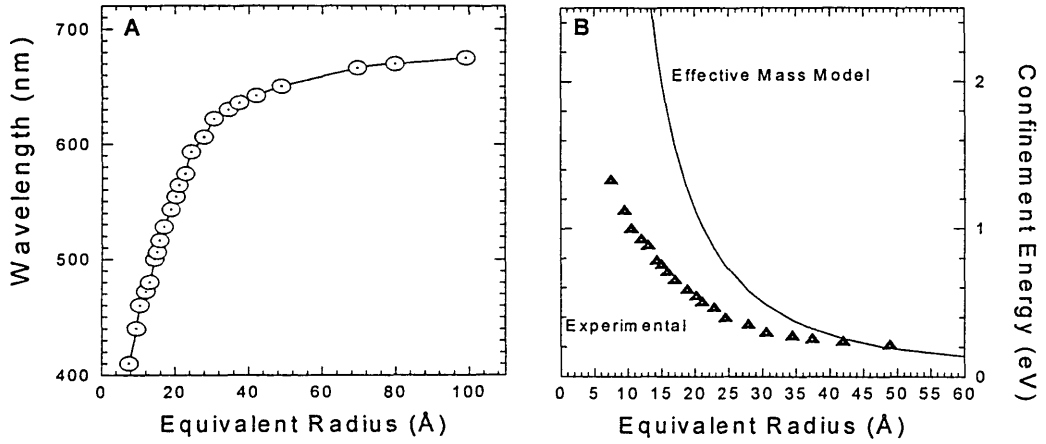

FIG. 3.3(A) Absorption position (wavelength) of the first excited state as a function of crystallite (R_{eq}).

FIG. 3.3(B) Confinement energy (E*) as a function of crystallite size (R_{eq}). Triangles are experimental sizes (TEM and SAXS) while the solid line represents the predictions of the effective mass model.

3.2.2 Luminescence: QDs are of interest for their strong tunable features in emission as well as in absorption. These excised fragments of the bulk lattice are robust inorganic chromophores with emission tunable from the near-uv to the near-infrared. Figure 3.4A shows room temperature absorbance and luminescence spectra for a series of CdSe samples. The smallest species display broad emission shifted significantly from the band edge absorption. These broad features are referred to as "deep trap" emission. The physical origin of these deep trap states is still unresolved. As crystallite size increases a sharper band edge emission feature grows in. Linewidths of this feature are equal to

those in absorption and resemble emission from bulk semiconductors. In our studies the quality of the internal crystal structure is seen to influence the relative proportions of deep trap and band edge emission. Each of the band edge luminescence features is red shifted from the absorption maximum (Stokes shift). Crystallites grown a low temperature have high defect densities and display a greater proportion of deep trap emission. The size dependence of the Stokes shift is characteristic of the quantum mechanical nature of the emitting state and has been extensively investigated.[7]

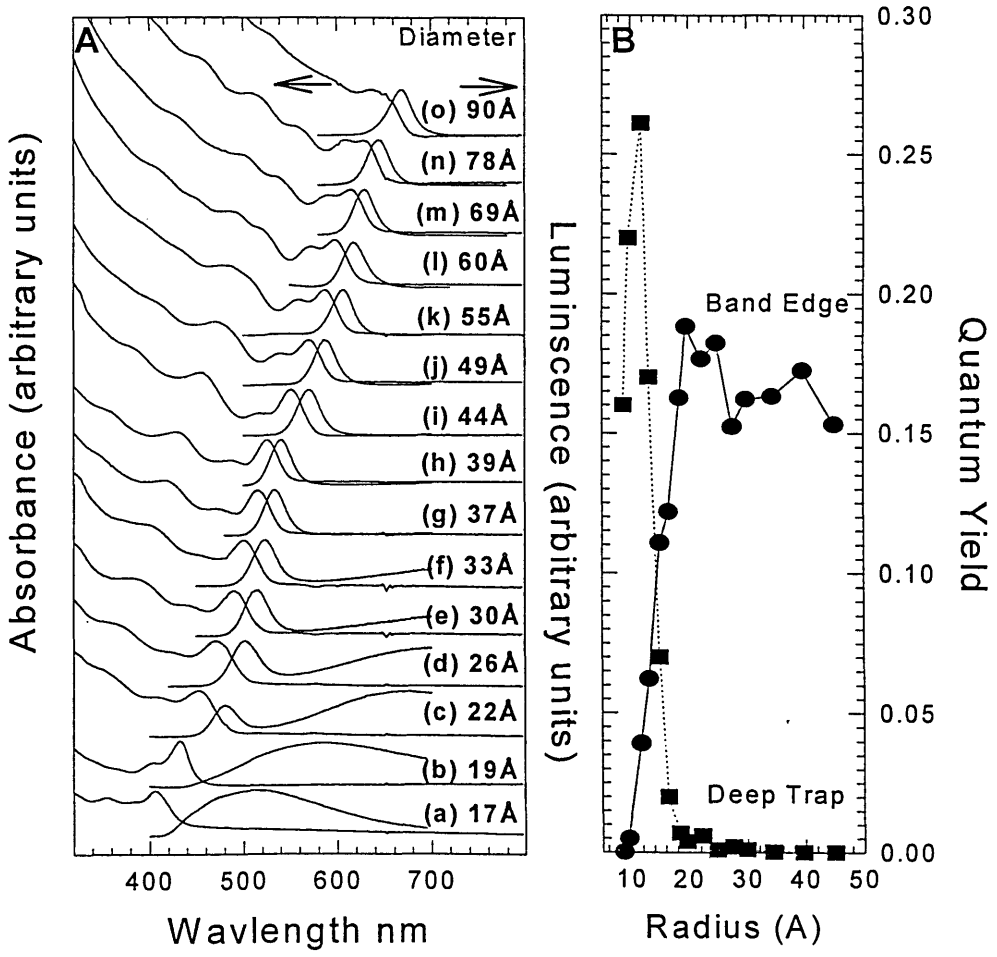

FIG. 3.4A Room temperature absorption and luminescence spectra for a series of CdSe nanocrystallite size ranging from ~17Å to 90Å in diameter.

FIG. 3.4B Room temperature quantum yields (QY) for CdSe nanocrystallites as a function of size. Band edge luminescence (circles) and deep trap (squares).

In any applications involving the nanocrystallites as tunable emitters, the spectral linewidth and quantum yield (QY) are important figures of merit. Near band edge features display ~40 nm linewidth FWHM at room temperature. The QY is the fraction of the photons absorbed that are reemitted, ($QY = I_{lum}/I_{abs.}$). Fig. 3.4B shows the size dependence of the QY (measurements are relative to a Rhodamine 590 standard). The high crystalline quality and efficient surface passivation permit these quantum yields for the near band edge emission to approach 20%. These particles still show strong sharp emission even after storage for more than 3 years in their original growth solution.

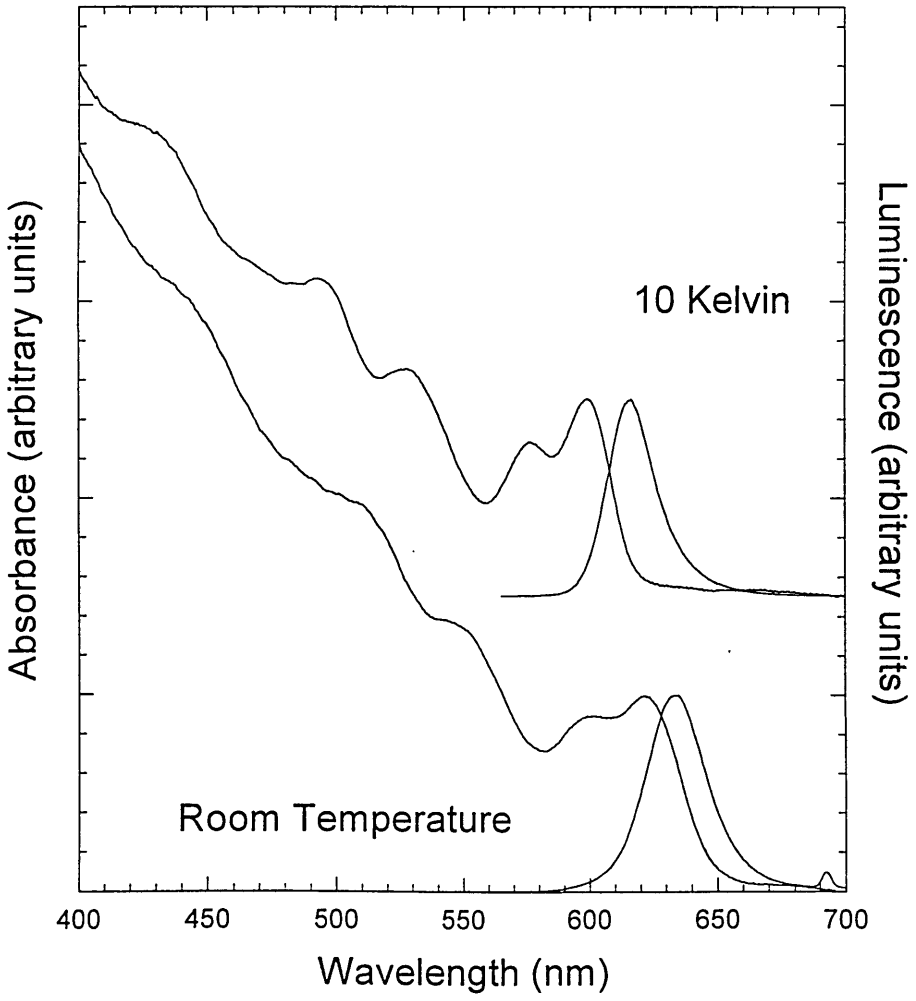

FIG. 3.5 Absorption and luminescence spectra of the 62Å diameter CdSe nanocrystallites taken at room temperature and at 10K. (C. R. Kagan)

The linewidth of each absorption and emission feature observed at room temperature is a combination of homogeneous broadening due to coupling with the phonons and the residual distributions of size, shape, and defects within the sample. The temperature dependence of the linewidths in absorption and emission are shown in figure 3.5. The blue shift of the optical features at low temperature reflects the temperature dependence of the bulk band gap. As phonon broadening is suppressed the optical transitions sharpen significantly. At low temperature the QY of the samples approaches unity. Extensive optical studies of these QD samples at low temperature now provides a detailed description of the evolution of electronic structure with size.[2-4]

3.3 References

(1) Reviews (a) L. E. Brus, Appl. Phys. A. 53, 456 (1991); (b) A. Henglein, Top. Curr. Chem. 143, 113 (1988); (c) Y. Wang and N. Herron, J. Phys. Chem. 95, 525 (1991) (d) M. G. Bawendi, M. L. Steigerwald, and L. E. Brus, Annu. Rev. Phys. Chem. 41, 477 (1991).

(2) D. J. Norris, C. B. Murray, and M. G. Bawendi, Phys. Rev. Lett. 72, 2612 (1994).

(3) D. J. Norris, Ph. D. Thesis, Massachusetts Institute of Technology (1995).

(4) M. Nirmal, D. J. Norris, M. Kuno, M. G. Bawendi, Al. L. Efros, and M. Rosen, Phys. Rev. Lett. (sumitted).

(5) Al. L. Efros and A. V. Rodina, Phys. Rev. B. 47,10005 (1993).

(6) P. E. Lippens and M. Lannoo, Phys. Rev. B 39, 10935 (1989)

(7) Al. L. Efros, M. Rosen, M. Kuno, M. Nirmal, D. J. Norris, and M. G. Bawendi (in preparation)

(8) C. R. Kagan, C. B. Murray, and M. G. Bawendi (submitted).

Chapter 4

Characterization of the Semiconductor Core and Surface

(Much of this chapter has appeared in print: C. B. Murray *et al*, J. Am. Chem. Soc. 115, 8706 (1993), M. A. Marcus *et al*, NanoSTRUCTURED MATERIALS 1, 323 (1992))

4.0 Introduction

Many studies (experimental and theoretical) of the structural evolution of small particles have focused on systems without directional bonding (metallic[1] or ionic solids[2]) while covalent solids have remained more obscure. CdSe is a polar covalent solid with highly directional bonding. In these studies we follow the transition of CdSe from the local bonding of molecules to the extended symmetry of the bulk lattice. Our CdSe nanocrystallites range in size from ~ 70 atoms in the smallest samples to greater than 70,000 atoms in the largest samples.

A model of the semiconductor core is developed by combining the results from a series of independent structural probes. We employ standard elemental analysis techniques, transmission electron microscopy (TEM), extended X-ray absorption fine structure spectroscopy (EXAFS), wide angle and small angle X-ray scattering (WAXS and SAXS) and combine all results in simple computer models. In large crystallites we highlight the importance of stacking faults and particle shape in reproducing the experimental results. The results of these studies indicate that unlike metallic and ionic systems, the structure of these polar covalent system is dominated by the local and highly directional nature of the bonding. Little evidence for isotropic lattice contractions or room "surface-pressure-induced" phase transitions at ambient pressures is found even in the smallest crystallites. We believe the significant surface free energy of these crystallites is minimized by a local relaxation of bond lengths and bond angles at the surface.

4.1 Elemental Analysis

A series of techniques have been employed to confirm the overall chemical composition of the particles produced. Elemental analysis of ensembles of crystallites by

atomic emission and X-ray absorption point to a stoichiometric CdSe core. Energy dispersive X-ray detection allows microscopic measurements of individual crystallites (limited to larger crystallites) and indicates stoichiometric particles. More detailed X-ray fluorescence studies have detected a slight excess of Se which we attribute to the presence of some TOPSe capping groups on the surface.[3] All of our structural models are compatible with these general results.

4.2 Transmission Electron Microscopy

4.2.1 Introduction: Transmission electron microscopy (TEM) allows both the imaging of individual crystallites and the development of a statistical description of the size and shape of the particles in a sample. High resolution imaging allows determination of individual crystallite morphology and internal structure. Two major mechanisms provide contrast in TEM imaging. Lattice image contrast and Z contrast provide important and complimentary information. Lattice imaging highlights the crystalline core of particles with planes oriented perpendicular to the electron beam but is insensitive to misoriented or disordered portions of the structure. When electrons are diffracted by different portions of a periodic sample they have a definite phase relation. When refocused in the image plane, an interference pattern characteristic of the lattice is generated. Specific crystal reflections can be selected by the choice of objective apertures. The aperture limits the angular range of reflections contributing to the final image. In addition to being diffracted by the crystal lattice electrons are also diffusely scattered from individual atoms. This diffuse scattering is proportional to the atomic number (Z) of the element and is referred to as Z contrast or Z scattering. Z scattering provides contrast in the disordered / misoriented regions.

4.2.2 Experimental: A Topcon EM002B electron microscope operating at 200 kV was used for transmission electron microscopy (TEM). Lattice imaging was carried out in bright field with an objective aperture selected to permit lattice imaging of the (100), (002), and (101) wurtzite planes. Smaller apertures were inserted to produce imaging with Z contrast alone. Magnifications were calibrated from the lattice fringes in the

individual particles. Copper grids (300 mesh) coated with a ~50 Å amorphous carbon film were purchased from LAD Research. Low coverage samples were prepared by placing a drop of a dilute hexane or pyridine dispersion of nanocrystallites on the surface of a grid, waiting for ~1 minute, and then wicking away the solution. The coverage level of crystallites was adjusted by varying the initial dispersion concentration and the contact time. Monolayers of crystallites were produced by placing a single drop of a dispersion of crystallites in a 95% / 5% mixture of octane/octanol directly on the grid and allowing it to slowly evaporate.

4.2.3 Results and Discussion: A large single nanocrystallite is seen in figure 4.1. The columns of atoms display the characteristic hexagonal pattern of the <002> projection. Alignment of the beam with the crystallite axes makes the imaging sensitive to faulting along axes perpendicular to the line of observation. Although there is no faulting observed in this projection, this single measurement does not ensure that the particle is a perfect wurtzite domain. There are no faults in <101> or <100> direction but this projection would not be sensitive to faulting along the <002> axis. In figure 4.2(A) a nanocrystallite with an unusually high defect density is seen. Imaged perpendicular to the <002> axis, 3 stacking faults are clearly seen. Position (a) marks a twin plane while (b) and (c) indicate faults of lower symmetry. If the particle had been oriented with its <002> axis perpendicular to the substrate, as in figure 4.1, these faults would have gone undetected. Crystallites have the bulk wurtzite structure. The stacking faults observed along the <002> axis are also the predominant form of disorder in bulk II-VI materials. The near energetic equivalence of the hexagonal and cubic modification of the CdSe lattice makes these faults a small perturbation on the energy of the particles. The recognition of their presence is essential however in understanding symmetry sensitive properties of the crystallites such as optical selection rules.

There is a broad distribution in the position and frequency of stacking faults within each sample. More stacking faults are observed near the center which may point to an increased probability of faulting early in the growth. There are indications that the smallest crystallites may contain local bonding environments consistent with both of the

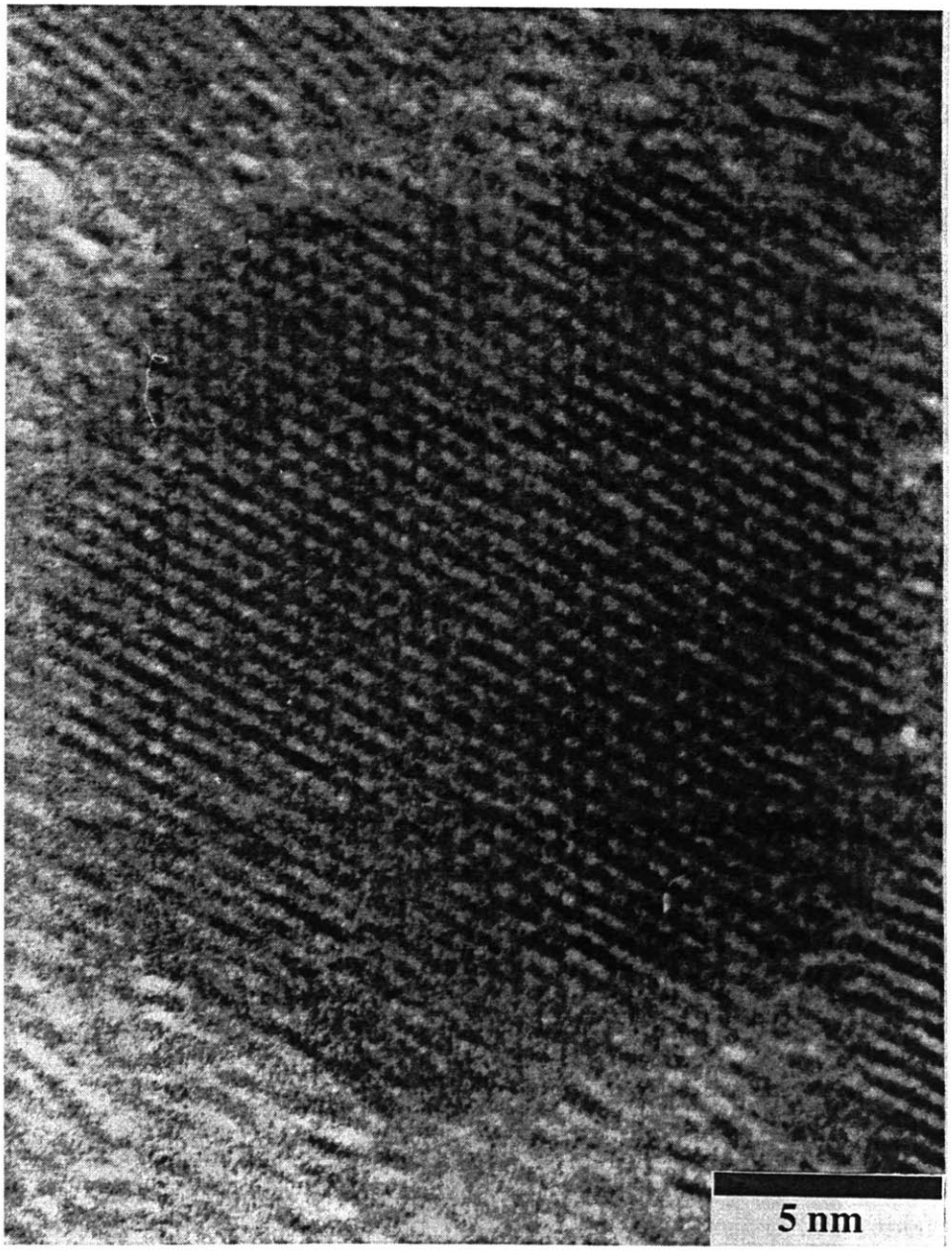

FIG. 4.1 HRTEM of a single large CdSe nanocrystallite showing the characteristic hexagonal lattice image of the <002> wurtzite projection.

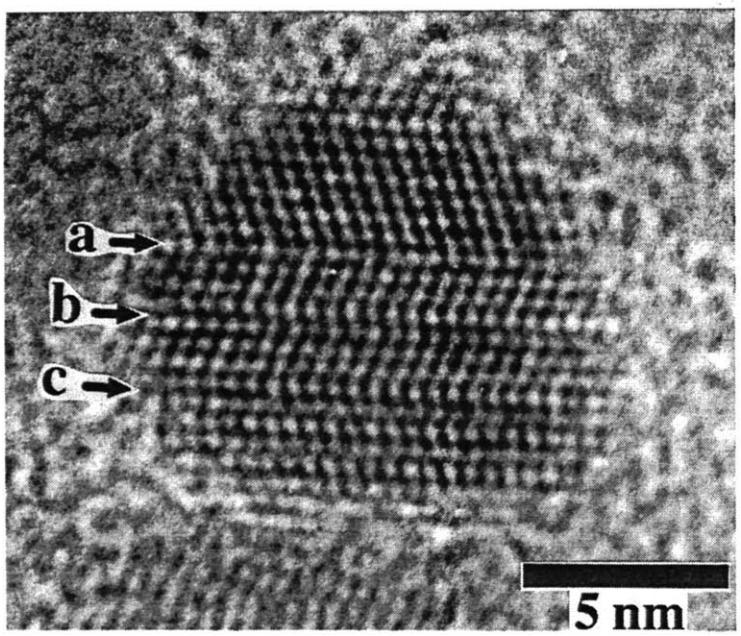

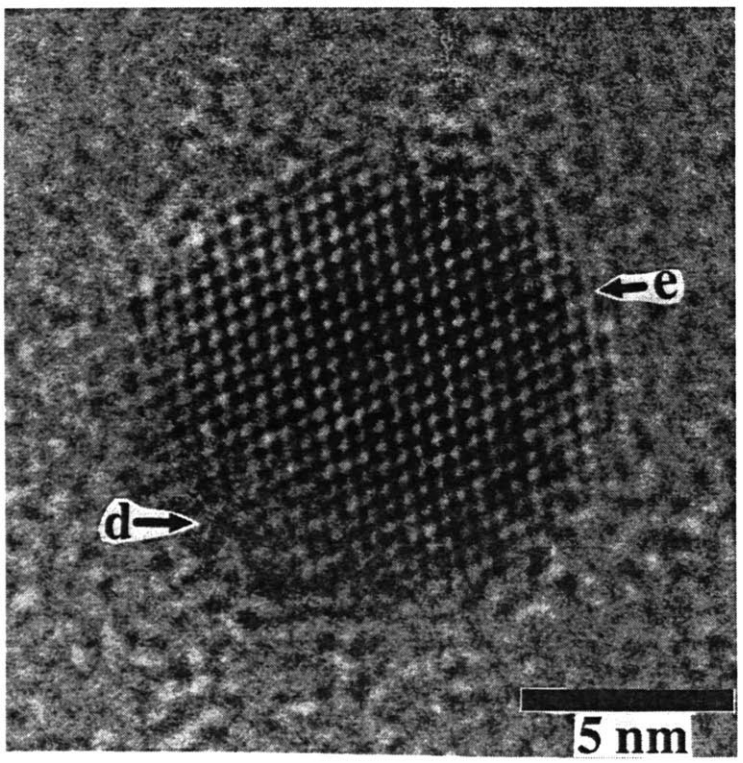

FIG. 4.2A CdSe nanocrystallite imaged perpendicular to the <002> axis. Stacking faults are clearly visible. (a) marks a twin plane while (b) and (c) mark faults of lower symmetry.

FIG. 4.2B CdSe nanocrystallite viewed perpendicular to the <002> axis, (d) marks a region of Z contrast where a portion of the crystallite is misoriented with respect to the electron beam. (e) shows the sharp lattice contrast at near optimum focus.

bulk modifications.[4] It is also possible that greater contrast in the central region improves detection of the faults. Stacking faults do become less prevalent with increasing growth temperature. The optimized growth process yields crystallites with fault densities of ~1 fault in every 10 to 12 planes (measured by X-ray diffraction). The wavy lattice patterns of individual faulted crystallites can be qualitatively reproduced in computer generated atom images by introducing stacking faults along the <002> axis. Reliable statistics on the prevalence of stacking faults are complicated by the low statistical probability of observing faults. Simple counting of the crystallites in a single image displaying stacking faults would lead to seriously inflated claims of crystallite perfection.

When particles are faulted or misoriented with respect to the electron beam more diffuse scattering from Cd and Se atoms continues to produce contrast. Figure 4.2B shows a projection of a single CdSe nanocrystallite, perpendicular to the <002> axis. The upper portion of this crystallite (e) shows clear columns of atoms while lattice contrast is lost in the region marked (d). This image highlights the importance of contributions from both lattice and Z contrast in building an accurate description of average crystallite size, shape and structure.

Extensive surveys of samples ranging from ~25 up to 150Å yield some general qualitative and quantitative results regarding crystallite size, shape, and faulting. To provide accurate size measurements, the lattice fringes of the particles are used as a standard. When Z contrast imaging is employed the magnification is first calibrated with an image showing lattice fringes and then a smaller objective aperture is inserted to eliminate the lattice image and leave only Z contrast. Comparing images taken from a single field of view, lattice contrast and Z contrast produced a statistically significant discrepancy in the measurement of crystallite radii. Radii measured with lattice contrast were approximately one monolayer of CdSe (~2.5Å) smaller than those measured with Z contrast. We speculate that a relaxed or disordered surface layer of the particles may be detected by Z contrast. In addition the periphery of the particle is often poorly resolved even in cases where the sharp internal structure demonstrates near optimum focus. Size distributions in samples after processing by size selective precipitation are nearly

Gaussian with $\sigma < 5\%$ in the major and minor crystallite axes. Loss of contrast at the edge of the crystallites makes the assignment of the final plane uncertain and introduces the principal source of experimental error.

The crystallites under study are surrounded by a diffuse capping layer of TOPO / TOPSe which uniformly reduces the contrast in each image. Processing of the particle to exchange these bulky groups for volatile pyridine yields particles with bare surfaces in the high vacuum environment of the microscope. These exchanged particles have however been shown to be increasingly sensitive to oxidation.[13] We have chosen to focus our microscopic investigations on the TOPO / TOPSe samples as these are representative of the material characterized optically.

Figure 4.3 clearly shows the natural tendency for the nanocrystals to begin hexagonally close packing at higher concentrations. This image shows several hundred prolate nanocrystals with an average size of 66Å along the <002> axis and 57Å perpendicular to the <002>axis. Figure 4.4 shows ~100 nanocrystallites from this sample at higher magnification. The apparent size of an elliptical particle is dependent on its orientation with respect to the beam. Particles with the <002> axis perpendicular to the grid are nearly circular in cross section while nanocrystals oriented in other directions appear slightly oblong. Figures 4.4 and 4.5 show the same sample at successively higher magnification. Observations of individual crystallites are carried out by sequentially expanding portions of images to the scale seen in figure 4.5. In this way a statistical picture of the sample is built up. Self-organization of the size selected crystallites into monolayers provides high contrast and maximizes the number of crystallites for analysis in a single image. The ordering of particles in 2 dimensions has been investigated by Daboussi *et al.*[5]

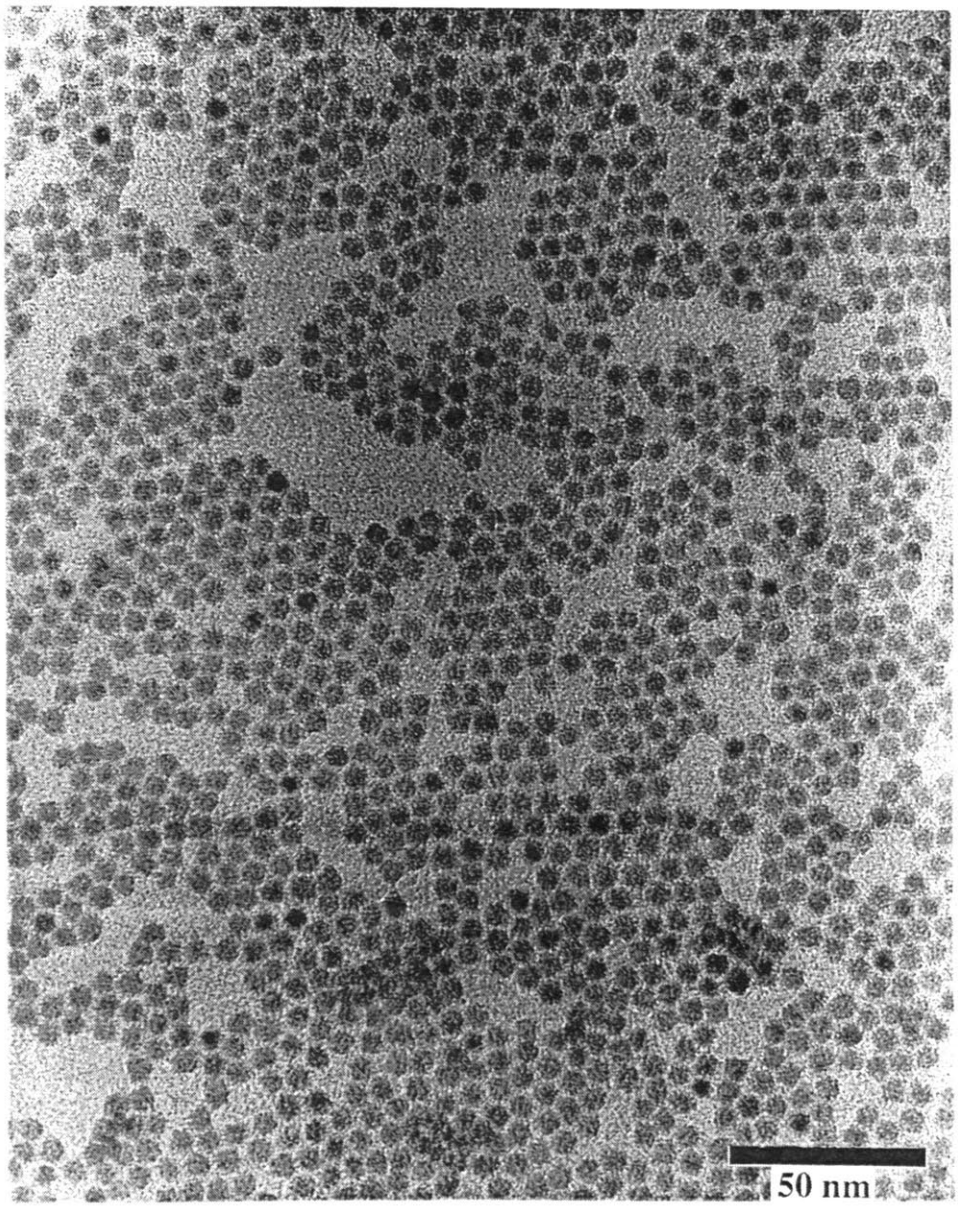

FIG. 4.3 HRTEM image shows a sample of slightly prolate CdSe nanocrystallites beginning to hexagonally close pack. Crystallites average 66Å along the <002> axis and 57Å perpendicular to the <002> axis.

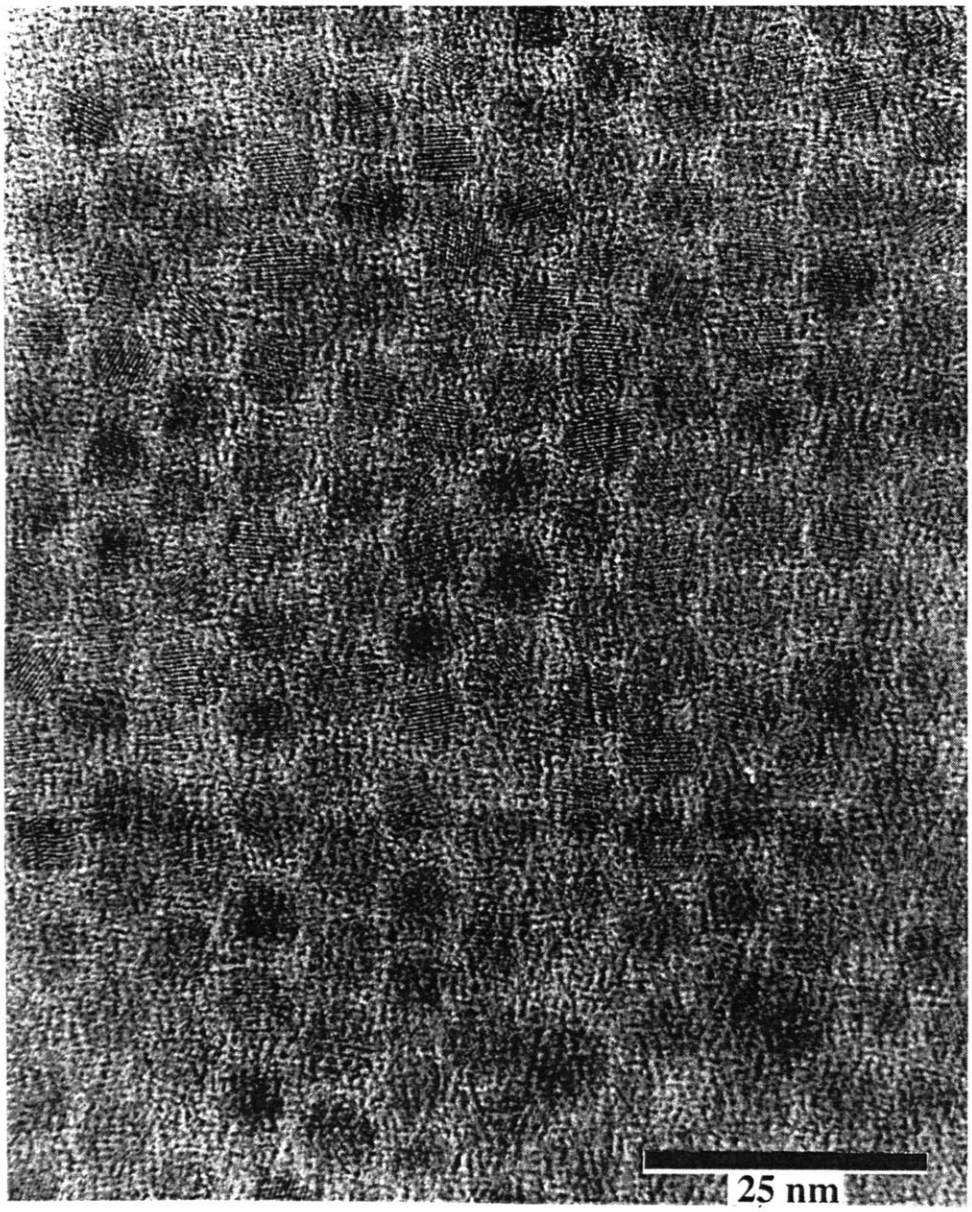

FIG. 4.4 HRTEM image shows a higher magnification image of the sample seen in figure 4.3.

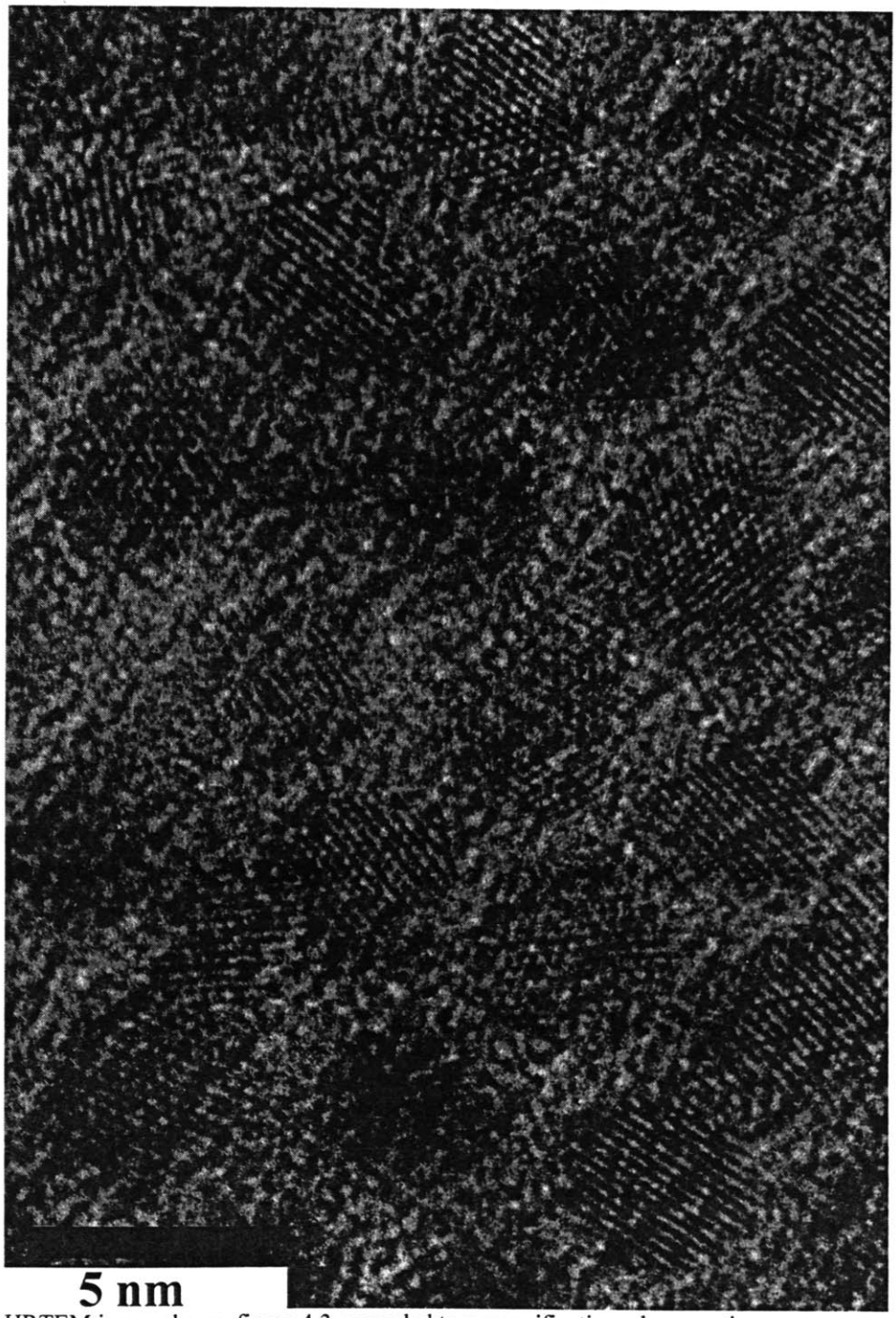

FIG. 4.5 HRTEM image shows figure 4.3 expanded to a magnification where routine measurements of crystallite sizes are made.

At higher coverage multilayers begin to form. Figure 4.6A shows hexagonal packing with a second layer forming. Measurements of particle size in such multilayers are greatly complicated by the simultaneous contribution of several layers to the lattice image. In cases like that shown in figure 4.6B it can be difficult to know where one particle ends and where the next begins. Complex Moiré fringes can also arises from the misalignment of the particles in the layers as seen in figure 4.6C. Thus measurements of monolayer structures optimizes the statistical analysis of the samples.

Preparation and observation of a series of monolayer samples yields some general results. The highest quality size selected samples display standard deviations in diameter (σ) of between 3.5 and 4.5 %. This represents a variation of less than one atomic plane on most crystallites and is thus atomic scale roughness. Loss of contrast at the periphery of each particle makes the assignment of the last plane uncertain, thus our estimates of σ are still measurement limited. When size selective precipitation is not performed sample distributions are broader with a pronounced tail in the distribution to smaller sizes as discussed earlier.

Crystallites are slightly prolate with an aspect ratio increasing as growth proceeds. Series of nanocrystalline samples isolated at intervals from a single preparation were organized into monolayers. TEM studies of these samples were used to develop a statistical model of crystallite structure. The smallest particles resolvable in the TEM (~25Å) are nearly spherical with a 20Å crystalline core and a diffuse overlayer. As growth proceeds the aspect ratio increases to 1.3 for the 80Å diameter particles. This trend is consistent with slightly faster growth of the (002) planes. The (002) planes have statistically fewer sites for coordination of capping groups than the (100) or the (101) planes and thus may experience lower steric barriers to growth. In addition, coordination may help to differentiate the surface energies of the crystal faces. Nucleation and growth of crystallites capped with pyridine and its derivatives dramatically accentuates asymmetry with aspect ratios approaching 2 to 2.5. It should be noted that bulk (002) surfaces have a lower surface energy than the perpendicular faces and thus simple surface energy arguments, in the absence of surface derivatization, would predict growth of oblate particles.

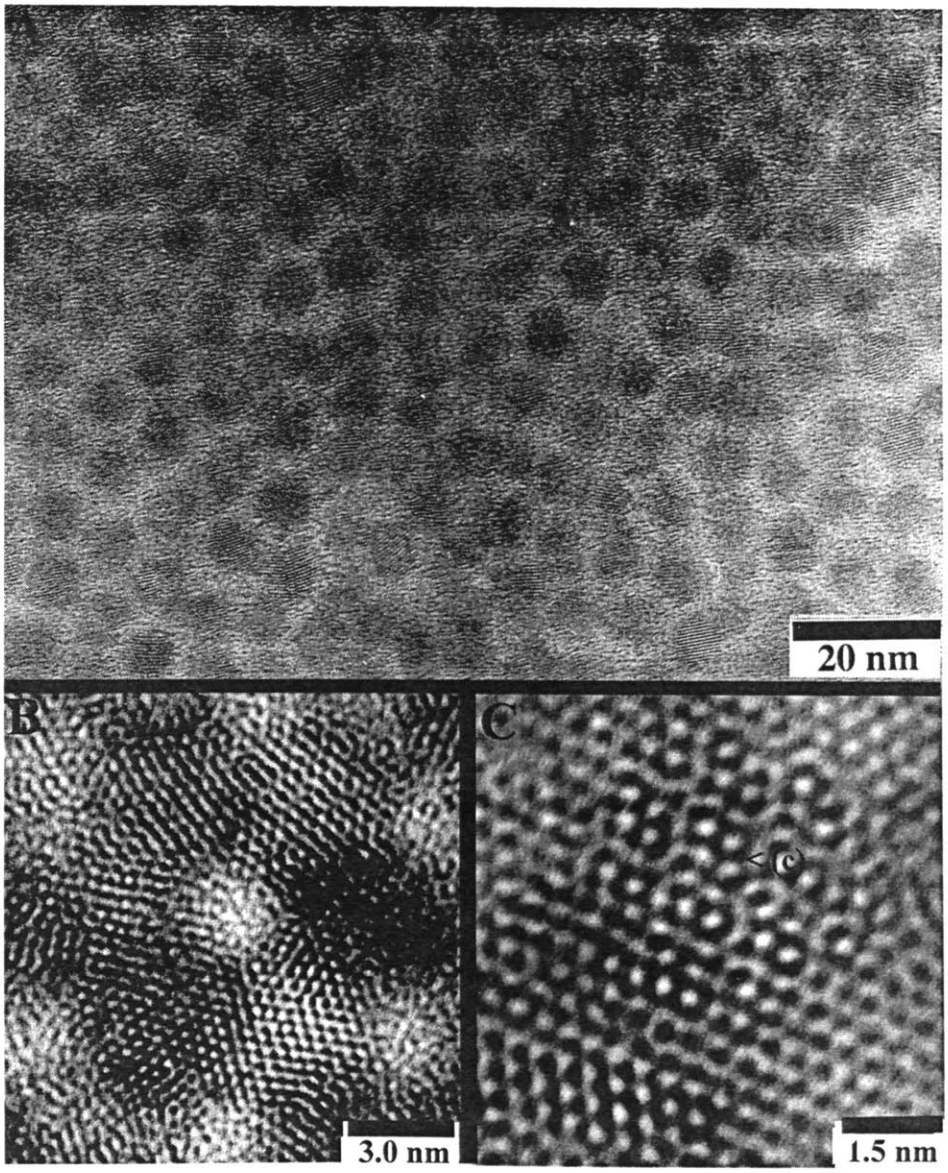

FIG. 4.6A TEM image of a region of ~64Å diameter CdSe nanocrystallites beginning to form a bilayer at high coverage.
FIG. 4.6B High magnification image showing the coherence of the lattice fringes in the bilayer. Detecting the boundaries of a single particle is difficult.
FIG. 4.6C At high magnification a bilayer of 80Å diameter particles shows Moire fringes due to the slight misalignment of an underlying crystallite.

Selected area electron diffraction patterns confirm the wurtzite structure of the crystallites. Although a common technique, selected area diffraction is not emphasized in our analysis of individual crystallites. Both bright field and dark field images indicate that our crystallites are not randomly oriented but rather that they exhibit a strong tendency to orient with their long axis parallel to the carbon substrate. The non statistical distribution of crystal orientations can greatly impair the interpretation of the electron diffraction line shapes. Electron diffraction patterns do provide an important probe of crystallite orientation that will be of increasing importance in studies of quantum dot solids.

4.3 EXAFS

4.3.1 Introduction: Nanocrystallites smaller than 25Å diameter provide great challenges in structural characterization. They are too small to provide good contrast in TEM and have too few planes to produce well resolved diffraction features. Direct measurement of the broad peak positions has lead to predictions of dramatic lattice contraction and even size dependent phase transitions.[11] An independent structural probe sensitive to the local bonding environment is essential. EXAFS spectroscopy allows the determination of both the average bond length and the distribution of bond lengths in a material.

Extended X-ray absorption fine structure (EXAFS) refers to the oscillatory character of the X-ray absorption coefficient (μ) at energies between 40 and 1000 eV above an absorption edge. These oscillations may have a magnitude of 10% or more. EXAFS is a powerful local probe of the bonding environment of the atom excited. There is no requirement for long range order. The bond lengths in both amorphous and crystalline materials may be determined with an accuracy between 0.01 - 0.03Å. The ability to isolate the signal from a single absorbing species allows investigations of dilute systems and nonstoichiometric regions that present great challenges to other structural techniques. A series of investigations of II-VI nanocrystallites was carried out in

collaboration with M. A. Marcus (AT&T Bell Labs).[6] Reference (6) details these studies. Only a summary of the methods, analysis and results are presented here.

4.3.2 Experimental: EXAFS data was taken in fluorescence on Beamline X-15 at the National Synchrotron Light Source. Si (111) monochromator crystals were used for the Se-edge data, while Si (220) crystals were used for Cd and Te. Data were taken from 200 eV below the edge to 1,000 eV above. Data were collected at both metal and chalcogenide edges to insure self consistency. Samples were prepared by drying a dispersion of nanocrystallites into filter paper. Bulk CdS, CdSe, CdTe and $Cd(OH)_2$ were employed as model compounds prepared by the methods in reference(6).

4.3.3 Results and Discussion: The probability that an X-ray photon will be absorbed by a core electron depends on both the initial and final states of the electron. An ejected photoelectron can be represented by a spherical wave originating at the absorbing atom. The photoelectron wave is back-scattered by neighboring atoms. The final state is the sum of the outgoing and back-scattered waves and thus the resulting interference gives rise to the sinusoidal variation of absorption coefficient μ with photon energy. This variation can be modeled with a short range single electron single scattering theory. [7]

The absorption coefficient μ is defined by:

(4.1) $$\mu x = \ln(I/I_0)$$

where x is the sample thickness, I is the transmitted intensity and I_0 is the incident intensity. A plot of μx vs. photon energy for a 35Å diameter sample of CdTe is shown in figure 4.7 . It is convenient to define a normalized absorption coefficient χ where:

(4.2) $$\chi(E) = [\mu(E)-\mu_0(E)]/\mu_0(E)$$

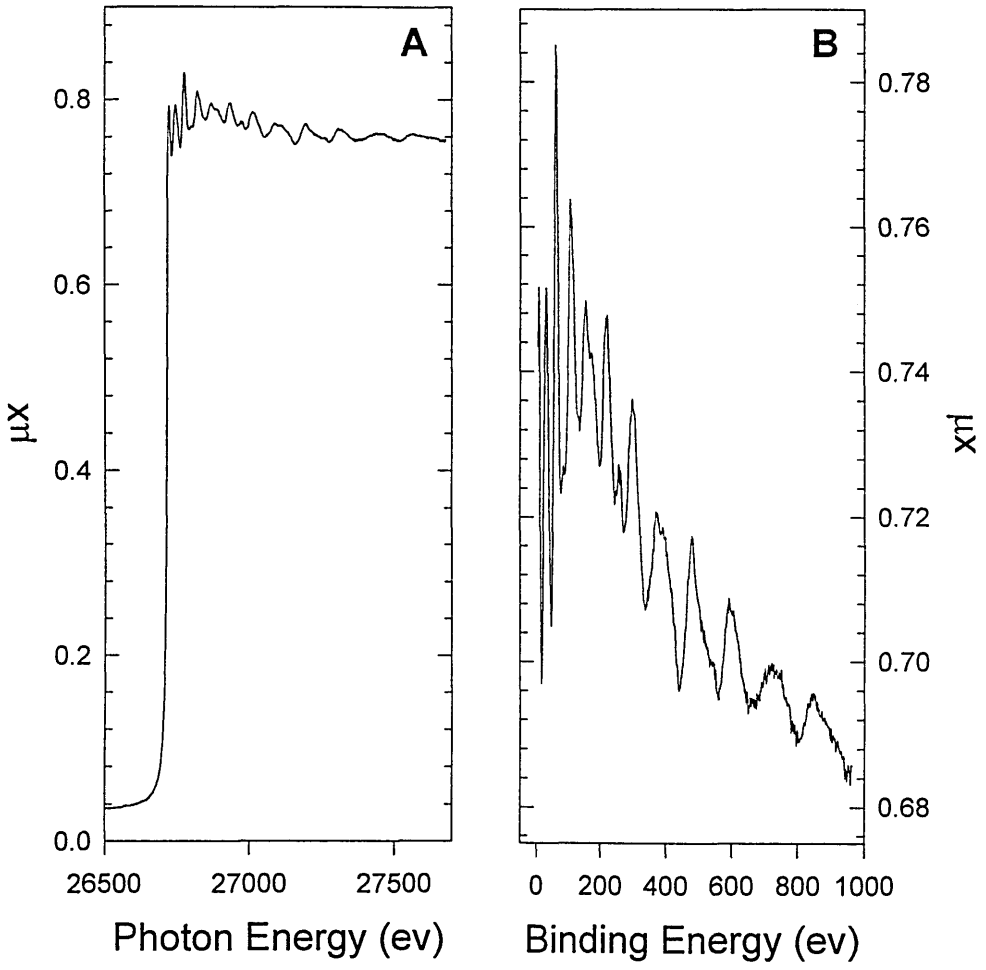

FIG. 4.7A Raw absorption (μx vs. Photon energy) at the Cd K edge in 35Å CdTe nanocrystallites

FIG. 4.7B Energy corrected (μx vs. Binding energy) at the Cd K edge in 35Å CdTe nanocrystallites

To obtain structural information we must transform $\chi(E)$ into $\chi(k)$, where k is the photoelectron wave vector

(4.3) $$k=(2m/h^2*(E-Eo))^{1/2}$$

where m is the mass of the electron, E is the photon energy and E_0 is the electron binding energy.Following this transformation the sinusoidal oscillations are accentuated for curve

fitting by plotting $k^3\chi(k)$ vs. k. This is referred to as a weighted EXAFS spectrum, an example of which is shown in figure 4.8.

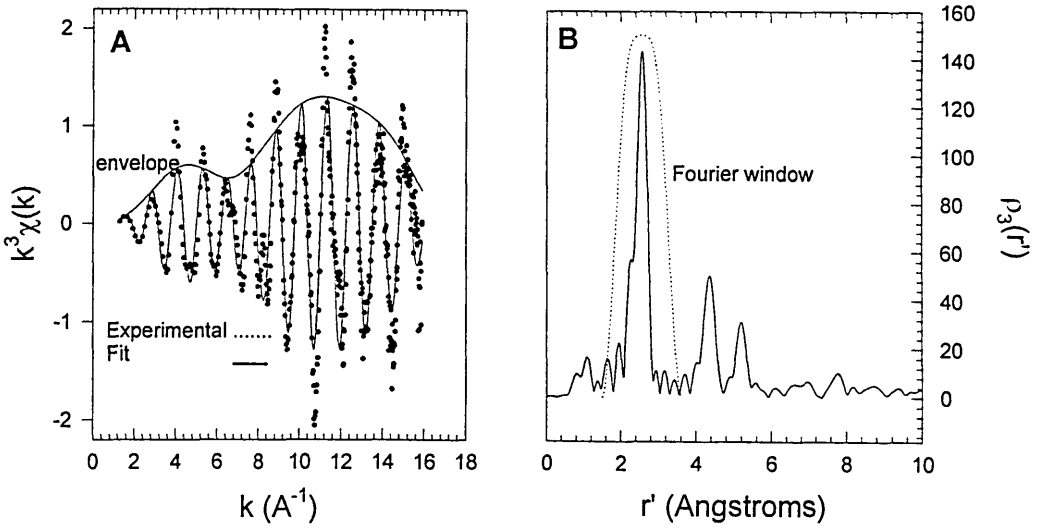

FIG. 4.8A Weighted EXAFS spectrum for 35Å CdTe taken at the Cd K edge. Experimental points are discrete points while the fit is the solid line.

FIG 4.8B Plot of $\rho_3(r')$ vs r'.

The experimental spectrum is then fit with an expression derived from the single-electron single scattering theory of EXAFS:

$$\chi(k)=\sum_j N_j S_i(k) F_j(k) e^{-2s_j k^2} e^{-2r_j/l(k)} [\mathrm{Sin}(2kr_j+f_j(k)]/ (kr_j^2). \quad (4.4)$$

$F_j(k)$ is the back-scattered amplitude from each of the N_j neighboring atoms of type j a distance r_j from the absorbing atom. Static and vibrational (thermal) disorder are modeled by a Debye-Waller factor s, where $s^2=s_{stat}^2+ s_{vib}^2$. $f_j(k)$ is the total phase shift experienced by the photo electron. The term $e^{-2r_j/l(k)}$ is due to inelastic scattering processes where l is the mean free path of the photoelectron. $S_i(k)$ is an amplitude reduction factor due to many body effects. Calculations provide the forms for $S_i(k)$, and

$F_j(k)$, while the phase shift is determined by analysis of model compounds with similar bonding environments. The vibrational contribution to disorder is eliminated by cooling the sample (~10 K). Values of N_j , r_j , and s_{stat} are then optimized. Structural information is obtained by a Fourier transformation of $k^3\chi(k)$ in k space over a finite range (k_{max} to k_{min}) to give a radial distribution $\rho_3(r')$ in r' space,

$$\rho_3(r') = \frac{1}{\sqrt{2\pi}} \int_{k_{min}}^{k_{max}} k^3 \chi(k) e^{i2kr'} dk \tag{4.5}$$

The distance of the nearest neighbor of type j, r_j is related to r' though the relation (r_j = a +r'), where a is determined by analysis of model compounds. The final presentation of the data is a plot of $\rho_3(r')$ vs. r' as seen in figure 4.8.

Studies were carried out for ~35Å and ~15Å CdE (E=S, Se, Te) nanocrystallites and yielded some general results. All samples studied showed bond lengths consistent with the corresponding bulk structures. Coordination numbers in larger crystallites approach bulk values while small crystallites show reduced coordination due to a large percentage of surface species. Measurements of average bond lengths indicate that any lattice contraction is restricted to less that 1% even in the smallest crystallites. Temperature dependent studies allow us to differentiate between thermal vibrations and static disorder. The thermal vibrational factors are always within 10% of the bulk with smaller crystallites showing a slight softening of the lattice. The static disorder also increases in smaller crystallites with a distribution of bond lengths centered within 1% of the bulk values. We speculate that this distribution of bond lengths may be the result of a surface relaxation.

4.4.0 Wide Angle X-ray Scattering (WAXS)

4.4.1 Introduction: WAXS probes a statistically large number of crystallites and can be combined with the observations of TEM and EXAFS to produce a representative model of average crystallite structure and morphology. WAXS is primarily sensitive to the size, shape, and symmetry of the semiconductor core in analogy to TEM lattice contrast imaging. There is less sensitivity, however, to a potentially relaxed / disordered surface layer. Simulations of the scattering pattern for test structures are compared with experimental results. A self consistent model is developed.

4.4.2 Experimental: WAXS spectra were collected on a Rigaku 300 Rotaflex diffractometer operating in the Bragg configuration using Cu Kα radiation. The accelerating voltage was set at 60 KV and 300 milliamp flux. Scatter and diffraction slits of 0.50° and 0.15 mm collection slits were used. Soller slits limited the vertical divergence. Samples were prepared both as pressed pellets and thin films on silicon (100) wafers. Pellets were prepared by pressing ~500 mg of dried nanocrystallite powder into 0.5 in. diameter pellets at 5000 psi. WAXS spectra were also collected from thin glassy films cast on the surface of the Si (100) wafers. Thin films are prepared by drying hexane dispersions of nanocrystallites directly on the surface of the wafers.

4.4.3 Results and Discussion: All the CdE (E = S, Se, Te) nanocrystallite samples display a predominantly wurtzite crystal structure with the lattice spacing of the corresponding bulk materials (figure 4.9). Bulk crystals of CdS and CdSe commonly exhibit the wurtzite structure when prepared at high temperature. The hexagonal modification of CdTe has been observed in thin films although to our knowledge it has not been seen in bulk crystals.

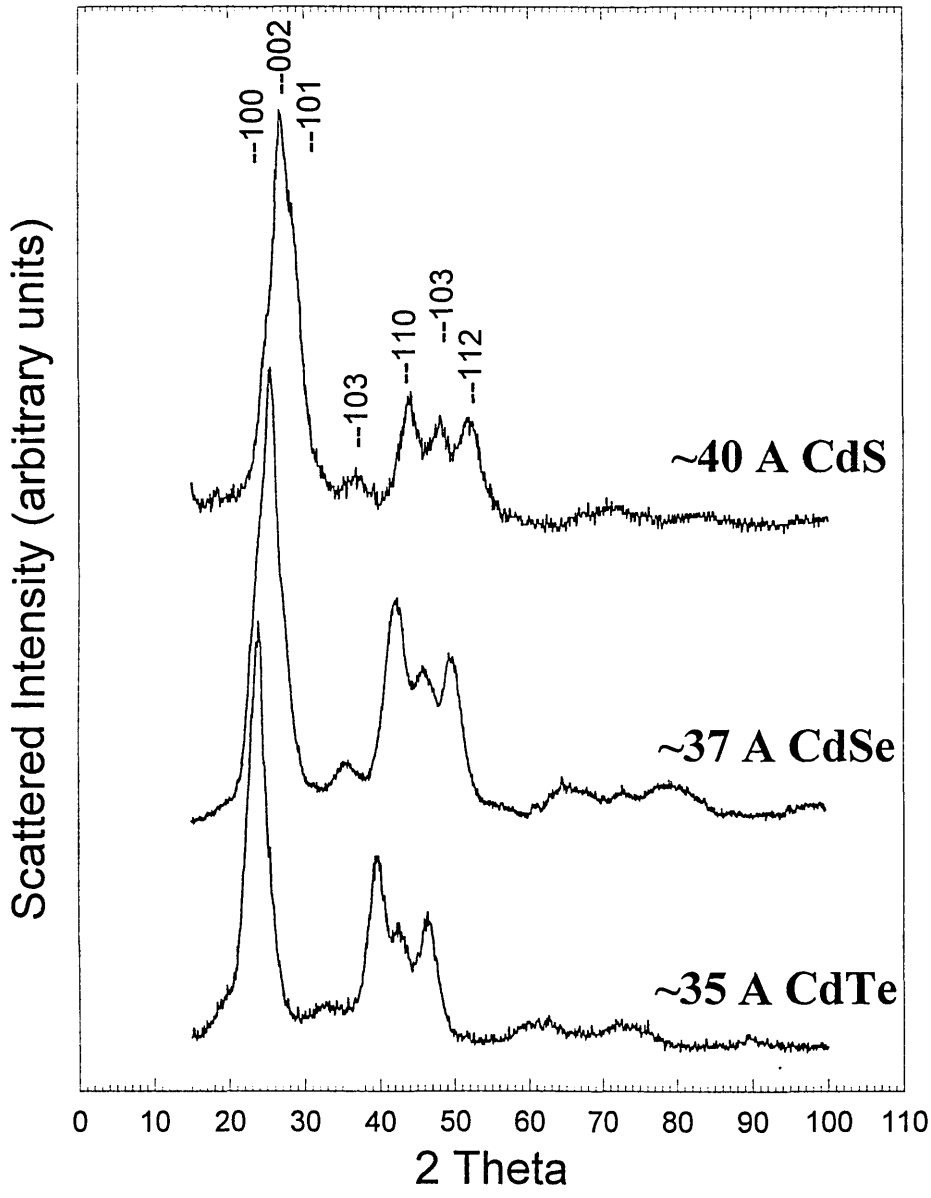

FIG. 4.11 WAXS patterns for ~30Å wurtzite CdS, CdSe, and CdTe crystallites. The positions of reflections from bulk CdSe are indicated.

Experimental WAXS patterns for CdSe crystallites ranging from 24Å up to 90Å are displayed in figure 4.10. Spectra show evidence of finite size broadening in all

reflections. Excessive attenuation and broadening in the (102) and (103) reflections are characteristic of stacking faults along the <002> axis. Reflections fit the expected positions for the bulk wurtzite lattice in agreement with the EXAFS studies.

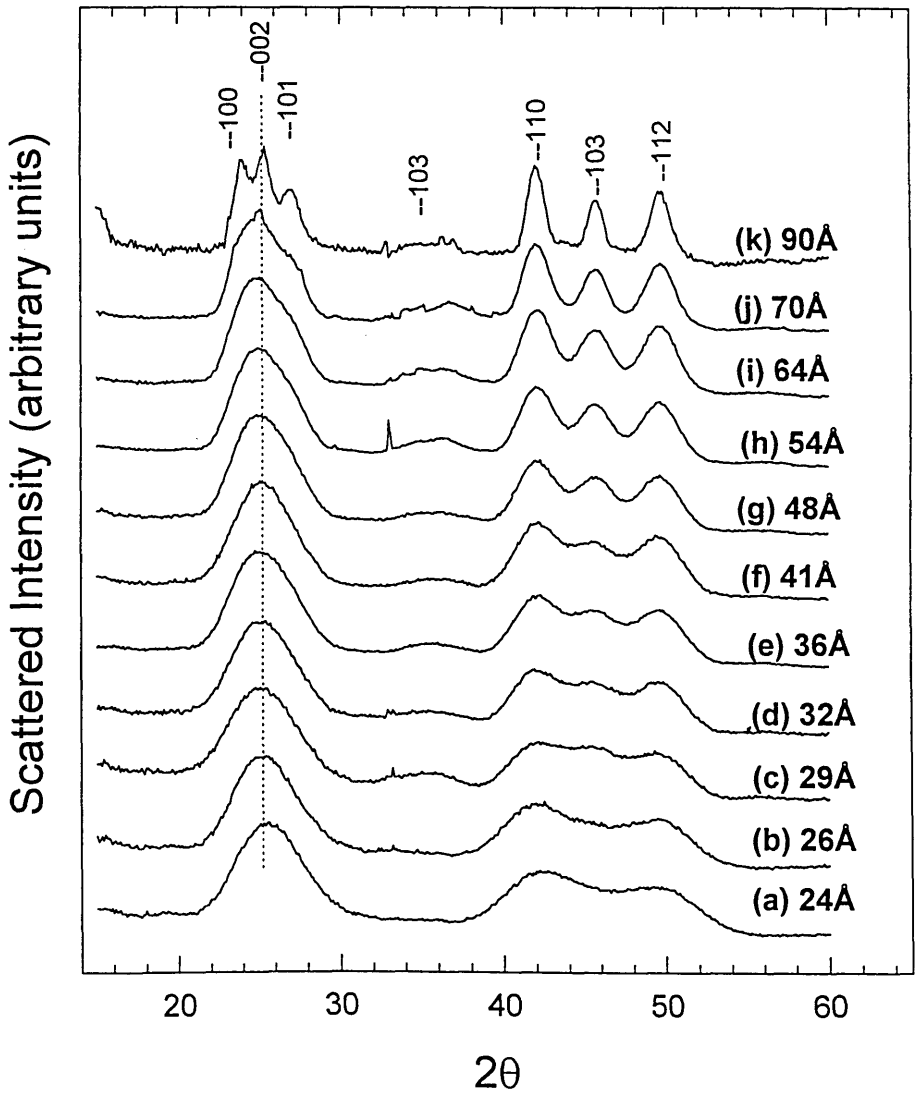

FIG. 4.10 WAXS patterns for CdSe crystallites ranging from 24Å up to 90Å. The bulk <002> reflection is indicated by a dotted line.

The first diffraction feature is a convolution of several reflections and thus its average position and width are not appropriate for simple estimates of lattice parameters or crystallite size. These small clusters possess too few atoms to define a core crystal structure making the distinction between wurtzite and zincblende meaningless. The change in the lattice diffraction features may indicate significant surface reconstruction or change in the shape of the crystallites. The diffraction patterns of the smallest members of the size series (17Å to 22Å) are shown in figure 4.11. In monodisperse samples the shift in peak position is not gradual with decreasing size. In a very small size range the spectra undergo a dramatic transition as the core atoms disappear. In the 17Å structures less than a dozen atoms can maintain full second nearest neighbor shell. Thus these crystallites are almost entirely surface species. Proper structural analysis of these nearly molecular species will require the isolation of materials as single crystals.[4]

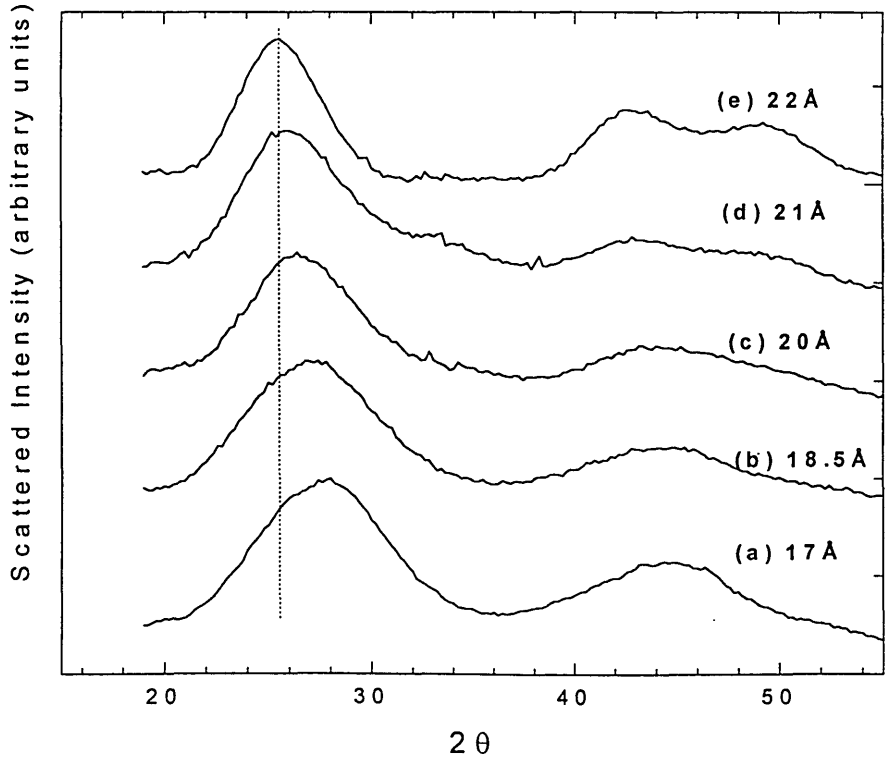

FIG. 4.11 WAXS patterns for a series of CdSe nanocrystallite samples 17Å up to 22Å. Dotted line marks the position of the bulk <002> reflection.

As mentioned the combination of finite size and defect broadening results in a convolution of peaks. Direct observation of peak position and peak width are thus unreliable measures of lattice spacing and crystallite size. But structural information can be extracted by using TEM observations to guide in fitting experimental X-ray diffraction spectra. Previous studies of the X-ray powder patterns of CdSe nanocrystallites have demonstrated the sensitivity of spectra to the presence of planar disorder and thermal effects.[8] These studies are extended here to probe the evolution of crystallite structure with size. The importance of crystallite shape, the possibility of lattice contractions, and probable surface disorder are investigated.

The Debye equation which is valid in the kinematical approximation is shown in equation 4.6. [8]

$$I(q) = I_0 \sum_m \sum_n F_m F_n \frac{\sin(qr_{m,n})}{qr_{m,n}} \tag{4.6}$$

where I(q) is the scattered intensity, I_o is the incident intensity, q is the scattering parameter [$q = 4\pi\sin(\theta)/l$] for X-rays of wavelength l diffracted through angle θ. The distance between atoms m and n is r_{mn}. A discrete form of the Debye equation is shown in eguation (4.7).[9]

$$I(q) = I_o \frac{f^2(q)}{q} \sum_k \frac{\rho(r_k)}{r_k} \sin(qr), \tag{4.7}$$

where I_o is the incident intensity, f(q) is the angle dependent scattering factor, and q is the scattering parameter [$4\pi\sin(\theta)/\lambda$] for X-rays of wavelength λ diffracted through angle θ. The sum is over all inter atomic distances, and $\rho(r_k)$ is the number of times a given interatomic distance r_k occurs. Since the number of discrete interatomic distances in an ordered structure grows much more slowly than the total number of distances, using the discrete form of the equation is significantly more efficient in the simulation of large crystallites.[9]

Atomic coordinates for the simulated clusters are obtained by systematically generating atomic positions for a crystalline lattice and retaining only those atoms falling within a defined ellipsoid. Planar disorder along the <002> axis was reproduced by creating a collection of coordinate files with a broad distribution of stacking faults about the center of the crystallites. The resulting spectra were statistically weighted and summed to create a crystallite sample distribution with a defined average defect density. Thermal effects were simulated by the introduction of a Debye-Waller factor.[8] A constant Debye-Waller factor was used based on a mean-square displacement of 0.040 $Å^2$ for each of the atoms. Samples grown at temperatures < 200°C show greater static disorder and hence require an increase in the Debye-Waller factor. The experimental spectra are subtly influenced by the combined effects of experimental geometry, variable absorption of X-rays and broad diffuse background due to contributions of incoherent scattering and the influence of the organic capping groups. Rigorous correction for these contributions to the line shape requires knowledge of sample density not presently available. A constant background chosen to best fit the relative intensity at the base of the (110) reflection is added to all simulated spectra to crudely compensate for the experimental contributions to the line shape. Average size and shape determinations from TEM images define dimensions of the ellipsoid for the simulations.

The (110) spacing is present in both the wurtzite and zincblende structures and is thus unaffected by the presence stacking faults along the <002> axis. This spacing also has reasonable separation from neighboring reflections. The line shape of the (110) reflection is thus the most robust to the effects of defect broadening and is chosen for normalization of all spectra. Crude estimates of particle size based on the Scherer analysis of peak width should employ the width of the (110) feature rather than the convolution of (100), (002) and (101) reflections found in the first diffraction feature.

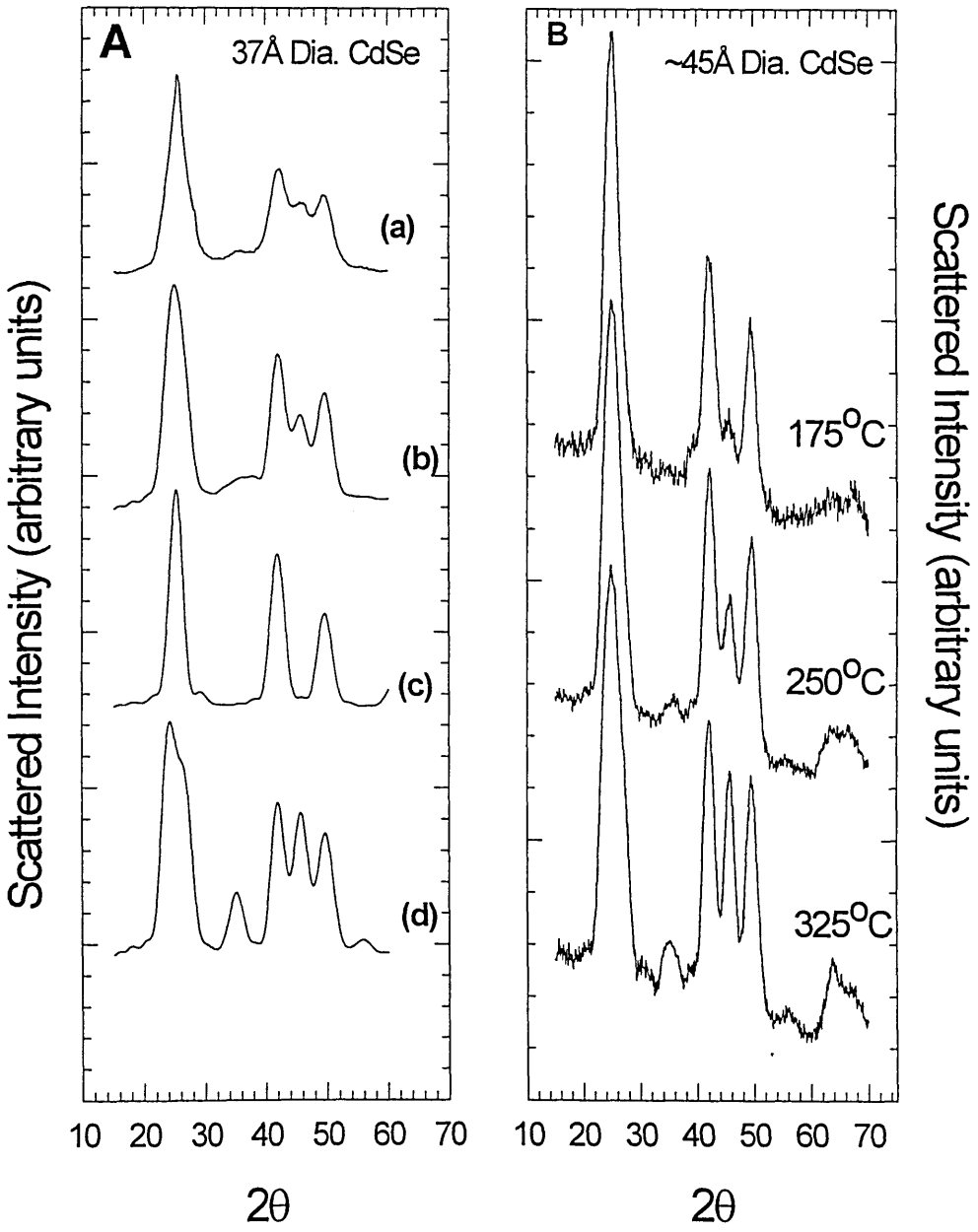

FIG. 4.12 (A) compares the calculated spectra of 1000 atom spherical particles (~37 Å diameter) of CdSe with the experimental powder pattern of a sample grown at ~250C and containing ca. 1000 atoms (a). The spectrum of defect free zincblende (c) and wurtzite (d) crystallites do not reproduce the overall shape of the experimental spectrum. The introduction of a single stacking fault near the center of an otherwise purely wurtzite crystallite greatly improves the fit (b). Increasing growth temperature results in a decrease in the prevalence of stacking faults. Panel (B) shows how growth temperature can be used to influence crystal perfection.

This convolution is often incorrectly labeled as the (111) zincblende reflection and used to estimate particle size. Figure 4.14 highlights the sensitivity of simulations to crystallite shape. The experimental spectrum of a sample of CdSe nanocrystallites, containing on average ca. 10000 atoms, is compared with simulations. The best fit obtained assuming spherical particles (a) and prolate particles with an aspect ratio of 1.3 (b) are shown. Each simulation has an average defect density of 3 stacking faults per crystallite. The particles have more (002) planes making the (002) peak the predominant reflection in the first diffraction feature. The greater coherence length results in the narrowing of the (002) reflection and less overlap with the neighboring (100) and (101) reflections. Inclusion of the prolate nature of the particles, observed in TEM, is essential to reproducing the convolution of the (100), (002), and (101) reflections in the first diffraction feature. These crystallites are sufficiently large that the contribution of surface effects may be neglected from the overall line shape.

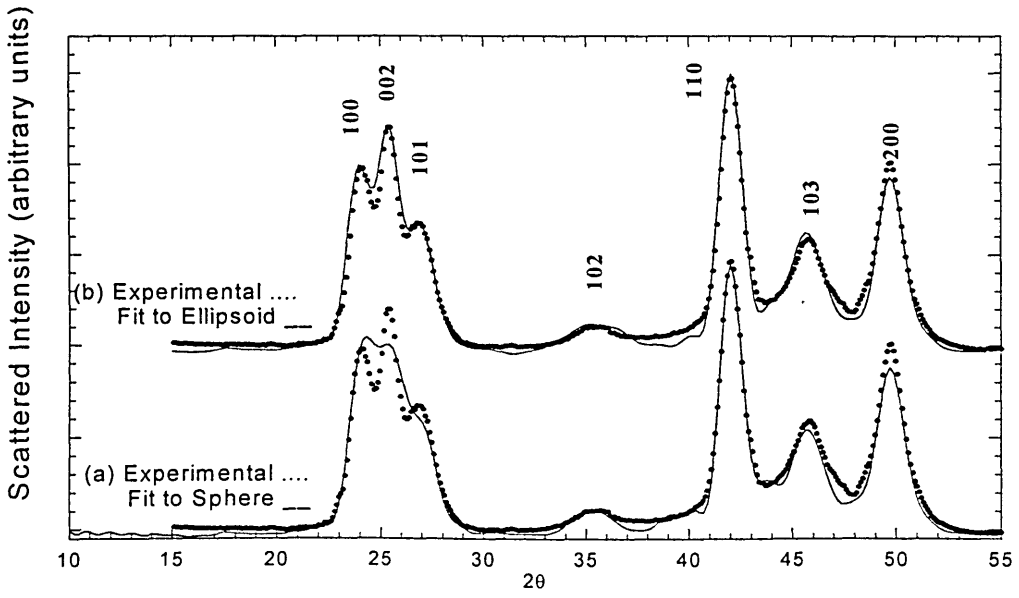

FIG. 4.13 WAXS patterns for CdSe nanocrystallites containing ~10,000 atoms. Discrete points show the experimental data while solid lines in (a) and (b) show the fits to spherical and ellipsoidal model structures detailed in the text.

The broad diffraction features of the smallest crystallites, when compared with the bulk, are shifted to higher scattering angles. An isotropic lattice contraction due to contributions of surface tension has been proposed as a possible explanation for similar observations in CdS nanocrystallites.[11] This model of gradually decreasing bond lengths is inconsistent with the EXAFS investigations. In fact the observation of a gradual shift may be largely an artifact of polydispersity as it can be reproduced by mixing back portions of our nearly monodisperse fractions to build a broader distribution. In figure 4.15 the experimental spectrum of small CdSe crystallites with ca. 275 atoms is compared with a simulation of 275 atom spherical particles (a) with a bulk lattice parameter while the spectrum of spherical particles with a lattice parameter contracted by 2% is displayed in (b). A constant defect density of 1 stacking faults / crystallite was employed in all simulations. The assumption of spherical particles leads to a poor agreement thoughout the spectrum and might initially lead observers to suspect a significant lattice contraction. The imposition of a 2 % contraction reproduces the position and general shape of the first diffraction feature but results in a poor fit at higher angles. The effect of average crystallite shape on the simulated diffraction pattern is investigated in figure 4.14 . The experimental pattern for CdSe crystallites containing ca. 275 atoms is compared with the simulation of 275 atom particles where the spherical symmetry of the particles is broken. Prolate particles with an aspect ratio of ~1.3, bulk lattice parameters, and one stacking fault per crystallite were used (c). The introduction of crystallite shape greatly improves the fit to experimental data. The prolate shape of the crystallites results in the prominence of the (002) reflection, skewing the first diffraction feature to higher scattering angles. Fits employing the crystallite's prolate nature reproduce the position and general shape of reflections but show a lack of intensity in a broad region between 27 and 33 degrees.

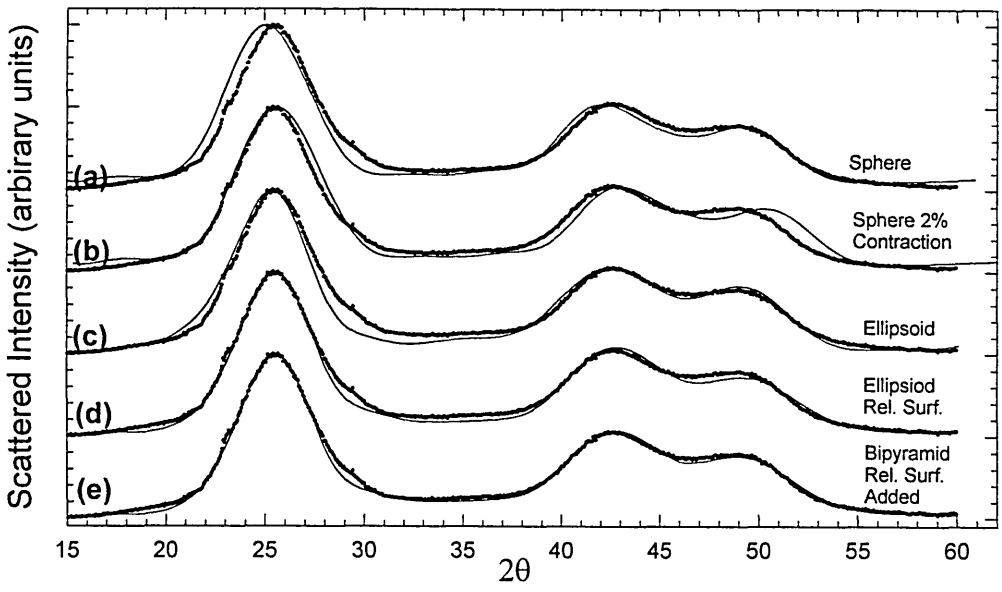

FIG. 4.14 WAXS patterns for CdSe nanocrystallites with ~275 atoms. Discrete points are the experimental data while the solid lines show the results of calculations on a series of model structures. (a) Sphere, (b) Sphere with 2% lattic contraction, (c) Ellipsoid, (d) Ellipsoid with relaxed surface, (e) Bipyramid with relaxed surface added (addition of the surface layer makes this a 350 atom structure).

TEM observations suggesting poorly resolved facets and the presence of a disordered surface layer limit the accuracy of each measurement to no better than one atomic plane (±2.6Å). The sensitivity of WAXS to the presence of surface disorder was investigated through the use of calculated spectra. The presence of surface disorder is simulated by the relaxation of all atoms lacking their full coordination shell. The poorly defined crystal surfaces make the choice of a specific relaxation difficult. Studies by Duke and Wang on clean II-VI surfaces in high vacuum have established general mechanisms for reconstruction on cleavages faces.[12] A general tendency for a bond length conserving rotation of surface II-VI pairs results in the cation relaxing into the surface while the anion is pushed out of the plane. A zero'th order attempt to retain the character of this relaxation, has been made in our simulations by radially translating all surface cations 0.40 Å toward the cylindrical axis of the crystallite. The surface anions

are translated outward 0.20 Å. The magnitude of the relaxation is chosen to provide the best fit to experimental data. The average bond length of even a 275 atom crystallite remains within $\pm$0.005 Å of the bulk value, consistant with EXAFS experiments. The fit displayed in figure 4.14 spectrum (d) shows that agreement with experimental spectra in the region $2\theta = 27^{\circ}$ to 33° can be improved by the introduction of surface disorder. Attenuation of reflections at higher angles results from the effective increase in the static disorder. If however a relaxed monolayer is added to the prolate particle all regions of the spectrum are improved. This overlayer corresponds to the sizes measured by TEM with Z contrast scattering.

The choice of the relaxation is not unique and is not an attempt to define specific surface structure nor is the choice of crystallite shape unique. The information content in these broad diffraction patterns is however too low to rigorously define the shape of the particles. The ellipsoidal model illustrates the powerful influence of particle shape on these patterns but with broad features the fits are not unambiguous. The small particles are expected to have geometries dominated by local bonding and more angular structures are anticipated. Angular structures related to trigonal-bipyramids, for example, of the retain an approximate ellipsoidal shape having a single elongated axis.

Ultimately, the smallest species are believed to resemble the pyramidal cluster isolated by Wang *et al.*[4] Although we have attempted to analyze as thoroughly as possible the line shapes of the patterns, the limits of the utility of powder diffraction are clear. The importance of our use of several independent structural probes is highlighted. EXAFS provides more reliable results in the small size limit.

The WAXS patterns of a series of CdSe samples can be fit with computer simulations which include parameters from TEM experiments and the assumption of bulk lattice parameters to provide a self consistent description of nanocrystalline CdSe samples. In figure 4.15 the experimental spectrum of a sample of crystallites containing ~1,100 atoms (solid circles) is compared with a simulation of crystallites with a defect density of 1.25 stacking faults / crystallite and spherical symmetry (solid line) and that of an ellipsoidal particle (dotted line) with an aspect ratio of ~1.2 and a relaxed surface.

These particles are too small to ignore surface contributions yet have reflections sharp enough to show strongly the influence of particle shape. The inset shows an expanded view of the first peak clearly showing the influence of particle shape. In addition an oscillation in the small angle portion of the simulation is seen. The simulation has not included the influence of a size distribution, this oscillation is the form factor characteristic of the model structure in the simulation.

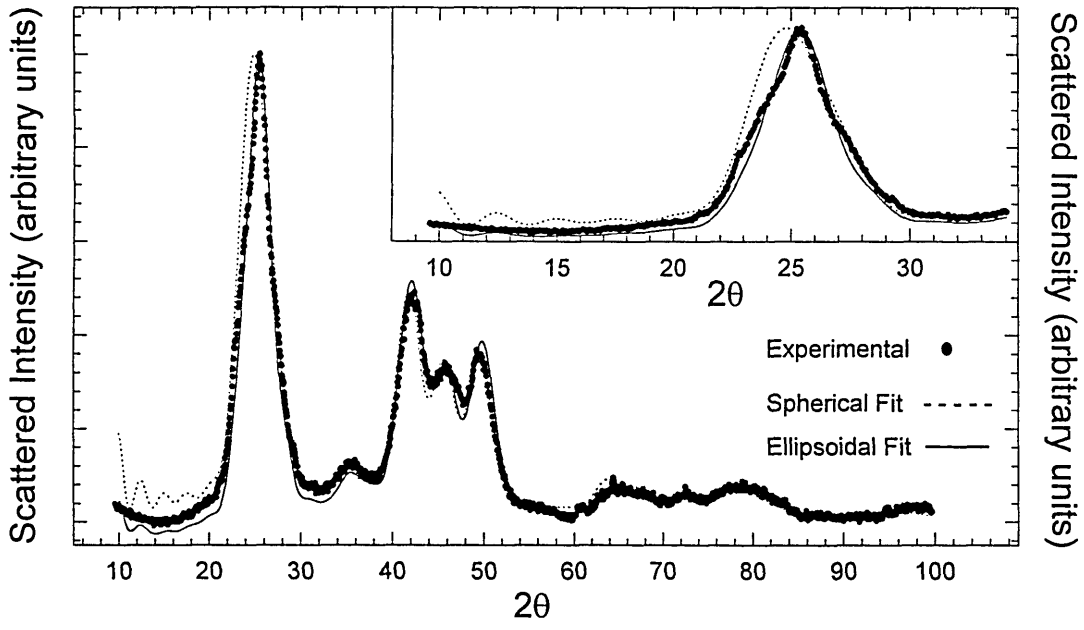

FIG. 4.15 WAXS patterns for CdSe nanocrystallites with 1,100 atoms. Experimental data are shown as discrete points, fit to a spherical model (------) and ellipsoidal model (———). Oscilations are seen at small angles due to the size and shape of the model structures.

We assert that shape has an important influence on the interpretation of the diffraction spectra. This can be highlighted by the use of two modification of the synthetic preparation which give different shaped particles. Slow growth by Ostwald ripening at ~300 °C yields ellipsoidal particles (a) while the rapid growth at 350 - 380 °C (after Bowen Katari *et al*)[13] yields spherical particles (b). Figure 4.16 displays the

experimental diffraction patterns (solid circles) and corresponding fits. Curve (a) represents a 4,450 atom ellipsoidal crystallite with a 1.2 aspect ratio and one fault per crystallite. Curve (b) corresponds to a fit with a 4,500 atom sphere with a stacking fault density of 0.75.

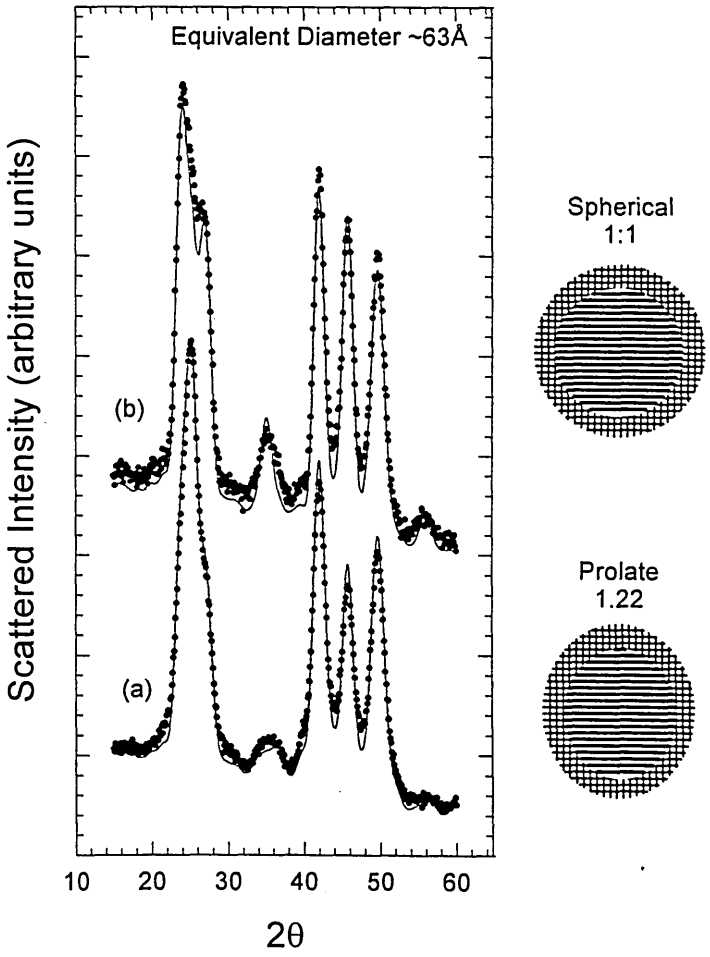

FIG. 4.16 WAXS patterns of ~63Å diameter CdSe samples displaying different shapes. Eperimental data are discrete points, fits are shown as solid lines. Sample (a) was grown slowly at ~300°C while (b) was grown rapidly at temperatures between 350 °C and 380 °C.

The combination of structural studies allows the development of a description of the average core structure of our CdSe nanocrystallites. Strict classifications of purely

wurtzite and zincblende crystal structures are potentially misleading. Crystallites grown slowly at high temperatures (~300°C) exhibit diffraction patterns consistent with a predominantly wurtzite structure with an average of one defect in every 10 planes. The presence of planar disorder cannot be ignored in the interpretation of diffraction spectra and may be important in understanding the influence of structure on the electronic properties and phase stability of nanocrystallites. Crystallite shape results in greater coherence length in the <002> direction and provides a potential explanation for the "apparent shift" in the first diffraction peak without requiring significant lattice contractions or phase transitions. Further narrowing of sample size distributions indicates the gradual shift with size may be an artifact of polydispersity. Fits to X-ray diffraction spectra can be improved by the introduction of surface disorder. The technique, however, lacks the sensitivity to uniquely define surface structure.

4.5 Small Angle X-ray Scattering

4.5.1 Introduction: Small Angle X-ray Scattering SAXS studies are sensitive to shape, size and size distribution of particles in a sample regardless of crystal perfection. Thus information gained is complementary to that of the WAXS studies which are largely sensitive to the crystalline core and relatively insensitive to aperiodic regions and to the presence of a size distribution. Systematic discrepancies in SAXS and WAXS thus provide insight into the morphology of aperiodic regions like the inorganic surface. Simultaneaous fitting of both WAXS and SAXS with the results of independent TEM and EXAFS studies completes our model of the inorganic portion of our capped nanocrystallites.

4.5.2 Experimental: Small Angle X-ray Scattering (SAXS) patterns were collected in reflection geometry on a Rigaku 300 Rotaflex diffractometer with a 250 mm focusing circle. The accelerating voltage on the Cu anode was set at 50 KV and a flux of 300 milliamps for investigation of $2\theta = 4^{o}$ to 15^{o} while the flux was reduced to 50 milliamps

to examine the region between $2\theta = 1^{\circ}$ and 4°. Diffraction and scatter slits of $1/6^{\circ}$ and 50 μm collection slits and further 150 μm receiving slits were employed. Soller slits were used to limit vertical divergence. This geometry permitted resolution limited peak widths to 0.07° fwhm at 2° 2θ. Data was collected in 0.02° steps, averaging for 10-60 seconds per point.

A typical sample preparation involves the production of a stock polymer solution containing 10% PVB, 1% n-butyl benzene, 0.1% TOP and 0.1% TOPO, all in toluene capped with a septum seal. This viscous solution is heated to 60°C and sonicated for 1 hour. A 10 mg portion of size selected CdSe nanocrystallites is placed in a vial and dispersed in 2 mls dry toluene. After the nanocrystallites are thoroughly dispersed, one ml of the polymer stock solution is added to the vial and the mixture is heated under argon to 60°C and gently stirred until homogeneous (~20 min). The pressure above the dispersion is then gently lowered allowing the excess toluene to evaporate. When the total volume is reduced to 1 ml and the dispersion has a viscosity comparable to glycerol it is spread on a silicon (100) substrate to a thickness of ~1mm. The substrate is placed in an oven and allowed to evaporate at ambient pressure and 80°C to produce a uniform film ~100 μm thick containing ~1% by weight CdSe.

4.5.3 Results and Discussion: SAXS is sensitive to the presence of the disordered layer and a powerful probe of both the dispersed crystallites and the assembled solids. Earlier WAXS studies of these nanocrystallites employed the Debye equation (equation 4.6) to aid in analyzing the structure of CdSe nanocrystallites.

Studies have thus far concentrated on the analysis of the WAXS patterns and highlighted the importance of stacking faults, crystallite shape and the presence of a disordered / relaxed surface layer in reproducing experimental X-ray patterns. Application of the discrete form of this equation to a collection of atomic coordinates allows the calculation of the scattering intensity for all angles and thus simultaneously predicts the SAXS and WAXS patterns for an arbitrary test structure. These calculations of monodisperse collections of CdSe crystallites display strong oscillations in the small angle portion of the spectrum, seen previously in figure 4.16. The experimental curve in

figure 4.15 was collected from a pressed pellet sample which was not size selected. We did not appreciate the full significance of this ringing pattern until similar oscillations were revealed in experimental patterns of our nearly monodisperse samples.

SAXS studies of dilute dispersions of the CdSe nanocrystallites in PVB (1% by weight) allows the experimental observation these oscillations. Figure 4.17 shows the experimental scattering pattern (solid circles) for a ~64Å sample of CdSe nanocrystallites from $2\theta = 1^{\circ}$ up to 60°. Data for $2\theta = 1^{\circ}$ to 10° was collected from a sample dispersed in a 100 μm thick PVB film spread on the surface of a (100) silicon wafer. It was necessary to collect the data from 1° to 4° with low X-ray flux and rescale the data due to the intense scattering in this angular region. Patterns from 10° to 60° were collected from a film deposited directly on the surface of a (100) oriented silicon substrate. Background scattering from a 100 μm film of the PVB was subtracted from the experimental pattern. Low concentrations of particles combined with interference from the polymer matrix to prevent collection of the WAXS pattern from the PVB film. Improvement in the computer algorithm to average over a Gaussian distribution of sizes allows these experimental patterns to be fit with a hypothetical ensemble of crystallites. The solid line running throughout the data is the result of a calculation for an ensemble of CdSe nanocrystallites displaying a Gaussian distribution in size ($\sigma = 4.2\%$) centered around 4,500 atoms. Scattered intensities from the SAXS and WAXS portions of the calculation were scaled separately to fit the respective experimental data. Each nanocrystallite is prolate with an aspect ratio of 1.2 and with a crystalline core containing on average one stacking fault per particle. Crystalline cores are surrounded by a monolayer of CdSe relaxed by the methods described earlier. The addition of a relaxed surface layer has only subtle effects on the WAXS pattern but dramatically influences the period of the oscillations in the small angle region. It should be noted that random displacements of the surface Cd and Se coordinates comparable in magnitude to those of the specific relaxation produced similar results. The explicit surface morphology still remains unresolved.

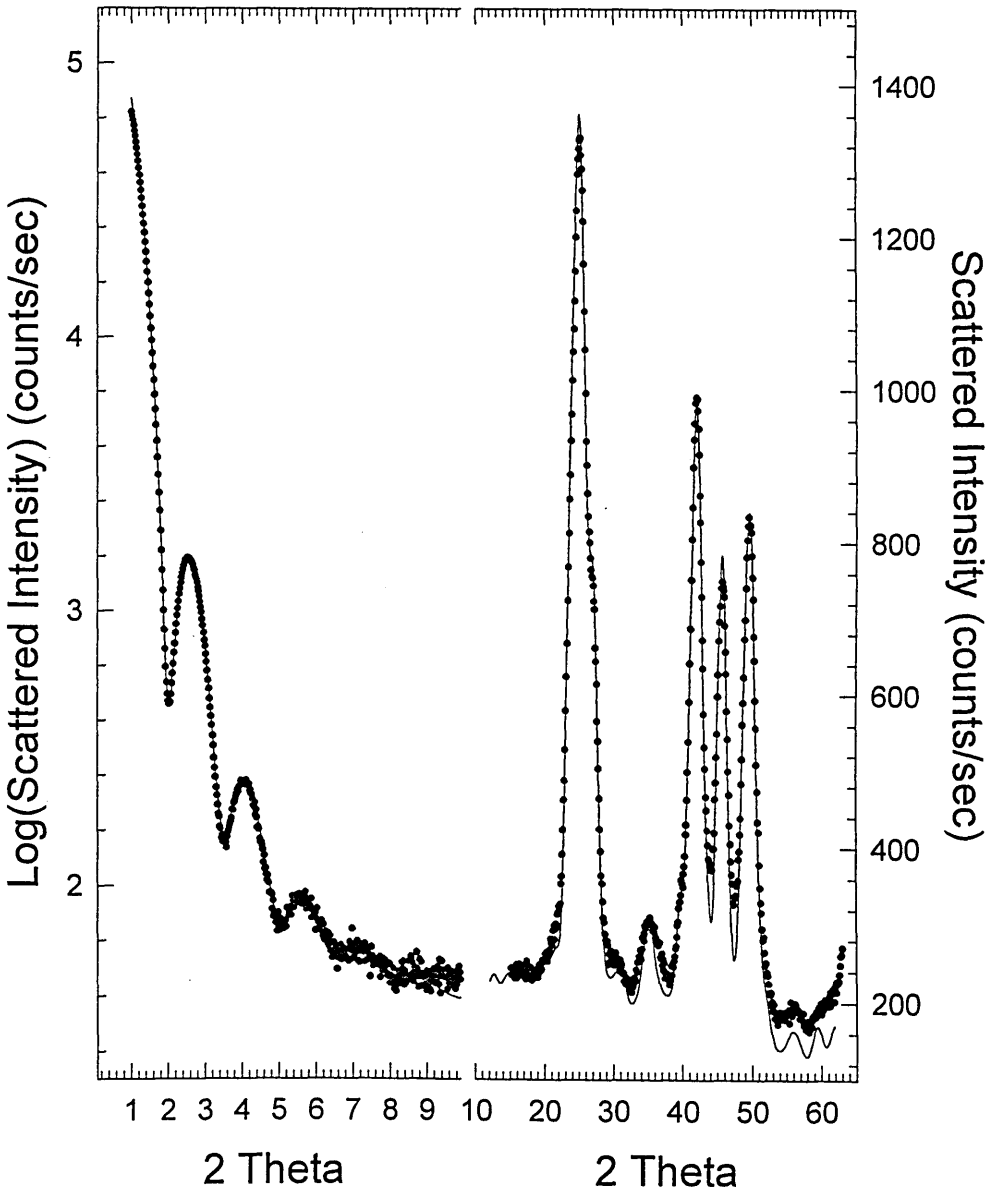

FIG. 4.17 Combined SAXS and WAXS pattern for ~4,500 atom CdSe nanocrystallites. Experimental data is shown as discrete points from separate measurements of the SAXS and WAXS patterns. The solid line is a single calculation for an ensemble of crystallites centered around 4,500 atoms with $\sigma = 4.2\%$. Each crystallite is prolate with an aspect ratio of 1.2 and has a relaxed surface layer.

Simultaneous fitting of SAXS and WAXS patterns with the addition of a single additional parameter [size distribution (σ)] allows the determination of size and shape of nanocrystallites with much greater precision than was previously possible. All values of bond lengths and thermal (Debye-Waller) parameters are consistent with studies of these nanocrystallites earlier in the chapter. The values of σ were allowed to float in this calculation, but fall within the statistical analysis of TEM images ($3.5<\sigma<4.5$).

SAXS is a standard technique for structural analysis in colloid science and has reached a high state of development in studies of monodisperse silica and polymer lattices. Uniformity of our CdSe samples reveals a SAXS fine structure long observed in classic colloidal systems but which has been cloaked by polydispersity in previous studies of quantum dots.[14] A general formulation of SAXS scattering from a collection of non interacting particles is given in equation 4.8. Particles are of rigorously uniform electron density in a homogeneous medium.[15]

$$I(q) = I_o N(\rho - \rho_o)^2 F^2(q) \tag{4.8}$$

Where ρ and ρ_o are the electron density of the particle and the dispersing medium, respectively. I_o is the incident intensity and N is the number of particles. F(q) is the material form factor (the fourier transform of the shape of the scattering object) and is the origin of the oscillations observed. Thus for a spherical particle of radius R

$$F(q) = \frac{4}{3}\pi R^3 [3\frac{\sin(qR) - qR\cos(qR)}{(qR)^3}] \tag{4.9}$$

$$I(q) = I_o N[(\rho - \rho_o)^2 \frac{4}{3}\pi R^3 [3\frac{\sin(qR) - qR\cos(qR)}{(qR)^3}]]^2 \tag{4.10}$$

Figure 4.18A curve (a) shows the calculated pattern for a collection of monodisperse spheres 62Å in diameter of rigorously uniform electron density.

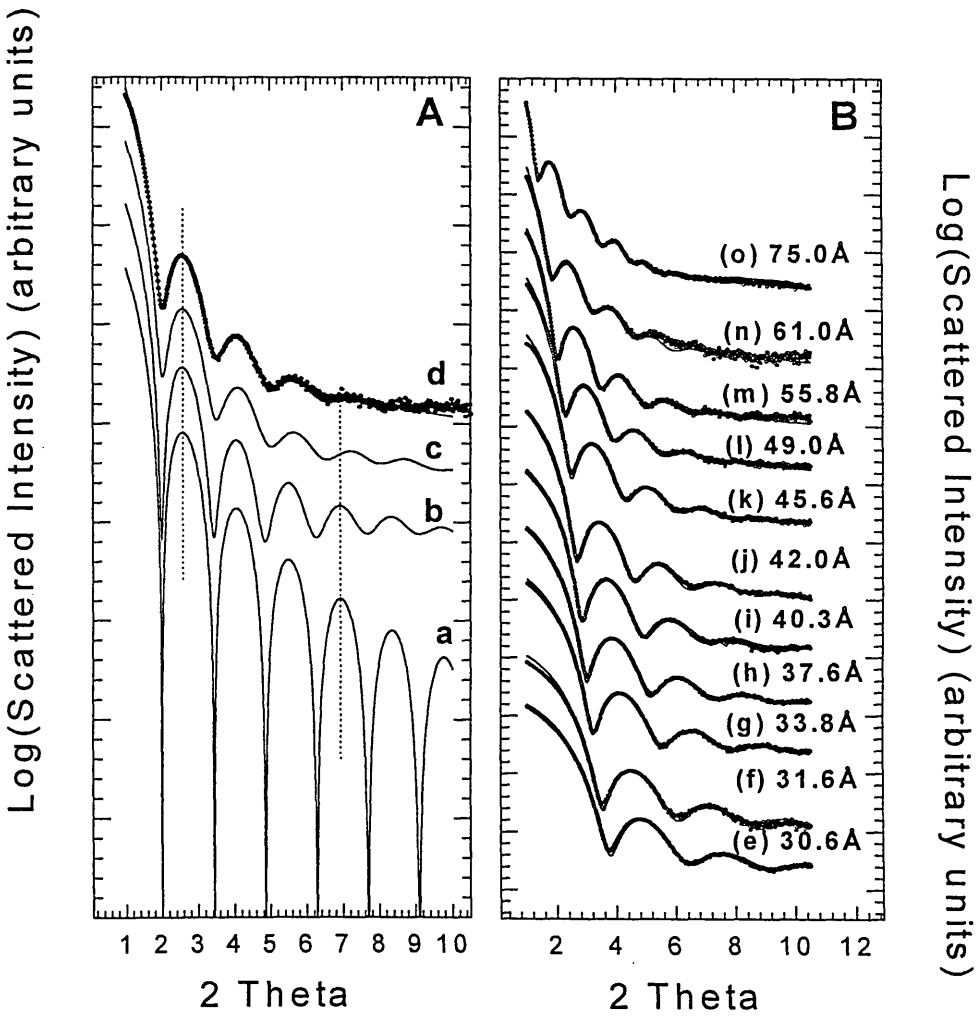

FIG. 4.18A SAXS Patterns for 4500 atom CdSe nanocrystallites and model structures. Curve (a) 62Å spheres of unifom electron density, (b) Monodisperse fragnents of the bulk lattice approximating a sphere of 62Å (~4,500 atoms), (c)monodisperse fragments of the bulk lattice approximating an ellipsoid with a 1.2 aspect ratio (~4,500 atoms), (d) Experimental data and fit from fig. 4.17.

FIG. 4.18B SAXS paterns for a series of CdSe nanocrystallite samples ranging form ~30Å up to 75Å shown as discrete points, solid lines are the fits to models all employing between 3.5 and 4.5% size distibutions. Sizes noted are equivelent diameters. Aspect ratios for the fits are (e) 1.00, (f) 1.00, (g) 1.05, (h) 1.075, (i) 1.10, (j) 1.125, (k) 1.15, (l) 1.175, (m) 1.20, (n) 1.225, (o) 1.250. Size distributions σ (e) 4.3%, (f) 4.0%, (g) 3.8%, (h) 3.7%, (i) 4.0%, (j) 3.8%, (k) 4.0%, (l) 3.6%, (m) 3.7%, (n) 4.2%, (o) 4.3%

Real objects are not of uniform electron density, each atom in the structure provides a local modulation that introduces a broad scattering background. Curve (b) in figure 4.18A shows the scattering pattern for a 4,500 atom fragment of the bulk wurtzite CdSe lattice approximating a sphere. The base line that results is the contribution of diffuse scattering from the individual atoms (analogous to electron Z scattering). The intensity of this contribution scales like the volume ($\sim R^3$) while the intensity of the oscillations scales like the square of the volume ($\sim R^6$). In large particles, micron sized latex and silica, the contribution from atomic scattering becomes negligible. Neglecting this contribution in our small systems however would result in an over estimation of the size distribution. Curve (c) shows the calculated pattern for a prolate (aspect ratio 1.2) fragment of the bulk lattice of CdSe containing 4500 atoms. The period of the oscillations changes and the minima wash out in response the changing shape. The X-ray scattering averages over all orientations of the sample. As with the measurement of particle size in TEM the distribution of projections could be confused with a true size distribution. Curve (d) (dots) shows the experimental results and fit discussed. SAXS oscillations result from the form factors of the individual particles and thus from both the size and shape of the particles. Thus even small variations in size and shape quickly wash out the oscillations. The amplitude of the oscillations allows precise determination of the size distribution.

Figure 4.18B shows the experimental SAXS patterns for 9 CdSe nanocrystallite samples isolated from a single preparation and processed by size selective precipitation. Experimental data is presented as discrete points and the corresponding computer simulations provide the solid lines. Particles above 25Å in diameter become increasingly prolate as growth by Ostwald ripening proceeds.

Scattering from samples smaller than 20Å was also collected. These sample display deviations from spherical symmetry. The form factors appears more consistent with cubes or angular structures and may indicate the transition to tetrahedral structures discussed earlier.

4.6 Conclusion

A series of independent structural studies have been combined with simple computer models to produce a self-consistent description of semiconductor nanocrystallites. The samples are shown to be monodisperse to the limit of atomic roughness. The presence of stacking faults, crystallite shapes, and surface relaxations are important in fitting the experimental data.

We find that the structural properties of these nanocrystallites approach the bulk limit much more rapidly than the optical properties. Structural evolution is dominated by local bonding. As soon as a reference atom is surrounded by a uniform second nearest neighbor shell, its nearest neighbor bond lengths are equal to the bulk (within experimental uncertainty). We find that these directionally bonded systems show little evidence for the isotropic lattice contractions found in metallic or ionic systems. Rather we believe the surface free energy to be minimized in the local relaxation of the surface atoms. We suggest surface atoms, lacking complete tetrahedral coordination, undergo relaxation (rehybridization) to lower the energy of the interface. The result is a surface monolayer of CdSe displaying a distribution of bond lengths and bond angles.

With a sound description of the inorganic core we focus now on the investigation of the organic capping shell.

4.7 Bibliography and References

(1) Ph. Buffat and J. P. Borel, Phys. Rev. A. 13. 2287 (1976).

(2) R. S. Berry, H. Chen, and J. Rose, High Temperature Science Vol. 27 (Humana Press Inc. 1990) p. 61.

(3) M. Danek, K. F. Jense, C. B. Murray, and M. G. Bawendi (submitted).

(4) N. Herron, J. C. Calabrese, W. E. Farneth, and Y. Wang Science 259,1426 (1993).

(5) B. O. Daboussi, C. B. Murray, M.F. Rubner, and M.G. Bawendi, Chem. Mater. 6, 217 (1994).

(6) M. A. Marcus, L. E. Brus, C. B. Murray, M. G. Bawendi, A. Prasad,and A. P. Alivisatos, NanoSTRUCTURED MATERIALS 1, 323 (1992).

(7) K. T. Boon,EXAFS: Basic Principles and Data Analysis (Springer-Verlag New York 1986) chapter 1-3.

(8) M. G. Bawendi, R. Kortan, M. L. Steigerwald, and L. E. Brus, J. Chem. Phys. 91, 7282 (1989).

(9) B. D. Hall and R. Monot, Comput. Phys. 5, 414, (1991).

(10) J. F. Vetelino and S. P. Mitra, Phys. Rev. B. 5, 2360 (1972).

(11) (a) Y. Wang and N. Herron, Phys. Rev. B 42, 7253 (1990) (b) A. N. Goldstein, C. M. Echer, and A. P. Alivisatos, Science, 256, 1425 (1992). (c) V. L. Colvin, A. N. Goldstein, and A. P. Alivisatos, J. Am. Chem. Soc. 114, 5221 (1992).

(12) (a) C. B. Duke, A. Patton, Y. R. Wang, K. Stiles, and A Kahn Surface Sci. 197, 11 (1988), (b) Y. R. Wang and C. B. Duke, Phys. Rev. B, 37, 6417 (1988) (c) T. N. Horsky, G. R. Brandes, K. F. Canter, C. B. Duke, A. Paton, D. L. Lessor, A. Kahn, S. F. Horng, K. Stevens, K. Stiles, and A. P. Mills, Jr., Phys. Rev. B 46, 7011(1992).

(13) J. E. Bowen Katari, V. L. Colvin, and A. P. Alivisatos, J. Phys. Chem. 98, 4109 (1994).

(14) O. Glatter and O Kratky, Small Angle Scattering (Academic Press 1982).

(15) A. Guinier and G. Fournet, Small Angle Scattering of X-rays (John Wiley and Sons 1955) chapters 1-3.

Chapter 5

Characterization and Manipulation of the Organic Capping Shell

(Much of this chapter has appeared in print: L. R. Becerra *et al,* J. Chem. Phys. 100 (4), 3297 (1994))

5.0 Introduction:

Optical studies indicate that surface morphology may play an important role in the electronic relaxation processes.[1-3] This is not surprising since 10's of percents of the atoms in a nanometer size crystallite do not have their full coordination and can be characterized as surface atoms. Surface derivatization (capping) of these small fragments of the bulk lattice is essential to prevent aggregation in solution and during growth.[4-5] The cap species are also thought to electronically passivate possible surface trap states.[2,3] While EXAFS, X-ray scattering and electron microscopy have been used to establish the structure of the semiconductor core, the structure of the surface has remained largely elusive. Nuclear magnetic resonance (NMR), by virtue of probing local chemical environments, has the capability of providing important information on crystallite surfaces.[7,8] For example, NMR has been used to explore the surface morphology of CdS nanocrystallites capped with thiophenol.[8]

We present a room temperature ^{31}P NMR study of the tri-n-octylphosphine chalcogenide moieties capping the surface of CdSe nanocrystallites synthesized using the method desribed in chapter 2. The identity and relative intensity of the two lines in the ^{31}P NMR spectrum of ~37 Å diameter CdSe crystallites is determined. An estimate for the percentage of surface atoms coordinated by a capping species is obtained. These results are combined to develop a model for the morphology of the surface of the nanocrystallites.

5.1 Experimental

Powders of three types of capped CdSe nanocrystallites were used to explore surface morphology. All samples were produced from the pyrolysis of dimethylcadmium

and tri-n-octylphosphine selenide in a solution of 50% tri-n-octylphosphine (TOP) and 50 % tri-n-octylphosphine oxide (TOPO).

Sample 1 contained ~1 g CdSe crystallites with an average diameter of ~ 37Å (±10%). Crystallite surfaces were passivated with a combination of tri-n-octylphosphine chalcogenide species. Sample 2 was synthesized as above followed by size selective precipitation to yield ~ 20 mg of nearly monodisperse ~ 37 Å diameter CdSe crystallites. This sample was chemically identical to sample 1 but displayed < 5% standard deviation in diameter. Sample 3 was prepared with a 4:1 excess of TOPO over TOP and washed twice with a 20% solution of TOPO in warm BuOH (60 °C) to remove TOPSe species prior to isolation by standard procedures.[5] Removal of the TOPSe groups produced a small shift in the optical absorbance indicating a slight decrease in average crystallite size. Multiple samples of types 1, 2, and 3 were used to insure reproducibility of the data.

Due to the large chemical shift anisotropies exhibited by ^{31}P, MAS was coupled with proton-cross-polarization and decoupling to obtain high resolution spectra. Experiments were performed at room temperature on two home-made spectrometers operating at 128.5 and 161.0 MHz for the ^{31}P resonance (317 and 400 MHz for ^{1}H) and 60.6 MHz for the ^{77}Se resonance (317 MHz for ^{1}H). Samples were spun at ~ 3.7 kHz in 7 mm rotors from Doty Scientific. Chemical shifts (positive for higher frequencies) are reported in ppm relative to 85% H_3PO_4.

5.2 Results and Discussion

The MAS ^{31}P spectra of free TOPO and of sample 1 are shown in Figure 5.1. Comparison of the isotropic shifts (lines marked with an asterisk in both spectra) indicates a smaller chemical shift (greater shielding) of the ^{31}P upon attachment to the surface. It is important to note that sample spinning and ^{1}H decoupling do not narrow the lines in the nanocrystallite samples nearly as effectively as in free TOPO. Further, the fact that the linewidths scale with the external field suggests that the broadening is inhomogeneous rather than homogeneous in origin and therefore probably arises from a distribution of chemical shifts. Chemical shifts may vary due to changes in electron

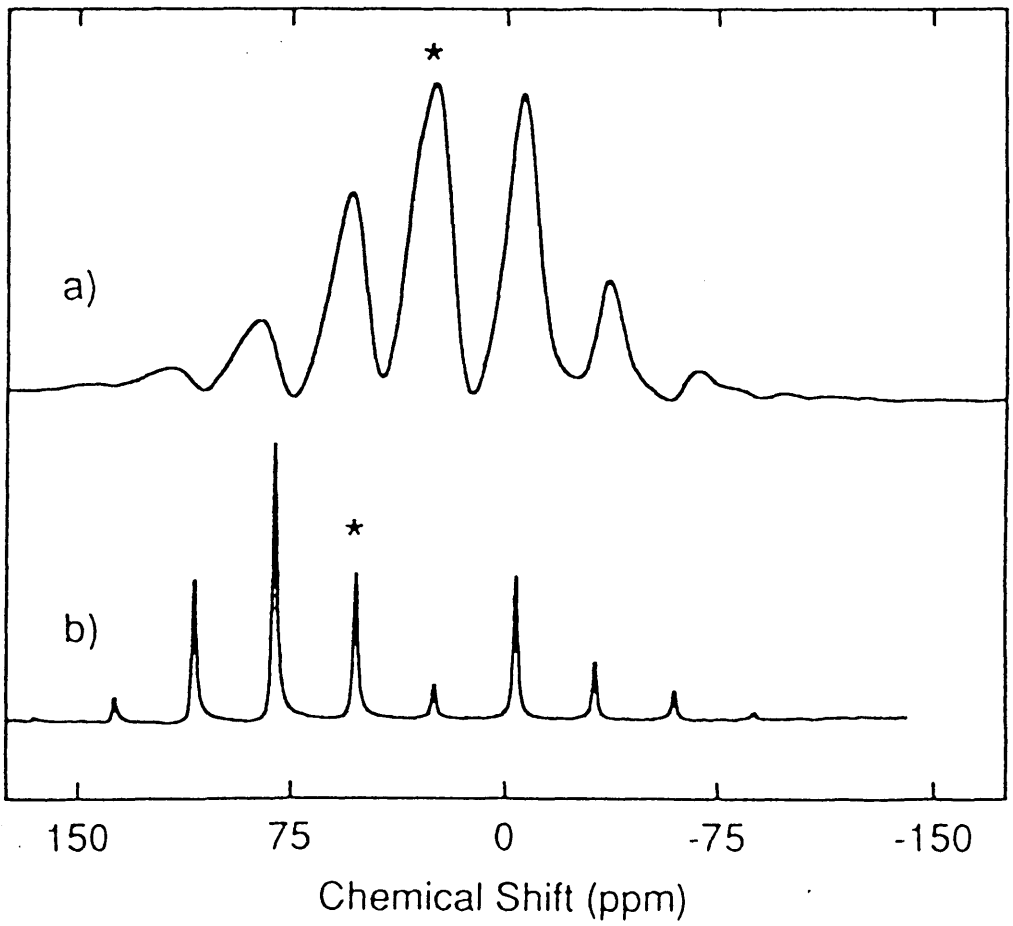

FIG. 5.1 ^{31}P MAS/NMR spectra of (a) CdSe nanocrystallite sample 1 and (b) free TOPO. The asterisk denotes the isotropic line. Chemical shifts (positive for higher frequencies) are reported with respect to 85% H_3PO_4.

overlap or in bond angle[9] and these factors together with the large size of ^{31}P shift tensors makes phosphorous spectra sensitive to disorder. In addition, structural studies of these CdSe nanocrystallites with a variety of techniques indicate the presence of a disordered surface and thus support a distribution of phosphorous coordination environments.[5,10] Therefore, we believe the resulting distribution of chemical shifts (which is unaffected by MAS) is the origin of the broadening.

Since the electronic structure of the crystallite changes with size, it is important to investigate if the effect of distributions of crystallite sizes contributes to the linewidth. The spectrum of sample 2, with a much narrower size distribution than in sample 1, showed no change in the widths or other features of the spectrum. Spectra of free TOPO and of sample 1 show different chemical shift anisotropies (Figure 5.1). Using rotational sideband intensities and spectra obtained at three different spinning speeds, the (traceless) chemical shift tensor parameters can be determined.[11] Free TOPO gives σ_{11}=62.3, σ_{22}=62.2, and σ_{33}=-124.5 ppm. This is an axially symmetric chemical shift tensor which indicates a threefold or higher symmetry for free TOPO. Sample 1, however, gives σ_{11}=76.6, σ_{22}=5.7, and σ_{33}=-82.2 ppm, giving an asymmetry parameter of η=-0.86. Solution coordination chemistry indicates that phosphine chalconide ligands have the potential for unidentate (bent) or bridging coordination.[12a] Both bent and bridging coordinations to the surface may result in a loss of axial symmetry at the phosporous site.

The spectrum of CdSe crystallites (sample 1) consists of two superimposed lines, each in turn broader than that of free TOPO. A least squares fit of the isotropic peak with two Gaussians (Figure 5.2) gives relative intensities of 31% and 69% with chemical shifts of 22.2 and 29.3 ppm respectively. The chemical shift of free TOPO relative to that of TOPSe was measured to be +7.4 ppm, in good agreement with the relative shift of the two surface species (7.1 ppm). The major component (29.3 ppm) is then assigned to surface TOPO and the minor component (22.2 ppm) is assigned to surface TOPSe moieties.

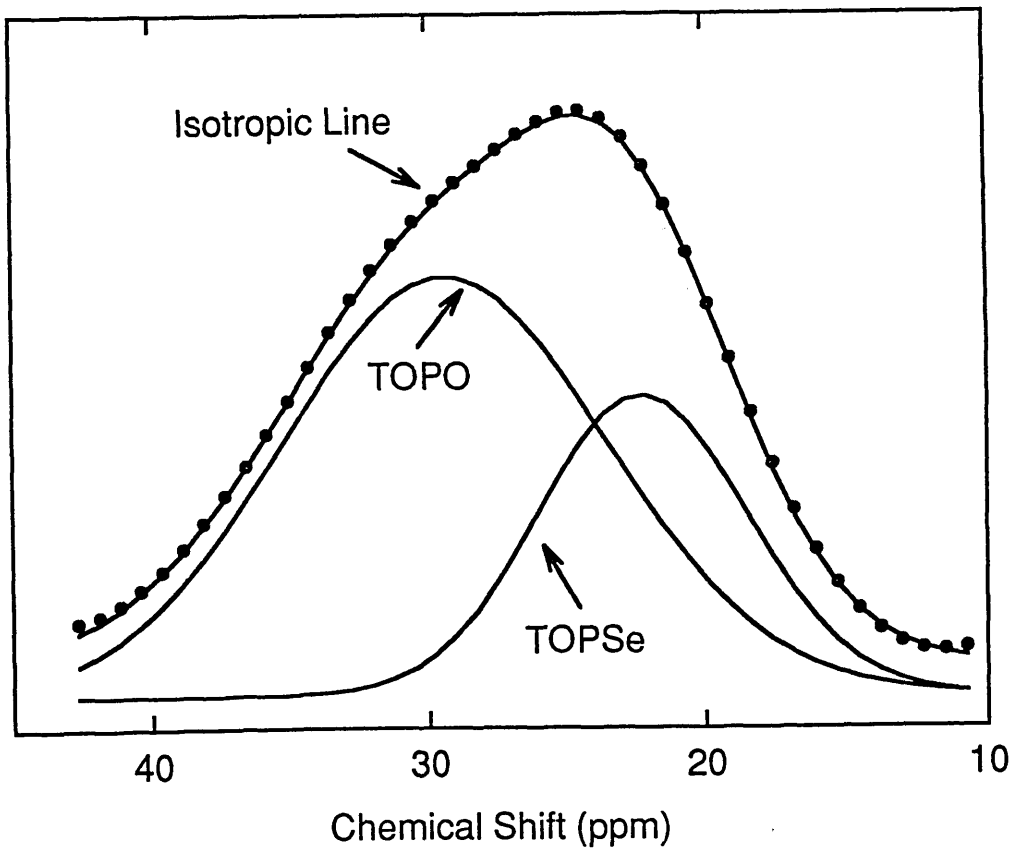

FIG. 5.2 Experimental (dots) and simulated (solid lines) data for the isotropic line of CdSe sample 1. The fit uses two Gaussian line shapes as described in the text.

The relative amounts of surface TOPO and TOPSe species are somewhat sample dependent and can be deliberately varied by changing growth conditions and isolation procedures. We exploit this control of surface composition to isolate the spectrum of a single capping species using sample 3. Figure 5.3 shows the MAS spectrum of sample 3 which has been treated to exclusively preserve the TOPO surface passivation. The chemical shift of 30.9 ppm agrees with the component of sample 1 initially assigned to TOPO. Attempts to prepare and isolate CdSe samples capped exclusively by the TOPSe moiety were unsuccessful. The much weaker TOPSe bonding to cadmium[12b] probably did not allow for the stabilization of the crystallites while the extraneous phosphine species were being removed.

The TOPSe species can be identified by a double resonance experiment between ^{77}Se and ^{31}P. In rotational echo double resonance (REDOR),[13] the ^{31}P spin echoes are detected with and without applying rf pulses to the ^{77}Se nuclei. The ^{31}P echoes are attenuated in the presence of ^{77}Se pulses and the difference of the two echoes (with and without ^{77}Se pulses) is Fourier transformed to provide the signal corresponding to the ^{31}P nuclei in close proximity to the ^{77}Se atoms. The spectrum of sample 1 and the REDOR difference spectrum are shown in Figure 5.4. Since ^{77}Se is 7% abundant, only a small fraction of the ^{31}P nuclei close to Se can be detected with REDOR. The REDOR difference shows a central peak at 23 ppm with a relative intensity of about 5% which confirms the assignment of the minor surface component (22.2 ppm) as surface bound TOPSe moieties.

The 25 ppm increased shielding of the capping TOPO and TOPSe molecules relative to the free species may be due to the weakening of the P=O and P=Se bonds upon coordinating to the surface. Extensive infrared studies show a decrease in the P=O stretch frequency upon coordination to Zn and Cd halides, consistent with a weakening of the P=O bond.[14]

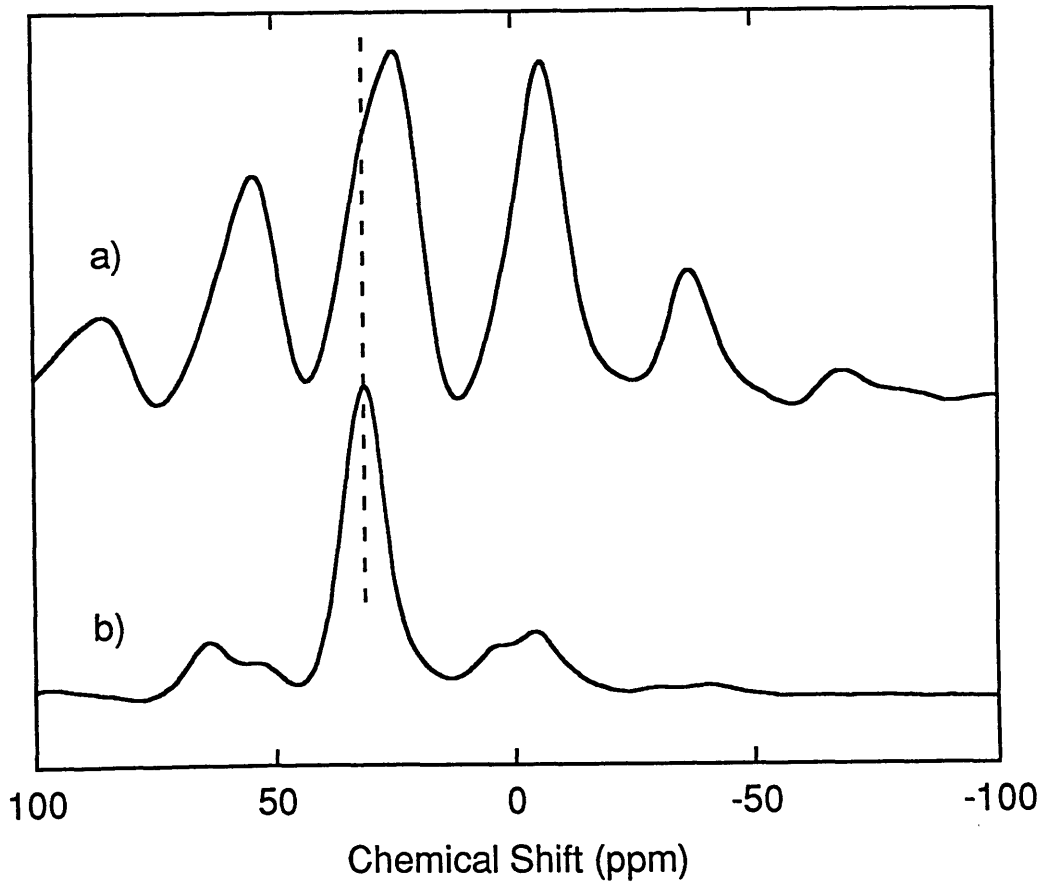

FIG. 5.3 ^{31}P MAS/NMR spectra of (a) sample 1 and (b) sample 3. Sample 3 was treated to remove TOPSe molecules from the surface leaving TOPO as the only capping molecule. The dotted vertical line indicates the isotropic shift for the TOPO component in each sample.

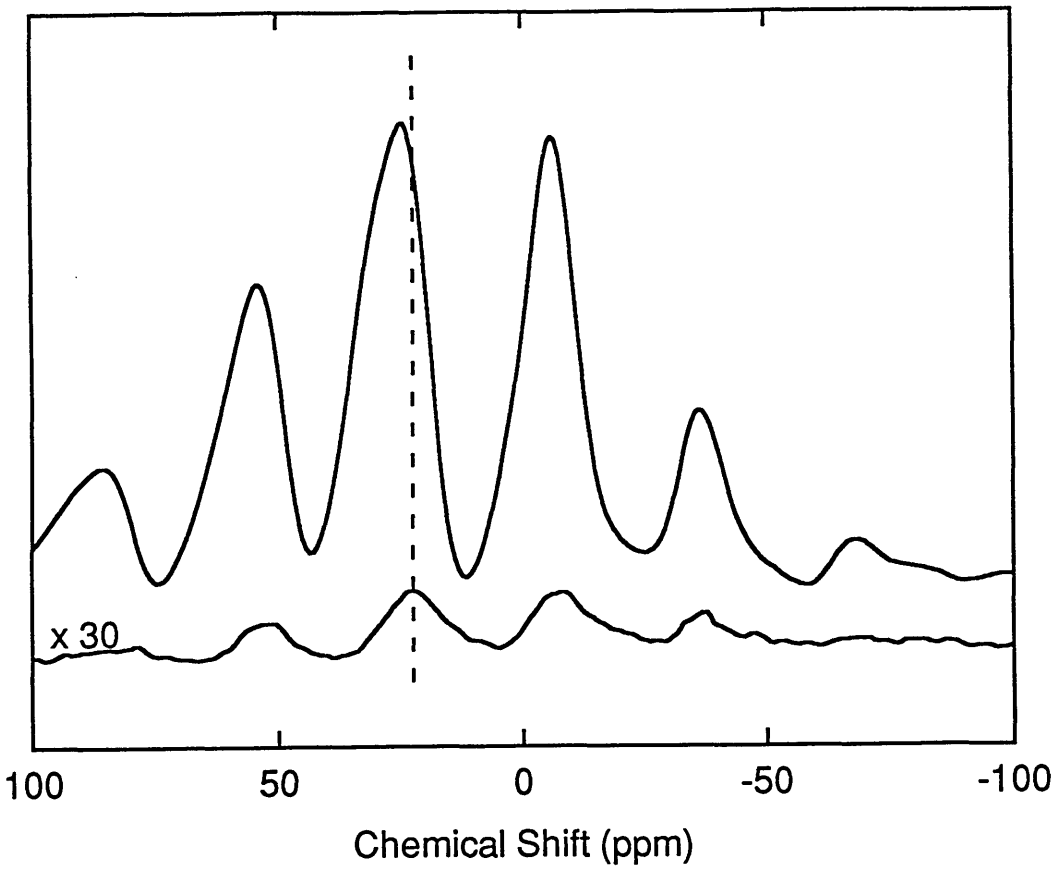

FIG. 5.4 ^{31}P MAS/NMR spectra of sample 1. (a) Full spectrum and (b) REDOR difference (x30) gives the ^{31}P species attached to Se. The dotted vertical line indicates the isotropic shift for the difference and the component assigned to TOPSe.

With the chemical identity of surface species clearly established it is possible to address quantitatively the important issue of surface coverage. GaP was added to the sample to provide an internal standard with a ^{31}P resonance conveniently shifted from that of the nanocrystallites and with which the amount of ^{31}P in the sample can be quantitatively established. Models of average CdSe nanocrystallite core morphology have been developed through extensive structural studies.[5,6] An average crystallite in sample 1 is modeled as slightly prolate (aspect ratio of 1.1) with a major axis of 37 Å. Crystallites are assumed stoichiometric with ~ 700 core atoms having complete tetrahedral coordination. An additional ~ 300 surface atoms (with coordination numbers of two or three) present an equal distribution of Cd and Se surface sites. By carefully weighing the amounts of CdSe nanocrystallite powder and GaP used and with this model we find approximately 150 to 170 phosphine chalconide capping groups per crystallite (~55% coverage of the surface atoms). Because of their basic character, both TOPO and TOPSe are expected to bind preferentially, if not exclusively, to Cd sites. This implies that nearly all surface Cd atoms are chemically passivated. We consider the TOPSe moieties structurally as capping groups because coordination by phosphine chalconide ligands is restricted to be at most bidentate.[12] The blue shift of the optical spectrum following exchange of TOPSe with TOPO molecules however indicates that the Se atoms in the capping TOPSe molecules participate in the electronic structure of the CdSe nanocrystallites. Changing the stoichiometry in the modeling so that the crystallites are stoichiometric if the Se atoms from the TOPSe groups are included does not change the surface coverage by more than a few percent and our conclusions remain unaffected. Although the density of capping groups on particular crystallographic surfaces probably fluctuates with the availability of coordination sites, the resulting gross morphology is a nearly hydrophobic shell surrounding each crystallite. The coverage is sufficient to coordinate all the surface Cd sites in our structural models, but does not permit passivation of all surface Se sites. This surface passivation is critical to both the optical and physical properties of the crystallites. A reduction of the total capping fraction below 50% by chemical treatments (e.g. extensive washings) results in a significant decrease in

the luminescence quantum yield and over time produces irreversible flocculation of the colloids.

Spin echo experiments on ^{31}P indicate an average P-P distance of ~8-10 Å consistent with capping of alternate atomic sites on the surface. The weak homonuclear coupling also supports the conclusion that the linewidths are largely inhomogeneous in nature. Measurements of closest approach for neighboring molecules in monolayers of TOPO[15] indicate that the 8-10 Å spacing places the capping groups in the close packed limit. This conclusion is in contrast to the islanding and low coverage found in previous works.[8] Transmission electron microscopy images of close packed monolayers (using LB technology) of CdSe nanocrystallites capped with TOPO and TOPSe are also consistent with a uniform hydrophobic shell.[16] Dispersions of CdSe nanocrystallites capped with TOPO and TOPSe in alkanes are stable on time scales of months if not years. A close packed hydrophobic capping shell around each crystallite is then also consistent with the stability of these colloidal suspensions.

Katari *et al* have employed X-ray photoelectron spectroscopy as a prode of the phosphine chalcogenide capped nanocrystallites prepared by an analogous procedure.[17] The results of these studies agree closely with those detailed here. The studies demonstrate the importance of surface passivation in preventing oxidation of the crystallite surface. Pyridine capped nanocrystallites were shown to be particularly susceptible to surface oxidation. We find that warming the oxidized crystallites with an excess trioctylphoshine can reduce the surface of the particles largely recovering their initial optical features. A slight blue shift in the absorption and luminescence is consistent with a decrease in average particle size. The decrease in particle size was confimed by SAXS.

This ^{31}P MAS/NMR study provides both qualitative and quantitative chemical analysis of the capping layer on CdSe nanocrystallites. A model for the morphology of the surface of crystallites is then developed. The average crystallite surface is capped with ~ 70% TOPO molecules and ~ 30% TOPSe molecules which combine to produce a close packed hydrophobic shell passivating surface Cd sites. The inhomogeneous linewidth of the NMR transitions indicates a variety of coordination environments for

both TOPO and TOPSe surface species. The morphology of the surface deduced from these experiments correlates with results of optical studies and with the stability of dispersions of these nanocrystallites in alkanes. Further refinement of the surface structure will be essential to understanding and ultimately controlling the properties of these spatially confined systems.

In summary, we model our CdSe nanocrystallites as fragments of the bulk wurtzite lattice surrounded by a relaxed surface layer of CdSe capped with a close-packed monolayer of trialkylphoshine chalcogenide groups.

5.3 Surface Exchange

The surface capping layer is essential in mediating the growth process and in stabilizing the crystallites in a variety of dispersing media. The assembly of the monolayer of capping groups is driven by the coordination of surface Cd sites. The capping groups maintain a dynamic equilibrium with the solution. Simple ligand exchange techniques allow us to exercise tremendous control over the capping shell by tailoring independently the tail and head groups of the ambiphilic capping groups. Tailoring the tail groups allows us to optimize the stability of the particles in a variety of solvents and polymer matrices. The head groups bind directly to the semiconductor surface passivating surface electronic states. The energetics of surface coordination may also influence the mode and magnitude of the surface relaxation.

Crystallite surface derivatization can be modified by repeated exposure to an excess of a competing capping group. Heating to ~ 60 °C a mixture of ~50 mg TOPO/TOP capped crystallites and 5-10 ml pyridine gradually disperses the crystallites in the solvent. Treatment of the dispersion with excess hexane results in the flocculation of the crystallites which are then isolated by centrifugation. The process of dispersion in pyridine and flocculation with hexane is repeated a number of times to produce crystallites which disperse readily in pyridine, methanol, and aromatics, but no longer disperse in aliphatics.

Pyridine capped samples can then be exchanged for alkylphosphine / alkylphoshine oxides of a desired chain length by an analogous process. Using pyridine as an intermediate crystallites can be derivitized with a variety of other Lewis bases (eg amines, phosphites / phosphates, furans) and a number of Lewis acidic capping groups (tributylborane and trioctylaluminum). Handling procedures for these lewis acidic capping groups have been developed by Kuno.[18] Heating of the pyridine capped samples in vacuum quantitatively desorbs the pyridine leaving the semiconductor core unpassivated.

Pyrazine is a molecule which can produce bridging flocculation, and as such it is better described as a flocculant than a capping group. The bridging flocculation is however very temperature sensitive and thus the aggregation of the particles can be controlled.

The utility of cap exchange has been demonstrated in ^{31}P NMR studies. The ability to make selective surface substitutions was a powerful tool in simplifing chemical analysis. Control over the capping groups allows the interaction with solvents and polymer matrices to be tailored.

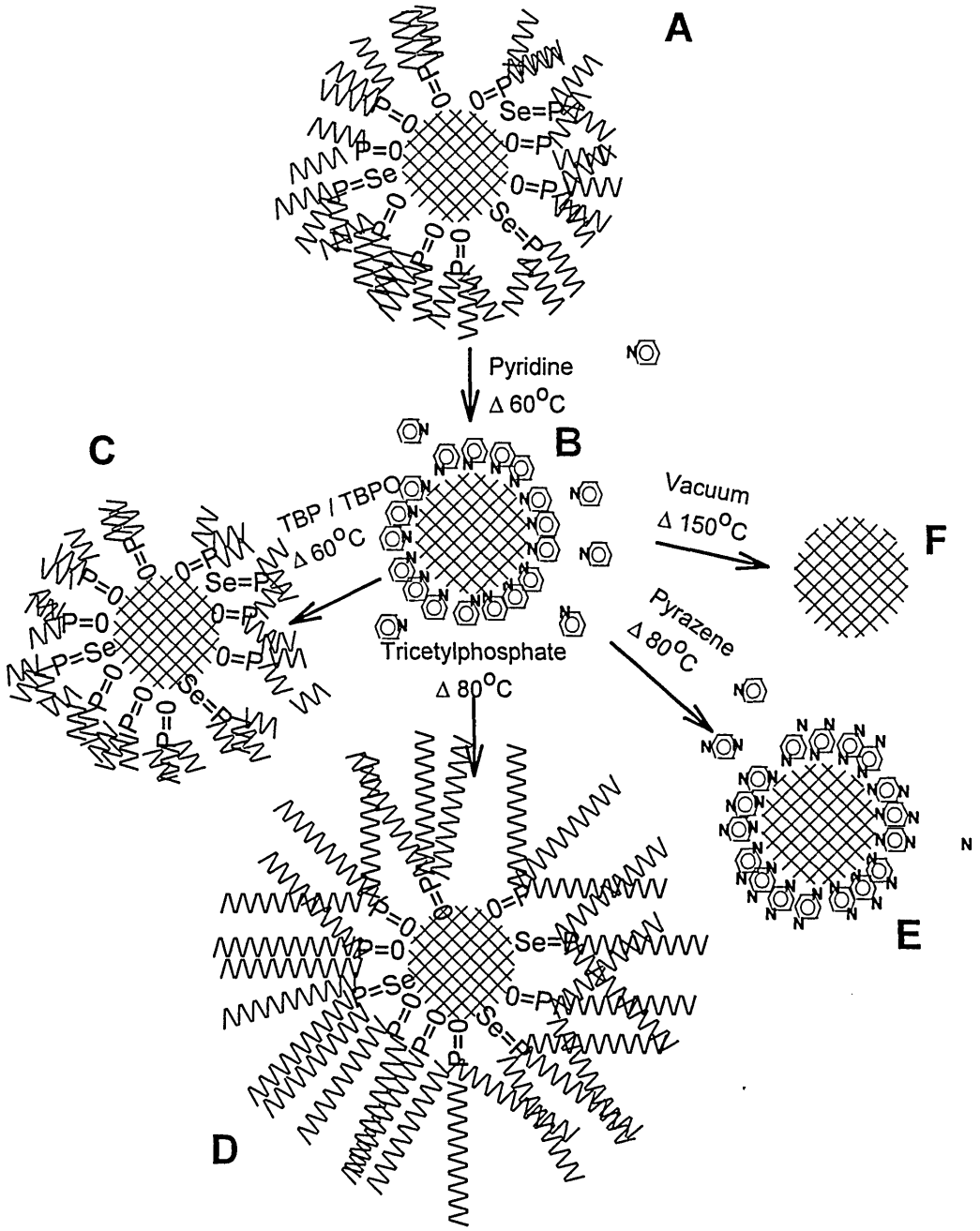

FIG 5.5 Cartoon shows cap exchange of the (A) native TOPO/TOPSe caps exchanged for (B) pyridine. The pyridine capped crystallites can then be exchanged for (C) tributylphoshine oxide TBPO, (D) tricetylphosphate TCPO, (E) pyrazine, or removed completely to yield (F) the bare semiconductor core.

The capping groups play a crucial role in the optical properties of the crystallites by passivating surface sites that can serve as nonradiative centers. The quantum yield of the samples is strongly dependent on the efficiency of the capping groups as seen in figure 5.6A. The quantum yield of samples with an optimal coating of TOPSE/ TOPO on the surface approaches 20% [curve (a)]. When subjected to excessive washing the capping shell is partially stripped (confirmed by ^{31}P NMR). The QY of the particles drops by almost 2 orders of magnitude to ~0.2% seen in [curve (c)]. Addition of a few drops of a 1% TOP/TOPO solution in hexane immediatly returns the QY to ~15% [curve (b)]. X-ray photoemision spectroscopy (XPS) studies of CdSe nanocrystallites have identified the deterioration of the crystallite surface due to oxidation. A sample of crystallites was placed in a flask back filled with 1 atm of O_2 for 3 days. Spectrum (d) shows that the oxidized sample has dramaticly reduced the luminescenced. Luminescence from pyridine capped samples dispersed in toluene is almost undetectible with a QY of less than 0.001%. The electronic passivation of the surface is critically dependent on the character and coverage of the capping groups.

Methods for the facile exchange of surface capping groups allow us to optimize the stability of dipersions and strongly influence the photoemission properties of the nanocrystallites. With control established over the organic capping layer our model structural studies of the individual crystallites are sufficiently refined to begin investigating more complex systems.

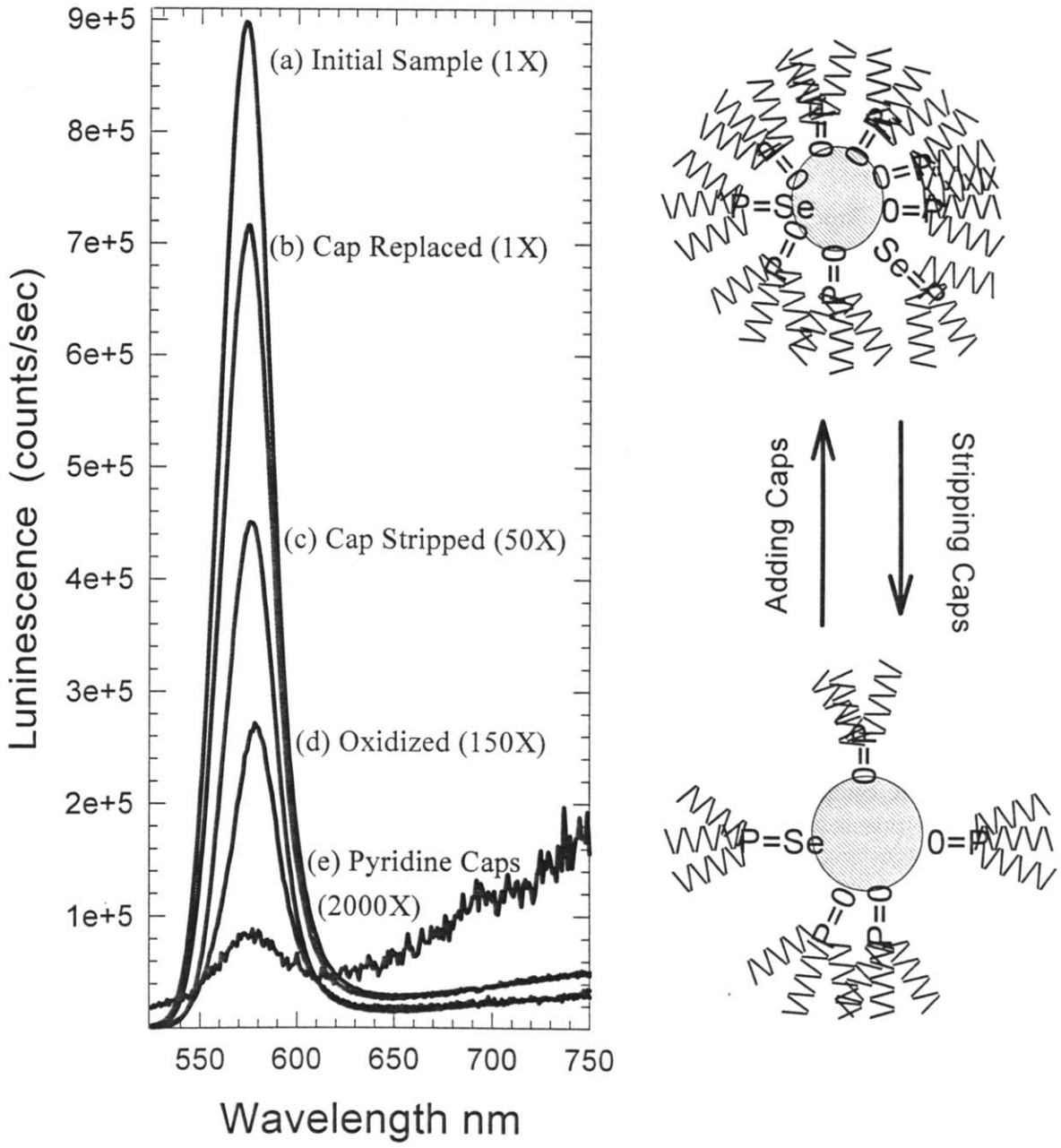

FIG. 5.6 Luminescence specra show the effects of surface manipulation. (a) Shows emission for a native sample. (c) Shows luminescence from a sample with the capping shell partially stripped. (b) Shows the recovery of the emission when TOPO and TOP are added to the solution to reassemble the close packed surface passivation. (d) Sample oxidized. (e) Pyridine capped.

References

(1) H. Weller, Angew. Chem. Int. Ed. Engl. 32, *41* (1993). A. Henglein, Top. Curr. Chem. 143, *113* (1988).

(2) See for example L. E. Brus, J. Phys. Chem. 90, *2555* (1986). M. O'Neil, J. Marohn, and G. McLendon, J. Phys. Chem. 94, *4356* (1990). A. Eychmuller, A. Hasselbath, L. Katsikas, and H. Weller, Ber. Bunsenges. Phys. Chem. 95, *79* (1991).

(3) M. G. Bawendi, P. J. Carrol, W. L. Wilson, and L. E. Brus, J. Chem. Phys. 96, *946* (1991). M. Nirmal, C. B. Murray, D. J. Norris, and M. G. Bawendi, Z. Phys. D26, *361* (1993).

(4) M. L. Steigerwald, A. P. Alivisatos, J. M. Gibson, T. D. Harris, R. Kortan, A. J. Muller, A. M. Thayer, T. M. Duncan, D. C. Douglas, and L. E. Brus, J. Am. Chem. Soc. 110, *3046* (1988).

(5) C. B. Murray, D. J. Norris, and M. G. Bawendi, J. Am. Chem. Soc. 115, *8706* (1993).

(6) M. G. Bawendi, A. R. Kortan, M. L. Steigerwald, and L. E. Brus, J. Chem. Phys. 91, *2782* (1989).

(7) A. M. Thayer, M. L. Steigerwald, T. M. Duncan, and D. C. Douglass, Phys. Rev. Lett. 60, *2673* (1988).

(8) J. R. Sachleben, E. Wrenn-Wooten, L. Emsley, A. Pines, V. L. Colvin, and A. P. Alivisatos, Chem. Phys. Lett. 198, *431* (1992).

(9) D. G. Gorenstien, Prog. in NMR Spec. 16, *1* (1983).

(10) M. A. Marcus, L. E. Brus, C. B. Murray, M. G. Bawendi, A. Prasad, and A. P. Alivisatos, Nanostruct. Mater. 1, *323* (1992).

(11) J. Herzfeld and A. E. Berger, J. Chem. Phys. 73, *6021* (1980).

(12) (a) F. R. Hartley, The Chemistry of Organophosphorous Compounds 2, (John Wiley and Sons, New York, 1992) page 414; (b) ibid, page 487.

(13) T. Gullion and J. Schaefer, Adv. Magn. Res. 13, *55* (1989).

(14) F. A. Cotton, R. D. Barnes, E. Bannister, J. Chem. Soc. *2179* (1960); G. B. Deacon and J. H. S. Green, Spectrochimica Acta 24a, *845* (1968).

(15) J. Dittrich, R. Philipp, H. D. Dorfler, and E. Muller, Electrochimica Acta 32, *479* (1987); A. Pappa-Louisi, P. Nikita, and D. Jannakoudakis, Electrochimica Acta 29, *515* (1984).

(16) B. O. Daboussi, C. B. Murray, M. F. Rubner, and M. G. Bawendi, Chem. Mater. 6, 216 (1994)

(17) J. E. Bowen Katari, V. L. Colvin, and A. P. Alivisatos, J. Phys. Chem. 98, 4109 (1994)

(18) M. K. Kuno (unpublished)

Chapter 6

Self-Organization of Close Packed Quantum Dot Solids

6.1 Introduction

Control over the size, shape and structure of the inorganic core as well as the chemical nature and dimensions of the organic capping layer has been established. Simple modifications of the synthetic procedures allow us to precisely and independently vary these structural parameters. With methods to control the individual nanocrystallite structure well developed, we can now turn our attention to the rational assembly of these tailored building blocks into extended close packed quantum dot solids.

New cooperative phenomena resulting from the coupling of quantum dot electronic states have been predicted when quantum dots (QDs) are organized into 3D close packed solids.[1-3] Two dimensional arrays of significantly larger QDs have been fabricated lithographically and show that novel electronic behavior arises from inter dot interactions.[4] Pioneering work on nanocrystalline TiO_2 semiconductor electrodes,[5] ZnO membranes,[6] and CdS nanocrystalline thin films[7] show new optical and electronic phenomena and highlight the need for more refined structural models.

Study of an appropriately high quality model system is critical to understanding any new collective phenomena. Extremely strict tolerances must be met both in the preparation and characterization of the individual QDs as well as their assembly into solid superstructures. Monodispersity, the classic synthetic goal of colloid chemistry, must be achieved; the average crystallite size must be continuously tunable over a wide range and the distribution about the average must be made arbitrarily small. Many methods have been employed by researchers seeking to organize QDs into solid state structures including incorporation into zeolites[8] and Langmuir Bloggett films,[9] etc. Use of the QDs as the fundamental building block in new close packed solids is a simple concept. Small CdS clusters containing fewer than 100 atoms are truly monodisperse and have been isolated as true molecular crystals.[10] This important work provides encouragement that much larger quantum dots containing thousands to tens of thousands of atoms can be organized in solution. Ordering of amorphous iron oxide particles observed by Bentzon

et al is the most powerful demonstration that colloidal organization of nanometer sized particles is possible.[11, 12]

Organization of much larger colloidal particles (0.1 to 1 micron) into well defined structures, such as colloidal glasses and colloidal crystals is an active area of interest.[13] Opals are natural examples of colloidal crystals in which monodisperse silica particles have grown and organized under hydrothermal conditions.[14] Their prized iridescence results from the Bragg diffraction of light by the regular lattice of colloidal particles. The phenomenology of synthetic colloidal crystals is now well developed. A series of particularly extensive studies of ordering in monodisperse latex provides a sound framework for the structural characterization of the QD glasses and QD colloidal crystals presented here.[15,16] Unlike silica or latex particles our particles, (QDs) have an internal crystalline lattice and possess highly delocalized electronic states.

We synthesize and characterize the monodisperse nanocrystallites and then rationally assemble them into novel solids incorporating the desirable photo/physical properties of mesoscopic structures. Combining a simple synthesis of monodisperse CdSe QDs with established methods for organizing colloidal particles provides a versatile route to novel QD solids. Systematic variations of size, spacing, and orientation of the individual CdSe QDs is achieved while controlling the symmetry and orientation of the solid superstructure. Control of dots with sizes from ~15Å to greater than 100Å smoothly tunes the absorption onset of the solids from ~400 nm to 700 nm. Interdot spacing can be varied from intimate contact of the dots up to ~17Å. Glassy QD solids with only short range order and random orientations of the individual crystallites provide isotropic optical materials. 3D QD superlattices coherent over hundreds of microns with highly oriented arrays of quantum dots provide highly anisotropic optical materials. Systematic studies of both disordered and ordered "phases" will be essential in differentiating the contributions of proximity and periodicity to the development of new collective electronic phenomena.

6.2 Experimental

6.2.1 General: All CdSe QD samples and precursors such as trioctylphoshine selenide (TOPSe) were prepared with the methods outlined in chapter 2. Anhydrous methanol, 1-butanol, 1-octanol, hexane, octane, pyridine, pyrazine, n-butylbenzene, toluene, tributylphoshine (TBP) and tributylphoshine oxide (TBPO) were purchased from Aldrich and used as received. Trioctylphoshine (TOP) was purchased from Fluka, trioctylphosphine oxide (TOPO) and dimethylcadmium (Me_2Cd) were purchased from Strem. Polyvinal buteraldehyde (PVB) was purchased from Aldrich.

6.2.2 Surface exchange: General concepts of ligand exchange outlined in chapter 5 are used extensively in the present work to adjust the chemical nature and dimension of the organic spacer layer. In each case portions of size selected CdSe QDs capped with native TOP/TOPO caps were first exchanged for pyridine and then exposed repeatedly to a large excess of the competing capping groups. In this way the pyridine capped crystallites provided a universal intermediate to permit the quantitative exchange of capping groups with similar solubility properties (e.g. TOP/TOPO for TBP/TBPO).

6.2.3 Preparation of Quantum Dot Glasses: A 300 mg portion of size selected CdSe quantum dots is dispersed in 2mls of a solution consisting of 90% hexane and 10% octane. The dispersion is stirred thoroughly until optically clear. The vial is fitted with a septum seal and allowed to stand at ambient temperature and pressure. The dispersion slowly evaporates becoming increasingly viscous over a period of weeks producing a single monolithic piece of optically clear glass.

Thin glassy films for optical studies and structural characterization are produced by placing a single drop of the concentrated dispersion (20% by weight) on the center of a substrate. The drop spreads radially producing a film less that one micron thick. Sapphire flats or silicon (100) wafers are used as substrates for optical and structural studies respectively. Radial variations in thickness produce concentric colored rings. The films dry rapidly but do not show significant cracking when the film thickness is kept below 1

μm. Samples were held at 80°C and 1 torr. for a period of ~1 hour to remove any entrained solvent.

Analogous procedures were used to deposit thin films of pyridine capped QDs from toluene dispersions. Modification of the deposition conditions were necessary for Pyrazine capped QDs. At room temperature these dispersions are unstable due to bridging flocculation. Warming the solution to 60°C prevents the formation of these networks and maintains an optically clear dispersion. These dispersions are spread directly onto the surface of substrate held in an oven at a 80°C and dried to produce a dense, optically clear film. Heating to 150°C under 0.1 torr for 3 hours removes any extraneous capping groups. Entirely inorganic QD films are produced by removing the pyridine capping groups were achieved by holding the sample at ~150°C under 0.1 torr vacuum for 3 hours.

6.2.4 Preparation of 3D Quantum Dot Superlattices: A 50 mg portion of size selected QDs is placed in a vial ~5 mls of a mixed solution of 90% octane and 10% 1-octanol is added to the vial with gentle stirring. The vial is then fitted with a septum seal. After puncturing the septum with a small bore needle the vial is placed in a vacuum oven at 80°C and the pressure slowly reduced. As the octane evaporates preferentially the dispersion becomes opalescent, indicating the formation of a crop of micron sized colloidal crystals. The precipitate containing the colloidal crystals is separated and spread on a substrate. The material is returned to the oven to remove any entrained solvent. Colloidal crystals assembled from crystallites smaller than 40Å in diameter display reduced thermal stability, requiring that the drying be carried out under reduced pressure and ambient temperature.

Oriented epitaxial films of quantum dots are produced by spreading 500 μl of the octane / octanol dispersion described above uniformly over a substrate. The dispersion is placed in an oven at 80°C and allowed to evaporate. The pressure is gradually reduced to ~1 torr and held for one hour to remove any entrained solvent. Spreading the dispersion on an ethylene glycol subphase followed by annealing at 80°C for 2 hours at ambient

pressure produces free floating ordered islands and regions of close packed monolayers. These free floating islands and monolayers can then be transferred to a solid substrate for support while drying under vacuum.

6.2.5 Electron Microscopy: Scanning electron microscopy (SEM): A JSM-6320F scanning electron microscope operating at 25KV was used to image the morphology of thick glassy films and ordered superlattices. Samples were prepared by the deposition of appropriately tailored dispersions directly onto the surface of silicon wafers and TEM grids (300 mesh Cu with 50Å of amorphous carbon coating). Thick samples were sputtered with a light coating of gold to prevent charging during observation.

Transmission electron microscopy (TEM): A Topcon EM002B transmission electron microscope was operated at 200KV for bright field imaging. Objective apertures were selected alternately to permit imaging of the (100), (002), and (101) wurtzite planes or to remove all lattice contrast leaving only contributions from z scattering and small angle electron scattering. Small angle electron scattering patterns were collected by reducing the operating voltage of the microscope to 80KV and employing a ~1.5 m camera length. Copper grids (300 mesh) coated with ~50Å of amorphous carbon were purchased from Ladd industries. Glassy and ordered epitaxial films were assembled directly onto the surface of TEM grids. The grids were held on the surface of a silicon (100) wafer with a thin film of ethylene glycol. A drop of an appropriately tailored dispersion was placed on the grid and allowed to spread radially. The grids were then placed in a vacuum oven at 80°C to allow the dispersion to evaporate. The pressure was gradually reduced to 0.1 torr over a period of 2 hours to complete the drying.

Cross sections of films were prepared by cleaving free floating islands formed on the glycol subphase. QD films are cooled with liquid N_2 and cleaved with a razor blade to produce fragments displaying all major crystal directions. Films of large QDs (i. e. >60Å) can be cleaved at room temperature.

6.2.6 Small Angle X-ray Scattering (SAXS): SAXS patterns were collected in a reflection geometry on a Rigaku 300 Rotaflex diffractometer with a 250 mm focusing circle. The accelerating voltage on the Cu anode was set to 50 KV and a flux of 300 milliamps for investigation of $2\theta = 4^{\circ}$ to 15°. The flux was reduced to 50 milliamps to examine the region $2\theta = 1^{\circ}$ to 4°. Diffraction and scatter slits of $1/6^{\circ}$ and 50 μm collection slits and a further 150 μm receiving slits were employed. Soller slits were used to limit the vertical divergence. This geometry permitted resolution limited peak widths of 0.07° fwhm at 2 degrees. Data was collected in 0.02° steps, averaging for 10-60 seconds per point.

A typical sample was prepared by depositing a dispersion directly onto the Si(100) wafer. The composition of each dispersion was tailored to adjust the length scale of ordering and the morphology of the sample.

6.3 Results and Discussion

6.3.1 Close Packed QD Solids (General) Close packed molecular solids are generally divided into two broad categories amorphous and crystalline. Amorphous materials display only short range order and are characterized by an average density and radial distribution of molecules. Crystalline solids exhibit long range 3D translational symmetry. Some new optical and electronic phenomena are proposed in both ordered and disordered packings of crystallites.[2] Production of close packed QD solids may allow a large enhancements in absorbance to be realized. Enhancements of optical non-linearities have been predicted in close packed QD solids.[1] More subtle differences have been predicted for glassy and ordered 3D arrays. Methods have been developed for the preparation of amorphous (glassy) and crystalline arrays of QDs both as macroscopic free standing structures and as the more technologically promising supported thin films.

Enhancement of the mass absorption coefficient mentioned in chapter 1 has important implications for thin film optical materials. A single close packed monolayer of 25Å diameter QDs with a capping shell of TOPO/TOPSe has an optical density 40 times that of an equivalent volume of bulk material and more than 100 times that of the

equivalent mass of bulk material. The high density of oscillator strength leads to correspondingly short penetration depths for photons in these QD solids. Although the material is optically clear (non-scattering) in transmission it exhibits a metallic-like luster in reflectance.

New optical properties which arise from the electronic coupling of neighboring crystallites are seen in simple room temperature optical measurements. There is a significant red shift in the emission of the ensemble of crystallites in the solid compared to the dispersion. Figure 6.1 shows absorption and emission spectra for a close packed glassy film of 62Å QDs in solid lines. The dotted line represents the luminescence of the dispersion prior to casting the film. The absorption of the dispersed and solid samples were indistinguishable at room temperature. The observed shifts are reversible upon redispersion of the solid samples. Similar shifts have been recognized by other investigators as indicative of collective phenomena although the mechanism of the coupling has remained elusive.[6,7] Kagan has recently investigated the dynamics in close packed QDs solids with a combination of spectroscopic and structural probes and has develop a model involving long range energy transfer between proximal dots.[17] Detailed optical and structural studies are needed to map out the structure / property relations in these QD solids.

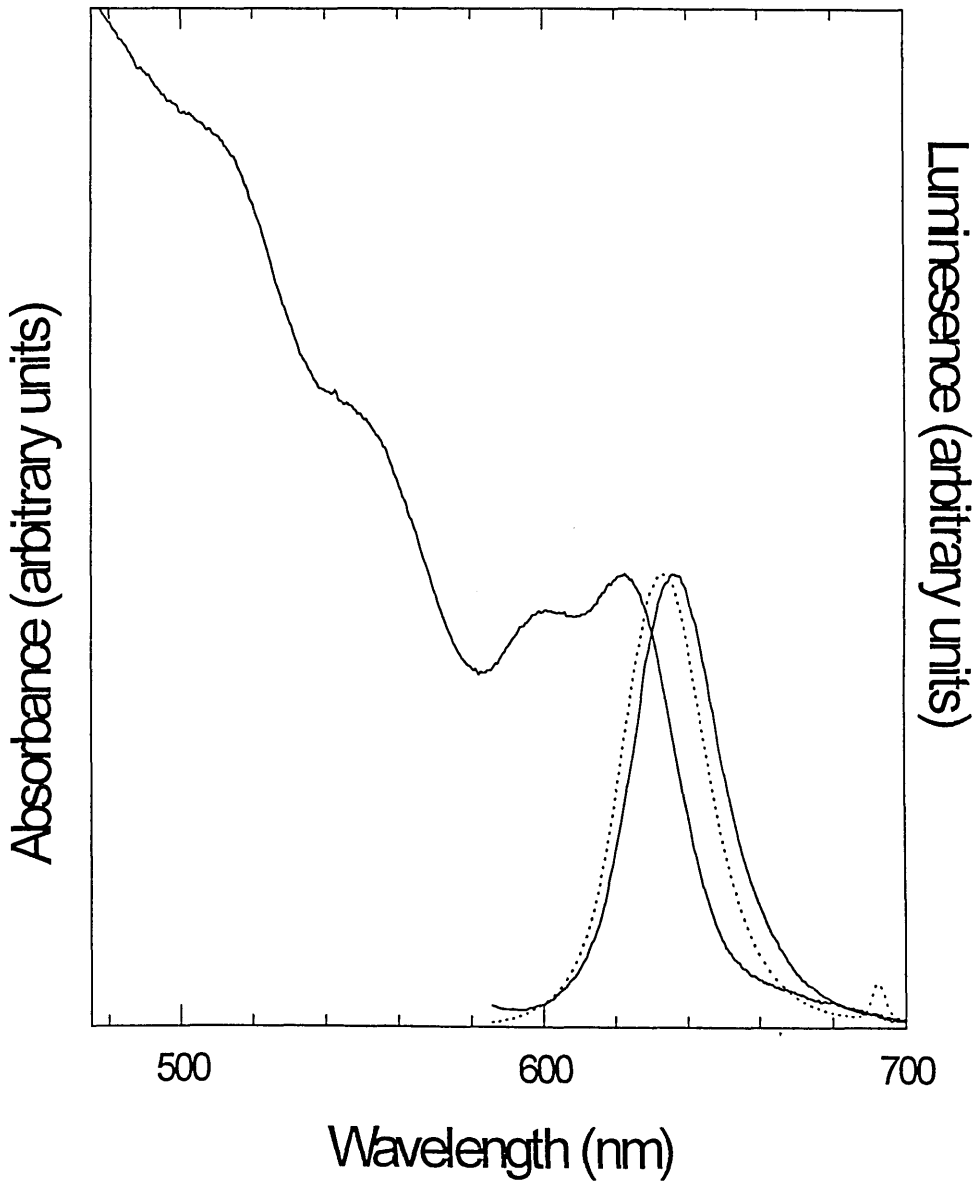

FIG. 6.1 Room temperature optical absorption and emission spectra for a glassy film of ~63Å diameter CdSe nanocrystallites are shown as solid lines. The dotted line indicates the emission from dispersed nanocrystallites in solution (C.R. Kagan).

6.3.2 Quantum Dot Glasses: We produce close packed glassy solids by tailoring the solvent composition to maintain the stability of the crystallites as the dispersion is concentrated. Close packed glassy solids displaying a well defined nearest neighbor spacing result from evaporation of the solvent from the nanocrystalline dispersions (alkanes). As the concentration of QDs approaches 20 to 30% by weight, a rapid increase in the dispersion viscosity is noticed. The QDs begin to interact significantly through a simple hard sphere repulsion. Further evaporation to ~50% by weight results in the formation of gels filling the volume of the container. Over a period of weeks the gels shrink isotropically, pulling away from the walls of the container, and ultimately produces optically clear monolithic solids. Single pieces as large as 1 cm^3 have been produced. The structure does not exhibit detectable porosity. Measurements of the density of the solids exceed 80% percent space filling and are consistent with the dense random packing of hard spheres with soft shells (capping groups filling the voids). The solids are hard materials and fracture under stress. Figure 6.2A shows a SEM micrograph of a QD glass prepared by evaporation of a dispersion of 64Å diameter QDs onto a silicon wafer, the sample was lightly coated with gold to prevent charging during the observation. This 240 μm thick film displays conchoidal fracture lines characteristic of brittle fracture in glassy solids. Neither macroscopic nor microscopic porosity is evident. To produce these monolithic glassy structures the evaporation of the solvent must occur very slowly. Significant strains are introduced by shrinkage of the solid during drying and slow evaporation is essential to avoid extensive cracking in the large structures.

When the glasses are prepared as films of submicron thickness cracking is dramatically suppressed or even eliminated producing uniform optically clear material extending over regions as large as 10 cm^2. The absorption edge of the solids can be engineered through control of the individual QD size. Figure 6.2B shows a TEM micrograph of a thin section of a glassy film of 53Å diameter CdSe QDs. Careful examination of the dense, disordered arrangement reveals a relatively uniform center to center distance between nearest neighbor QDs. Development of the average description of the structure within these solids is best done with a technique which simultaneously probes a large volume of the sample.

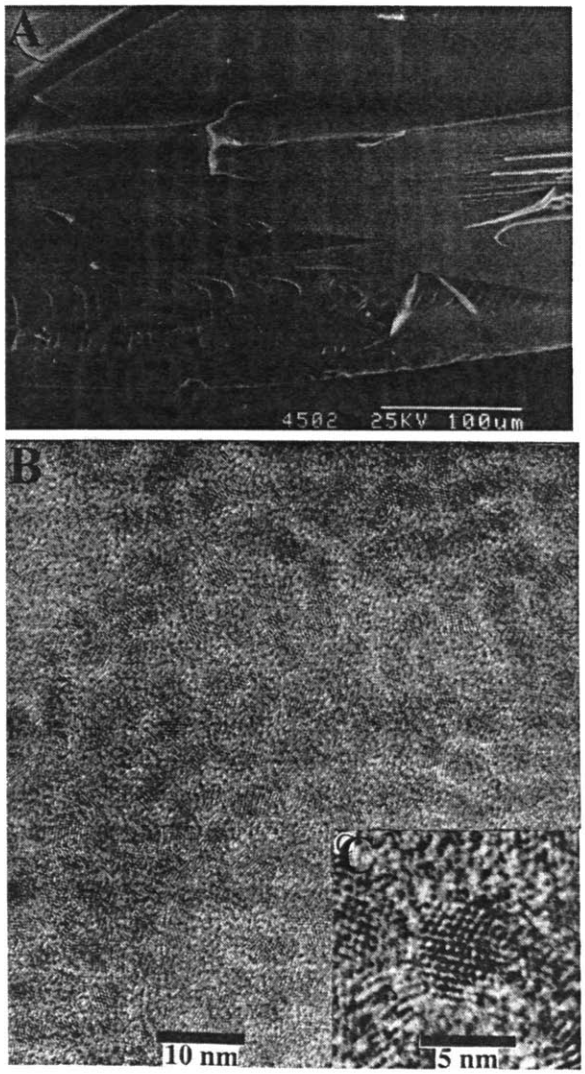

FIG. 6.2A SEM image of a 240 μm thick film of 63Å diameter CdSe nanocrystallites. The conchoidal fracture lines observed are characteristic of brittle fracture in amorphous solids. There is no microscopic or macroscopic porosity.

FIG. 6.2A TEM of a thin section of a glassy film of 53Å diameter CdSe nanocrystallites. The nanocrystallites display dense random packing.

SAXS studies allows us to develop a model of the average structure in these QD glasses. Each quantum dot acts as a scattering center with its individual scattering pattern serving as the form factor for the elements in the structure. In concentrated dispersions and colloidal solids the positions of the particles become correlated and the small angle scattering is modulated by the interference between particles. Figure 6.3(A) shows a series of SAXS spectra taken in reflection geometry and plotted on a log scale. Dotted lines are the scattering of ~1% dispersions of QDs in PVB (seen in chapter 4), solid lines represent the scattering from ~1 to 0.5 μm thick glassy films of QDs. The inter particle interference produces a peak in the small angle scattering. Analysis of this peak by direct application of the Bragg equation is not appropriate and does not yield the interparticle spacing.

A general formulation of the scattering from an arbitrary collection of N particles is given in equation 6.1.[18]

(6.1) $$I(q)\text{total} = I(q)NF^2(q)S(q)$$

The structure factor S(q) is the interference introduced by the correlation between the position of the particles. This structure factor can be extracted from the experimental data by dividing the scattering pattern of the glassy films with the pattern of the particles dispersed in PVB. When the particles are dilute, their positions are uncorrelated and thus S(q) is ~ 1. The scattering intensity from a dilute dispersion is $\sim I_o N F^2(q)$. Equation 6.2 expresses the structure factor in terms of an average radial distribution ρ(r) of particles about an arbitrary reference atom.

(6.2) $$S(q) = 1 + \frac{4\pi\rho_o}{q}\int_0^\infty r[\frac{\rho(r)}{\rho_o} - 1]\sin(qr)dr$$

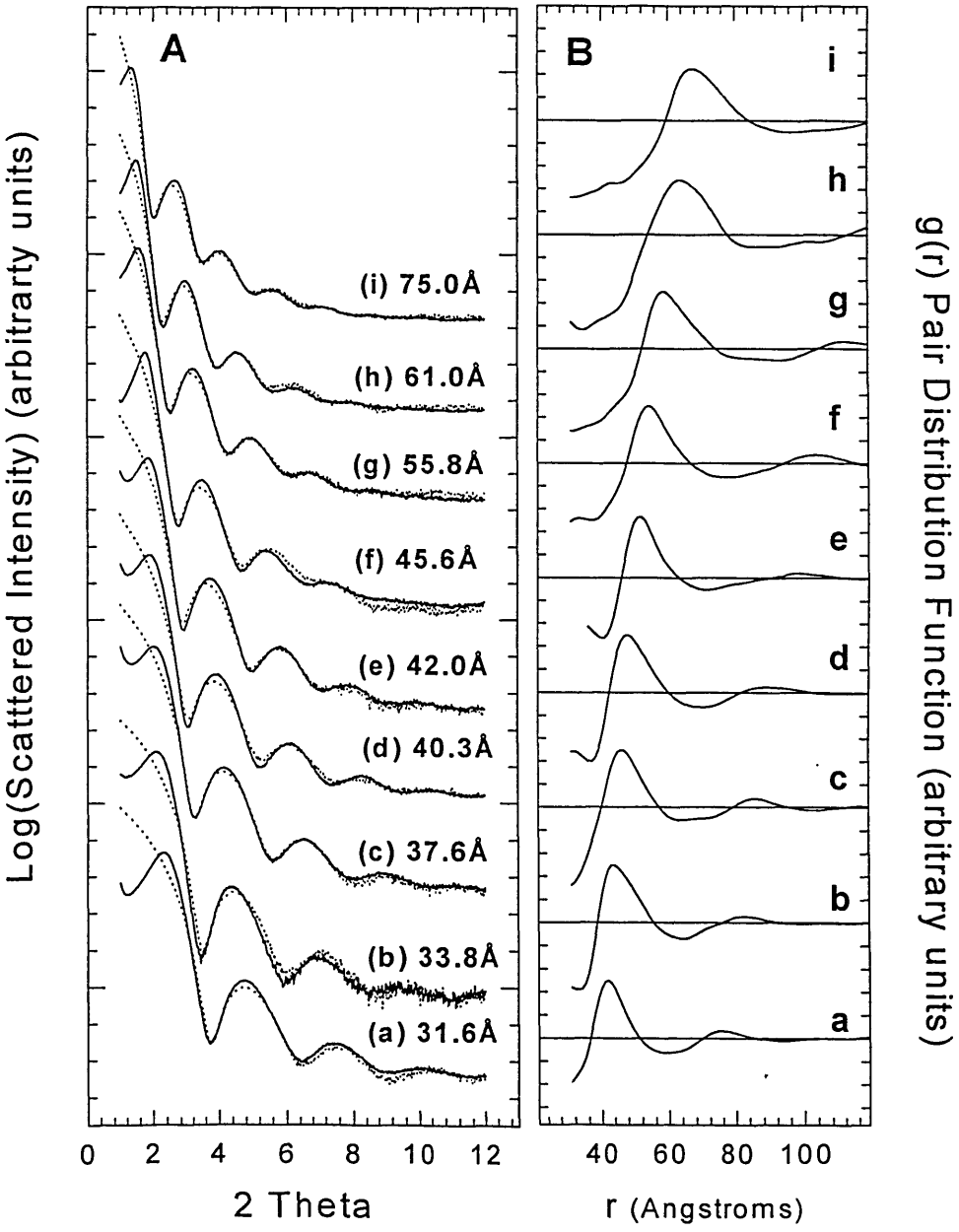

FIG. 6.3A Experimental SAXS patterns for a series of CdSe samples ranging from ~32Å up to 72Å in diameter. Samples dispersed in PVB are shown as dotted lines while glassy thin films are shown as a solid line.

FIG. 6.3B Pair Distribution functions, g(r), extracted from the data. TOPO /TOPSe caps maintain an average inter particle spacing of 11±1Å.

This structure factor can be Fourier transformed to yield a pair distribution function g(r) where $g(r) = \rho(r)/\rho_o$. Experimental observations are limited to angles between 1° and 12° 2θ and thus the data must be rationally extrapolated at the ends of the experimental range to minimize truncation errors. The methods described in reference (19) were employed to minimize spurious features and to extract a pair distribution function. In particular the exponential damping term ae^{q2} was required to suppress the effects of decreasing signal to noise at wider angles (2<a<6).[19] The positions of the nearest neighbor peaks are unaffected by the damping term, however the overall resolution is decreased and the areas under each feature in the g(r) no longer permit extraction of the average coordination number. We extract the pair distribution function for each sample using expression 6.3.

$$g(r) = 1 + \frac{1}{2\pi^2 r\rho_o}\int_0^\infty [S(q) - 1]q\sin(qr)dq \qquad (6.3)$$

Figure 6.3B shows the corresponding pair distribution functions for each of the samples representing the average center-to-center distances in the solids. A number of nearest neighbor orientations is possible in aggregates of elliptical particles. The analysis of each sample is conducted using the approximation of an equivalent radius for the particles. Results indicate the thickness of the capping layer between each quantum dot is ~11± 1Å. When these structural studies are combined with macroscopic measurements of the density a consistent description of the solids is possible.

When there is a weak repulsive interaction between crystallites there is no significant energy driving the formation of an ordered lattice. As the concentration rises, the free volume available to each dot is smoothly reduced and the viscosity of the dispersion rises. This ultimately freezes in the local structure of the dispersion. The formation of the glasses is reversible at any step by gradual addition of fresh solvent. These solids have liquid like radial distribution functions resembling the frozen packing of "hard spheres with soft shells".

6.3.3 Engineering of the Interdot Spacing: Establishing control over the dimension and chemical nature of the spacer group between each QD is essential in mediating the coupling of the dots. Ligand exchange techniques have been developed to optimize the stability of the dispersions in a variety of solvents and polymer matrices. They now provide precise control over the organic interlayer in assembled QD solids. Figure 6.4A shows the SAXS results when the native TOPO/TOP capping groups are exchanged for the less bulky TBP/TBPO groups. The interdot spacing is reduced from ~11Å to 7Å. In this simple fashion the bulk of the alkyl groups can be used to precisely tune the interdot spacing.

Trialkylphosphine groups can be replaced with pyridine and its derivatives to produce a distinct family of QD solids. Although dilute dispersions of pyridine capped QDs in toluene remain optically clear on standing for more than a year, SAXS studies of these systems show they are only metastable. Pyridine capped QDs maintain a weak net attractive potential between the QDs in solution. Evaporation of pyridine capped QD dispersions in toluene produces optically clear thin films analogous to those described earlier. These films display domains of longer range order dispersed within a predominantly glassy background. Unlike the trialkylphoshine moieties pyridine is highly volatile and weakly bound to the quantum dot surface. Gently heating the pyridine capped films (~150 to 175°C) under 0.1 torr vacuum quantitatively removes the pyridine from the thin films leaving an entirely inorganic superstructure. The optical features of the new inorganic films are red shifted from those of the isolated particles but remain to the blue of the bulk band gap as they come into intimate contact. The TEM image in figure (6.4) shows a region of a thin film that has been assembled with pyridine caps and heated under vacuum. Ordering is seen as lines of QDs running vertically in the image. The majority of this sample shows ordering on a much shorter range, extending over the 2nd to 3rd nearest neighbor shell. Figure 6.5C curve (c) shows the scattering from a thin film of pyridine capped quantum dots. Pyridine groups maintain a ~7Å spacing between the QDs. Curve (e) displays the scattering of a film heated under vacuum to remove the pyridine. The radial distribution function indicates that the superstructure has collapsed to less than a 2Å spacing between particles, indicating intimate contact. The removal of the

organic groups produces a thin solid film with extraordinarily high surface area. As the interparticle spacing collapses a nanometer sized pore structure remains as the particles can not exceed the closest packing of spheres (75%).

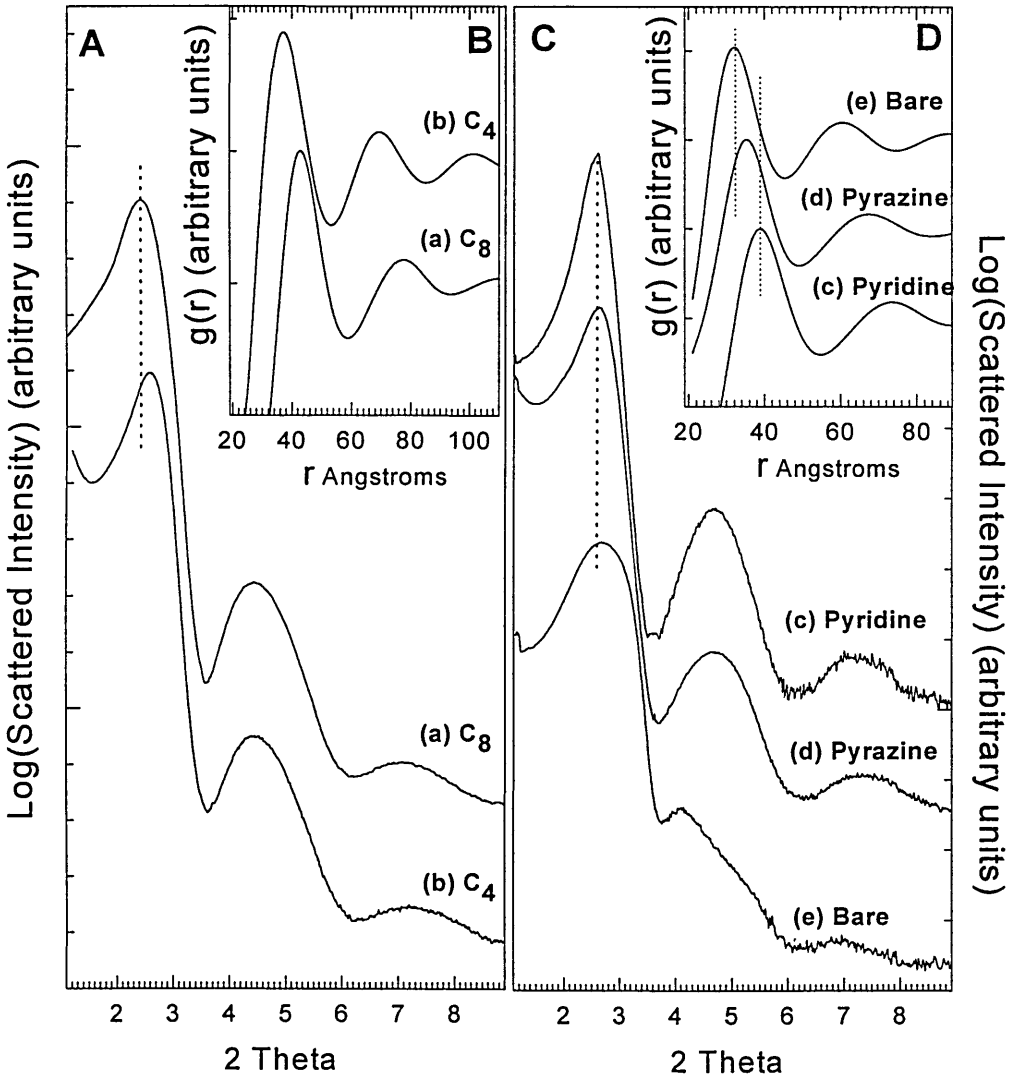

FIG. 6.3 (A) SAXS patterns for close packed glassy films of 32Å QDs with TOPO caps (a) and TBPO caps (b). Inset (B) shows the pair distribution functions g(r): with an ~11Å interdot spacing in film (a) and the ~7Å spacing in film (b).

FIG. 6.3 (C) SAXS patterns for glassy films of 34Å QDs with pyridine caps (c), pyrazine caps (d), and bare semiconductor surfaces (e). Inset (D) shows the pair distribution function g(r) : with inter dot spacings of ~7Å, 5Å, and <2Å in films (c), (d), and (e) respectively.

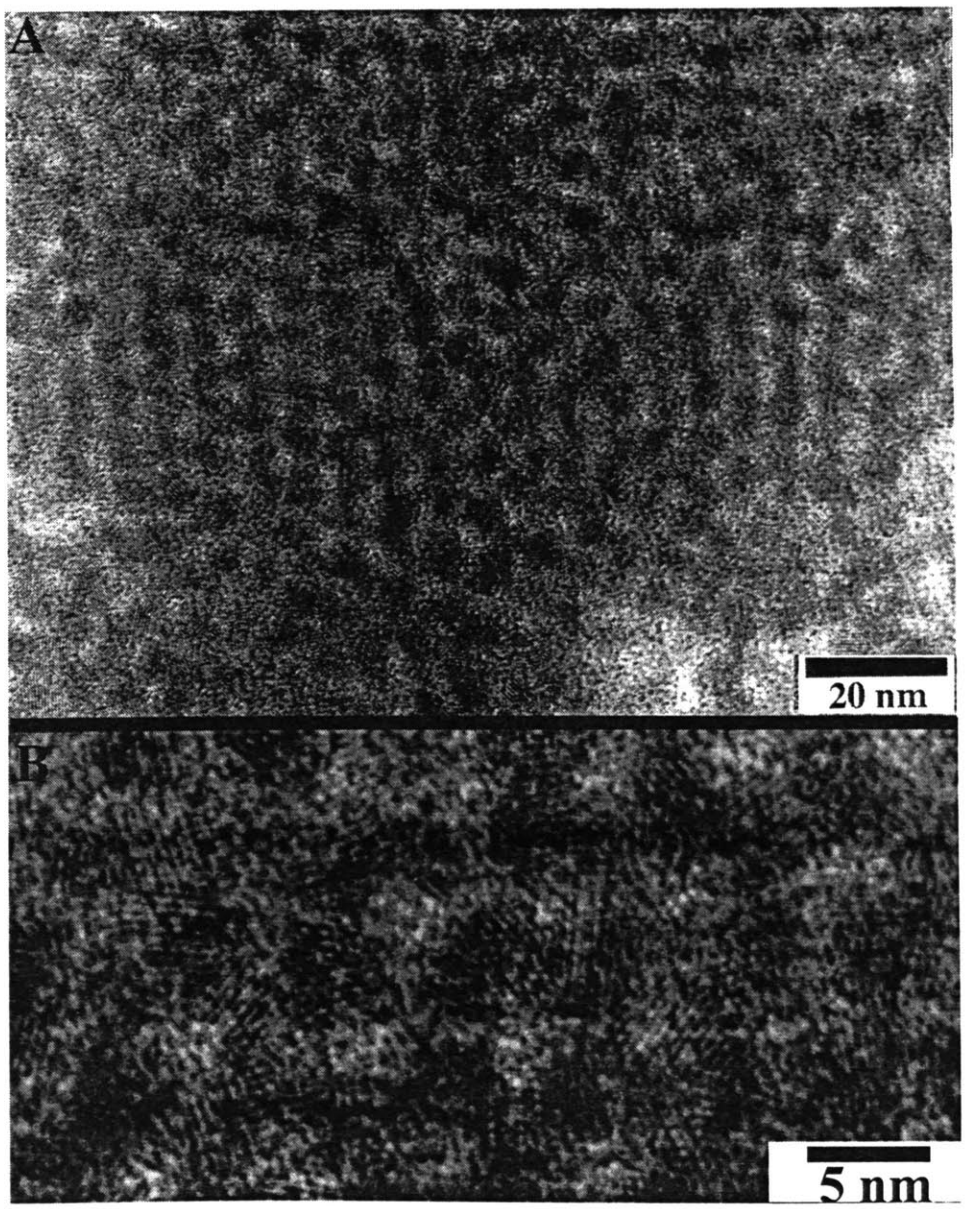

FIG. 6.4 TEM image of a portion of a CdSe superstructure produced by assembly of a pyridine capped thin film and subsequent removal of the pyridine. The image shows an ordered domain with lines of particles running vertically. The crystallites are in intimate contact but are not sintered. An expanded view is shown below.

Cross linking of the particles in the solid state has the potential to produce materials which are thermally and mechanically robust materials. Pyrazine (1,4 azobenzene) is a ligand with the potential to produce such cross-linking. Pyrazine capped CdSe QDs dispersed in toluene are unstable at room temperature, consistently producing a low density flocculate upon standing (a related flocculant, 4,4' bipyridyl has also been studied).[20] Evaporation of the dispersion at room temperature produces low density translucent films. Heating the dispersion to ~80°C provides sufficient thermal energy (Brownian motion) to disrupt the flocs and produce an optically clear dispersion. Evaporation at 80°C results in optically dense and clear films. Heating to 150°C under 0.1 torr vacuum removes any extraneous pyrazine and solvent but leaves the absorption features in the film largely unaltered. The SAXS pattern shown in curve d of figure 6.3 indicates that the QDs are separated by a 5Å spacing, consistent with the dimensions of bridging pyrazine molecules.

6.3.4 Transition from Local to Long Range Order: The formation of glassy solids is achieved by ensuring that the dispersion maintains a net repulsive potential between the crystallites during the evaporation process. A weak repulsive potential provides little energetic driving force for the formation of long range order and hence a regular crystalline lattice. An attractive potential between pyridine capped QDs has been measured by SAXS. This attractive potential permits the development of regions of extended order.

Tailoring the composition of the dispersing medium to provide a slow destabilization of the dispersion as the solvent evaporates allows the production of 3D superlattices of QDs coherent over hundreds of microns. The procedure involves the evaporation of a mixture composed of a low boiling alkane and a high boiling alcohol. Two solvent recrystalization methods are common in the growth of molecular crystals. As the dispersion is concentrated the relative concentration of the alcohol rises slowly reducing the steric barrier to aggregation, and causing a slow separation of the QDs from the dispersed state. If the rate of the transition is carefully controlled, the sticking

coefficient between the QDs remains small and the QDs have sufficient time to find equilibrium lattice sites on a growing structure.

Figure 6.5 shows a cross-section through a film of 100Å quantum dots assembled as an island floating on the surface of a pool of ethylene glycol. Initially the evaporation, rate of the octane/octanol dispersion was adjusted to provide a slow evaporation permitting the organization of a 3D ordered superlattice in the bottom of the film. After ~3/4 of the dispersion was deposited the pressure over the system was rapidly reduced resulting in a sudden increase in the flux of QDs to the growing superlattice as the solvent evaporated. With insufficient time to find equilibrium lattice sites the Qds have formed a close packed glassy layer. Figure 6.6 shows the top view of a film of 30Å QDs deposited directly on a TEM grid from a solution of 1% octanol in octane. Regions of glassy and 3D superlattice domains coexist (upper right and lower left) with a glassy region (center). Each of the domains is oriented with the <111> axis perpendicular to the substrate. The inset shows the electron diffraction pattern from a 2 μm diameter region surrounding the real space image. Portions of both the small angle electron diffraction from the 3D superlattice domains and the wide angle electron diffraction pattern of the individual crystallites are seen. An inner ring indicated by the arrow is seen to be composed of a series of discrete spots consistent with the (440) reflection fcc superlattice. Reflections from an ensemble of domains each oriented with the <111> axis perpendicular to the substrate but randomly oriented in the plane of the substrate make up this pattern. Moving radially outward the next ring is a convolution of the (100), (002), and (101) reflections of the individual crystallites. In each ordered domain there are QDs orienting with their <002> axis in the plane of the substrate (as noted in chapter 4) making the (002) reflections particularly intense.

FIG. 6.5 TEM of a cross section through a <111> oriented island. The sample was cleaved along the <111> axis. The top of the image shows a glassy region formed at high growth rates. The bottom shows the long range order possible with slow growth. Striations seen are the <112> fcc planes.

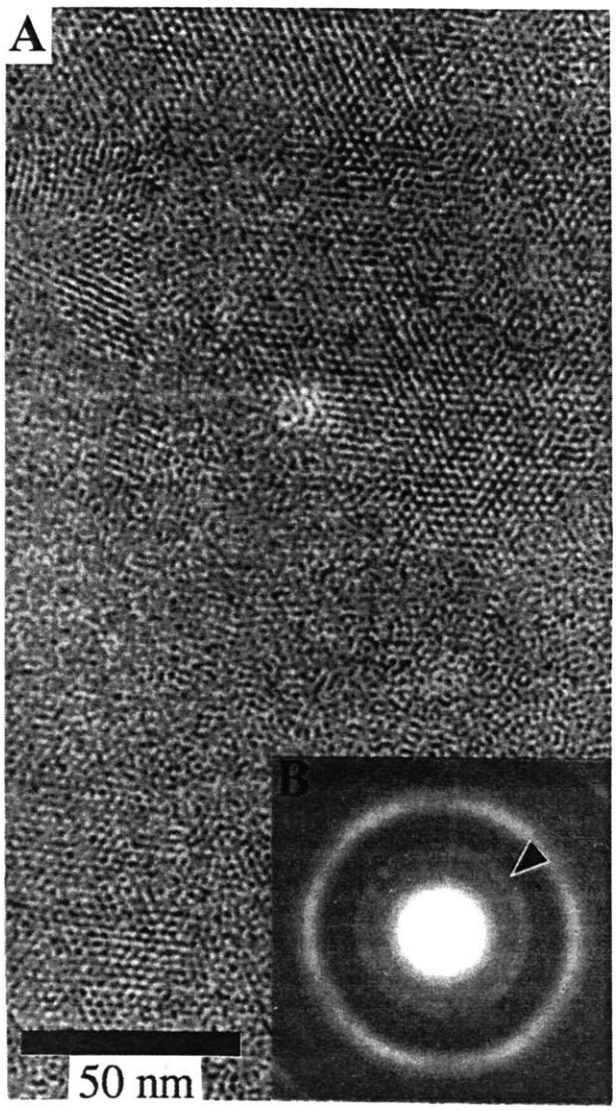

FIG. 6.6 TEM image of a thin film of 34Å QDs displaying coexistance of regions of short range order (center) and long range order (upper right and lower left). The small angle electron diffraction pattern for a region 2μm in diameter is inset. An arrow marks a series of spots from the (440) reflection of the superlattice indicating the presence of many ordered domains. Domains are oriented with their <111> axis perpendicular to the substrate.

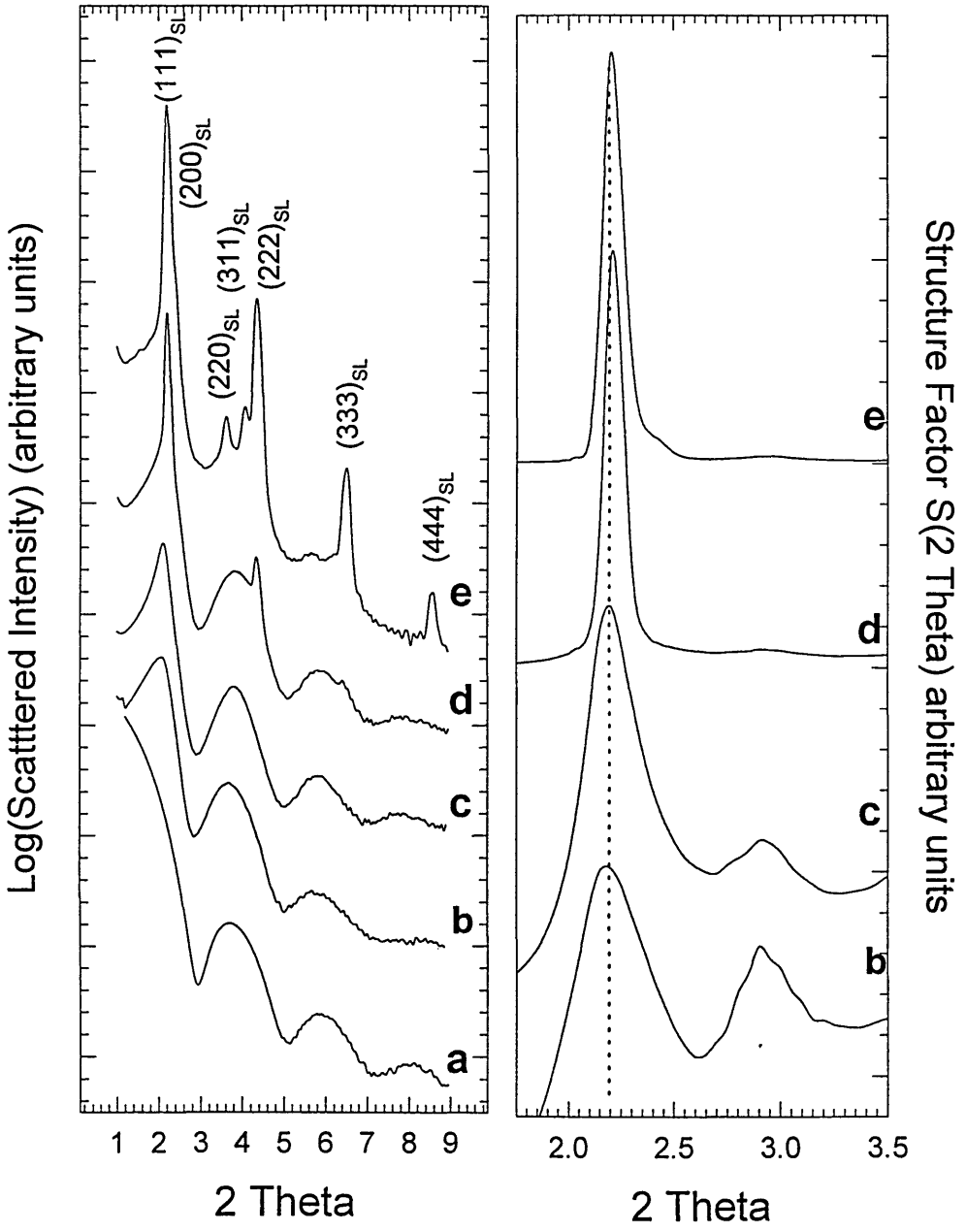

FIG. 6.7A SAXS spectra for a series of thin films assembled with 34Å QDs. (a) shows the pattern from a dilute dispersion in PVB, while (b) through (e) show progessively increasing order with adjustments in the deposition conditions. Details of deposition are found in the text.

FIG. 6.7B Structure factors extracted for each of the thin film samples. Shifts in the position of the SAXS peak are due to sharpening rather than a shift in structure factor.

SAXS allows us to characterize a series of films displaying the structural transition from glassy solids to large oriented 3D superlattices as the concentration of the dispersion and composition of the dispersing solvent are varied. The results are displayed in figure 6.7. Figure 6.7A shows the raw scattering patterns while panel B represents the extracted structure factors. Curve (a) displays the scattering from 34Å diameter QDs dispersed in a PVB matrix. Curve (b) shows a glassy pattern for sample b produced by deposition of 20% by weight dispersion of these QDs in pure octane. Sample (c) is a film deposited from a 1% by weight dispersion with 0.5% octanol and 99.5% octane. Panel (B) clearly shows the sharpening of the scattering pattern due to the narrowing of the structure factors. Sample (d) was prepared with a 1% by weight dispersion in 1% octanol (similar to the sample shown in figure 6.6) and displays the sharp reflections of an FCC lattice with a significant glassy background. Large oriented, ordered domains coexist with the glassy regions. It is important to note that the change in peak position of the SAXS patterns in curves (c) and (d) is largely the result of a sharpening and not of a large shift in the structure factor. Simple application of the Bragg equation would introduce a significant error in the measurement of the interparticle spacing. Finally curve (e) shows the result of depositing a film from a 0.1% by weight dispersion in 5% octanol. The pattern clearly shows fcc superlattice reflections.

Thus rational modifications of dispersion conditions allow us to control the deposition of nanocrystallites and hence the stucture of the solid superstructures produced. Figure 6.8 summarizing these obsevations. The TEM images show glassy and ordered solids prepared from the same initial sample of 80Å diameter QDs.

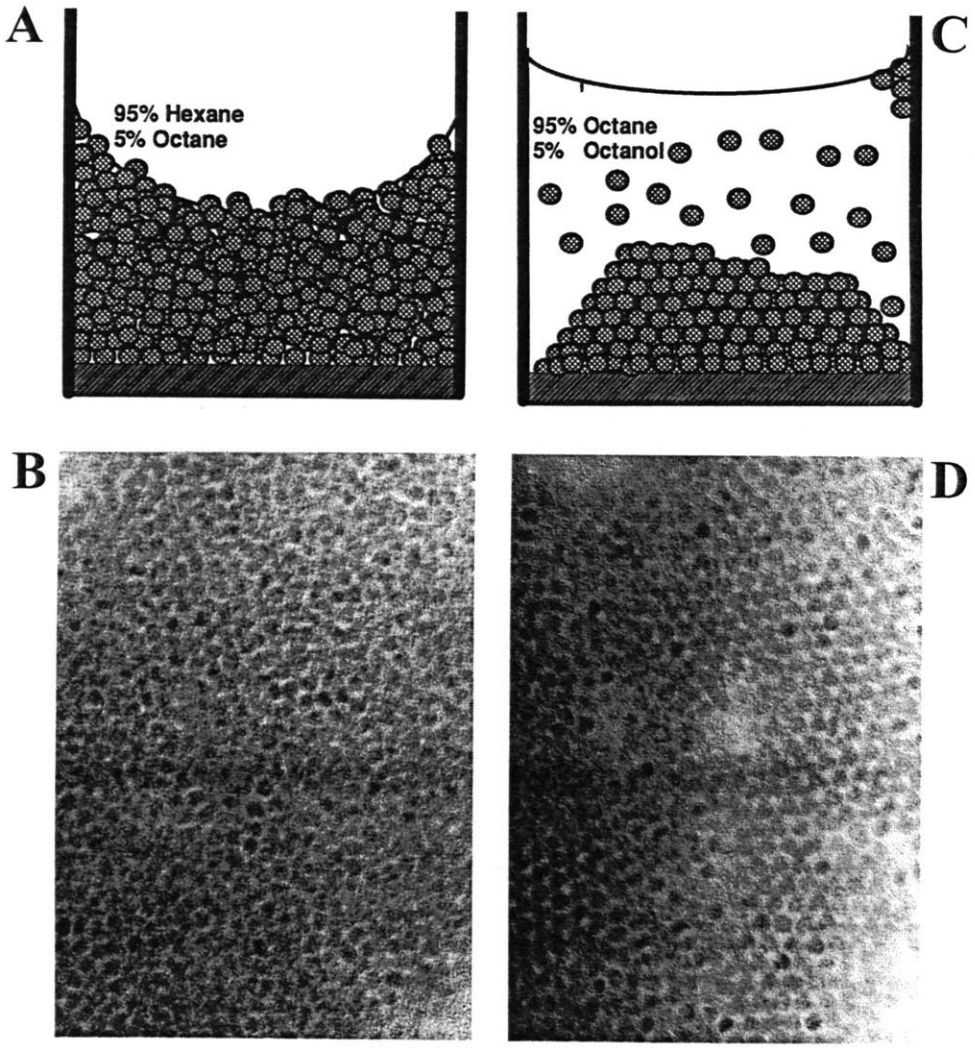

FIG. 6.8 (a) Cartoon of the general conditions for the formation of close packed glasses with (b) TEM image of the glass formed by deposition of 80Å diameter CdSe nanocrystallites.
(c) Cartoon of the general conditions for the formation of 3D superlattices with (d) TEM image of the 3D superlattice of 80Å diameter CdSe nanocrystallites.

6.3.5 Formation of 3D Quantum Dot Superlattices: Sub-micron sized colloidal crystals are produced by placing a vial containing a 0.5% by weight dispersion in 10 mls of 10% octanol and 90% octane in a vacuum oven at ~80°C and slowly lowering the pressure. As the dispersion evaporates a critical point is reached at which colloidal crystals nucleate uniformly throughout the dispersion. The contents of the vial become an opalescent suspension as the colloidal crystals grow to dimensions comparable to the wavelength of light. The colloidal crystals range from ~500 nm up to 2 μm in size and are remarkably uniform in size and shape for a given preparation. The evaporation process is stopped and the colloidal crystals are collected from the bottom of the vial. The material is spread on a substrate at 80°C while the pressure above the substrate is reduced to 1 torr to remove all the residual solvent. Figure 6.9A shows a faceted colloidal crystal with 60Å diameter QDs sitting in orderly rows producing well defined edges and vertices. An expanded view of one edge is seen in figure 6.9B. The star shaped pattern in the center of the structure is an electron channeling pattern of a $<111>_{SL}$ projection. This pattern clearly reveals the structure to be a single colloidal crystalline domain. Similar initial dispersions allowed to evaporate at room temperature produce much larger colloidal crystals, up to 50 μm along their largest face. These optically clear structures are sufficiently stable mechanically to be handled with fine forceps.

Figure 6.10 shows an optical micrograph with faceted platelets grown from a dispersion of 20Å diameter CdSe QDs, viewed under linear cross-polarization (dark field). Individual platelets range from ~5 to 50 μm. The colors seen result from the absorption of blue light, the broad emission of yellow light, and strong birefringence at green wavelengths near the band edge. Faceting and strong birefringence are important macroscopic evidence for not only the ordering of the individual crystallites but of the net orientation of their unique crystallite axes within the arrays. Figure 6.11 shows the luminescence of a similar collection of crystallites excited with 420 nm light. The brilliant yellow is the luminescence of the 3D Quantum dot superlattices. These 3D superlattices are a fundamentally new optical material.

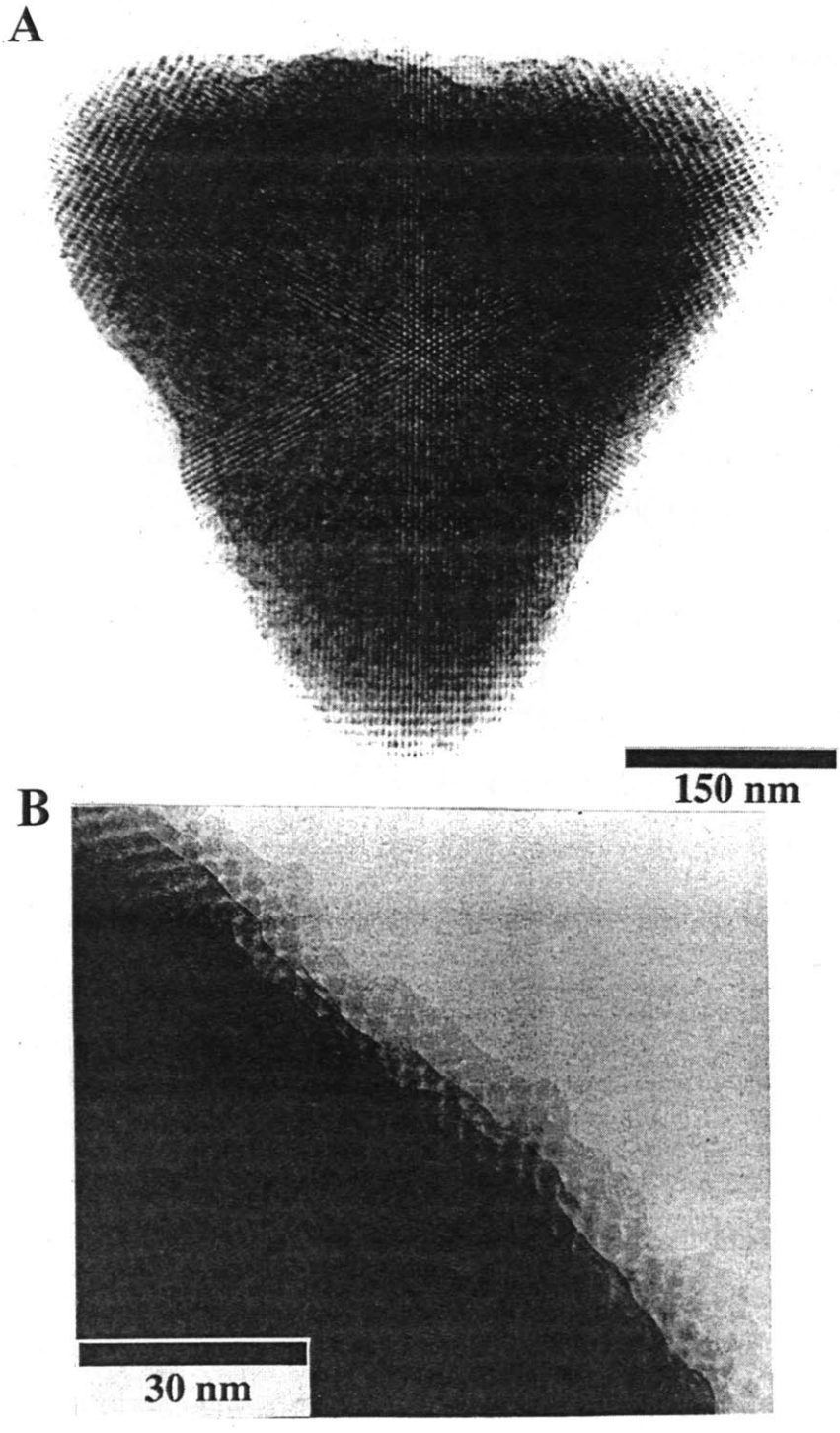

FIG. 6.9A TEM image of a faceted colloidal crystal is seen with 60Å QDs sitting on regular lattice sites producing sharp facets and vertices. A star shaped electron channeling pattern dramatically demonstrates the order throughout the structure.
FIG. 6.9B The individual 60Å QDs making up a facet are seen at higher magnification.

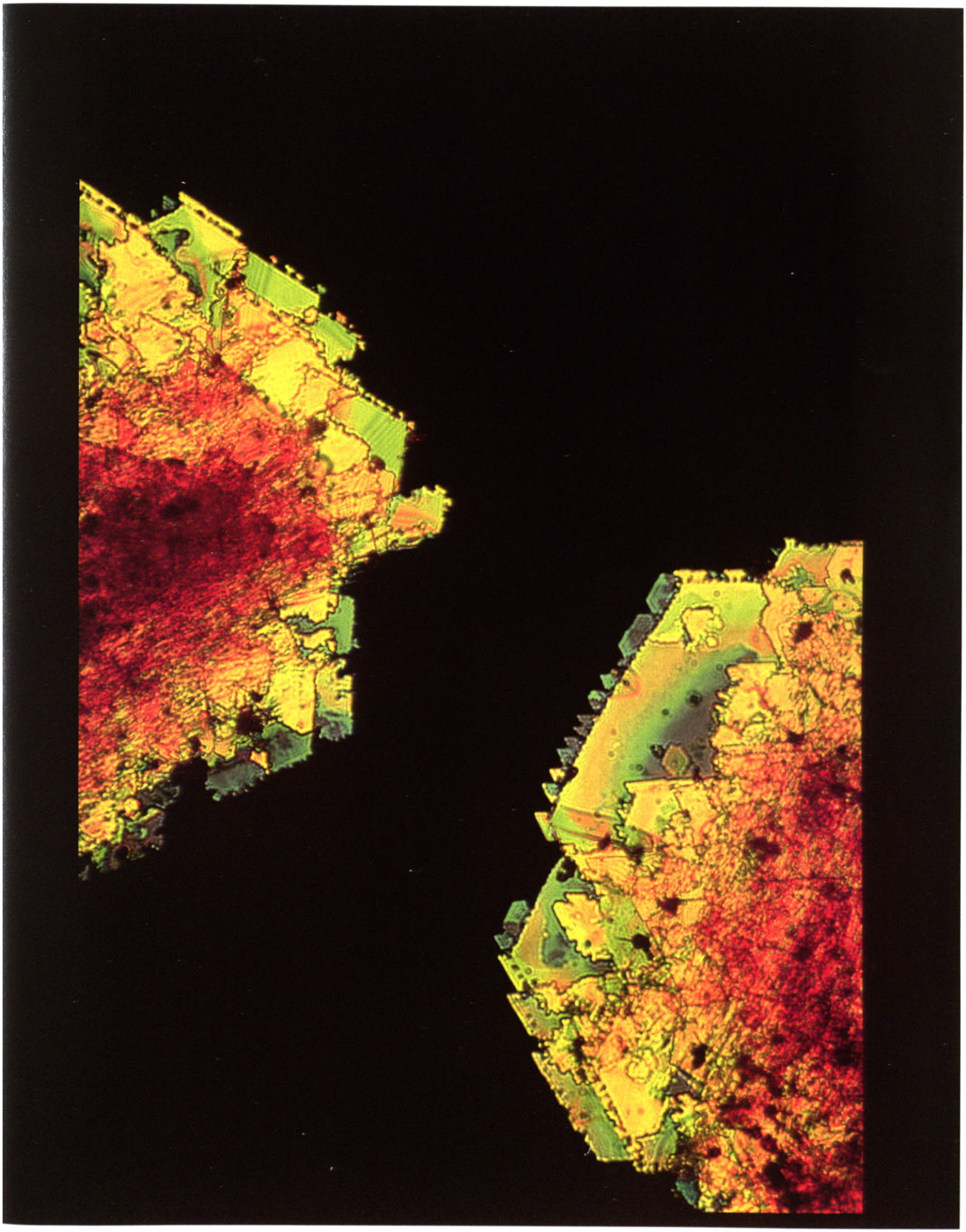

FIG. 6.10 Darkfield optical micrograph of faceted colloidal crystals. These stacked crystals range from 5 - 50 μm and are formed by self-organization of 20Å diameter CdSe QDs. The colloidal crystals are on quartz, back illuminated with linearly polarized white light, and detected at cross polarization.

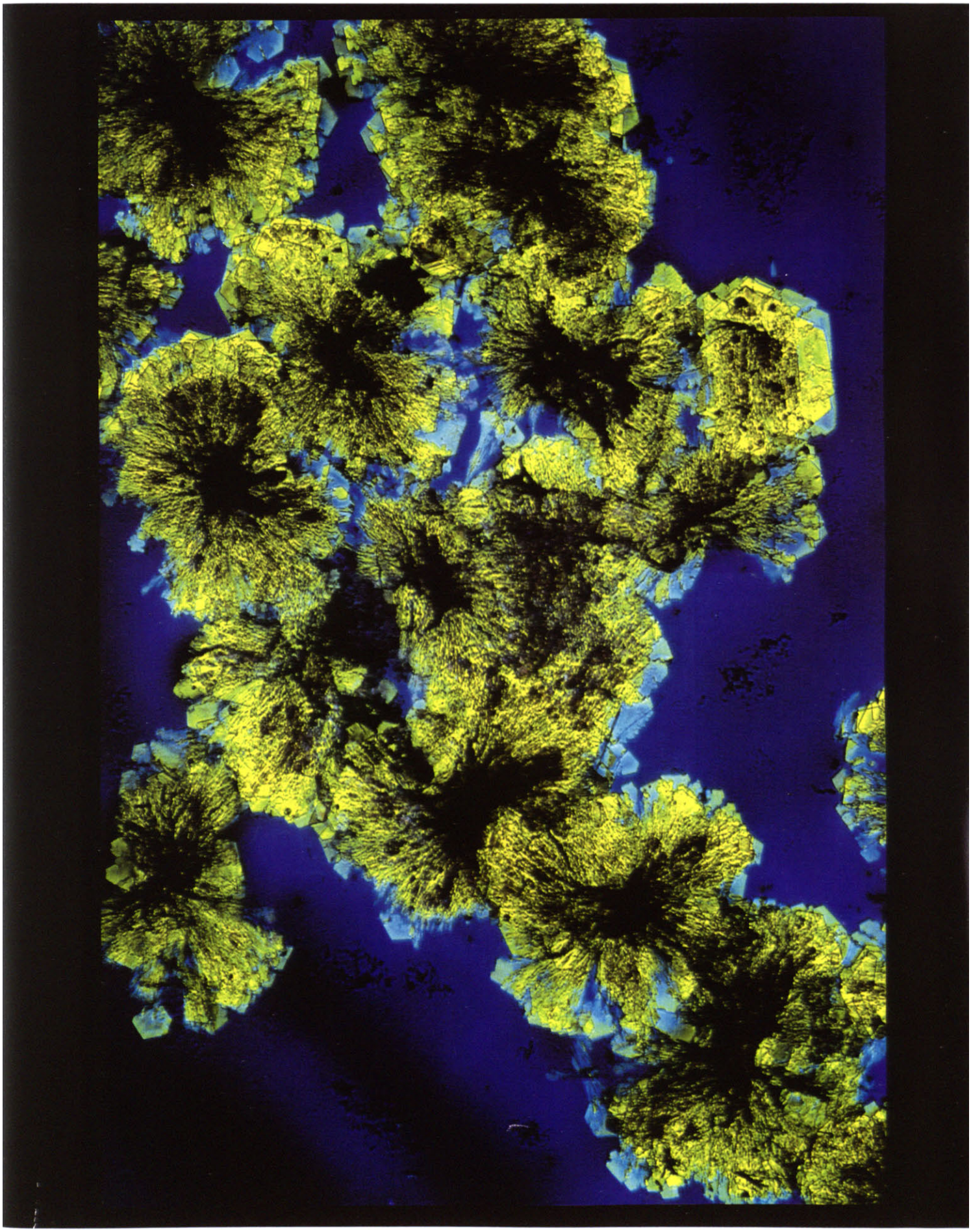

FIG. 6.11 Shows a luminescence micrograph of a collection of faceted colloidal crystals. The 3D superlattice of 20Å diameter CdSe QDs emits in the yellow under excitation with 420 nm (blue) light.

Spreading of the dispersion at an interface maximizes heterogeneous nucleation and allows the production of oriented epitaxial thin films. Approximately 80% of the ordered domains are organized with their close packed $(111)_{SL}$ planes parallel to the substrate. We use the subscript (SL) to differentiate the axis of the superlattice from those of the individual crystallites. Figure 6.12 shows a HRSEM image of the oriented domain, clear steps and ledges are formed by layers of close packed 64A QDs. A cartoon representing the classic terrace-ledge-kink model for monatomic crystals is shown below. The epitaxial film was heterogeneously nucleated on the surface of an amorphous carbon substrate. Slow addition of quantum dots to the steps and ledges produces low index planes on extended faces. The TEM image in figure 6.13 shows several of these $<111>_{SL}$ oriented domains. This image of the superlattice bears a striking resemblance to the thin colloidal crystals of iron oxide particles investigated by Bentzon *et al* [11,12] and thus reinforces the generality of the phenomena.

Although ~80% of the domains are $<111>_{SL}$ oriented, TEM surveys reveal other superlattice orientations growing at the grain boundaries and defects in the substrate. Figure 6.14 shows a TEM micrograph characteristic of the $<100>_{SL}$ projection through an fcc superlattice of 48Å diameter quantum dots. The inset shows a blow up of the superlattice, columns of atoms that make up each quantum dot are clearly seen. The small angle electron scattering pattern of a 2 μm region of the superlattice is also shown. Slight distortions of the lattice seen in the real space image are caused by heating by the electron beam during observation. In analogy to bulk crystalline solids ordered films undergo melting when heated. Figure 6.15 shows the results of heating a portion of a $<100>_{SL}$ oriented array with the energy of a focused electron beam. Bulk flow and streaming of particles can also be observed. Melting leads to the formation of glassy regions. Extensive TEM surveys reveal that crystal imperfections in these superlattices include dislocations, stacking faults and twins. A projection through another portion of this sample is shown in figure 6.16. In this $<101>_{SL}$ projection QDs are stacked in columns, providing high contrast. The white space surrounding each particle is the organic capping shell. The characteristic stripes of the $<112>_{SL}$ are seen in figure 6.17.

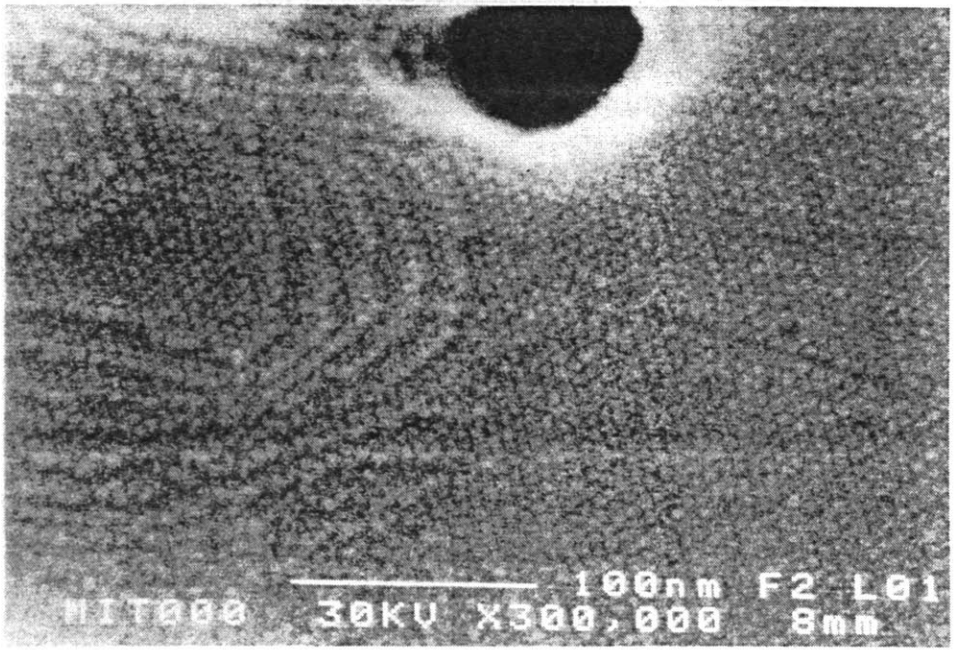

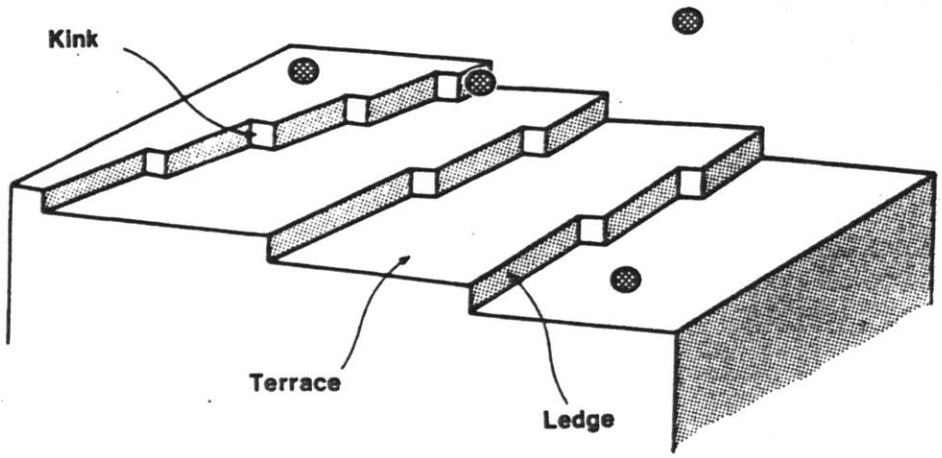

FIG. 6.12A HRSEM of a 3D superlattice of 64Å QDs grown epitaxially on an amorphous carbon substrate. Ordered rows of dots form ledges and terraces.
FIG. 6.12B Cartoon of the terrace, ledge, kink model of monatomic crystal growth.

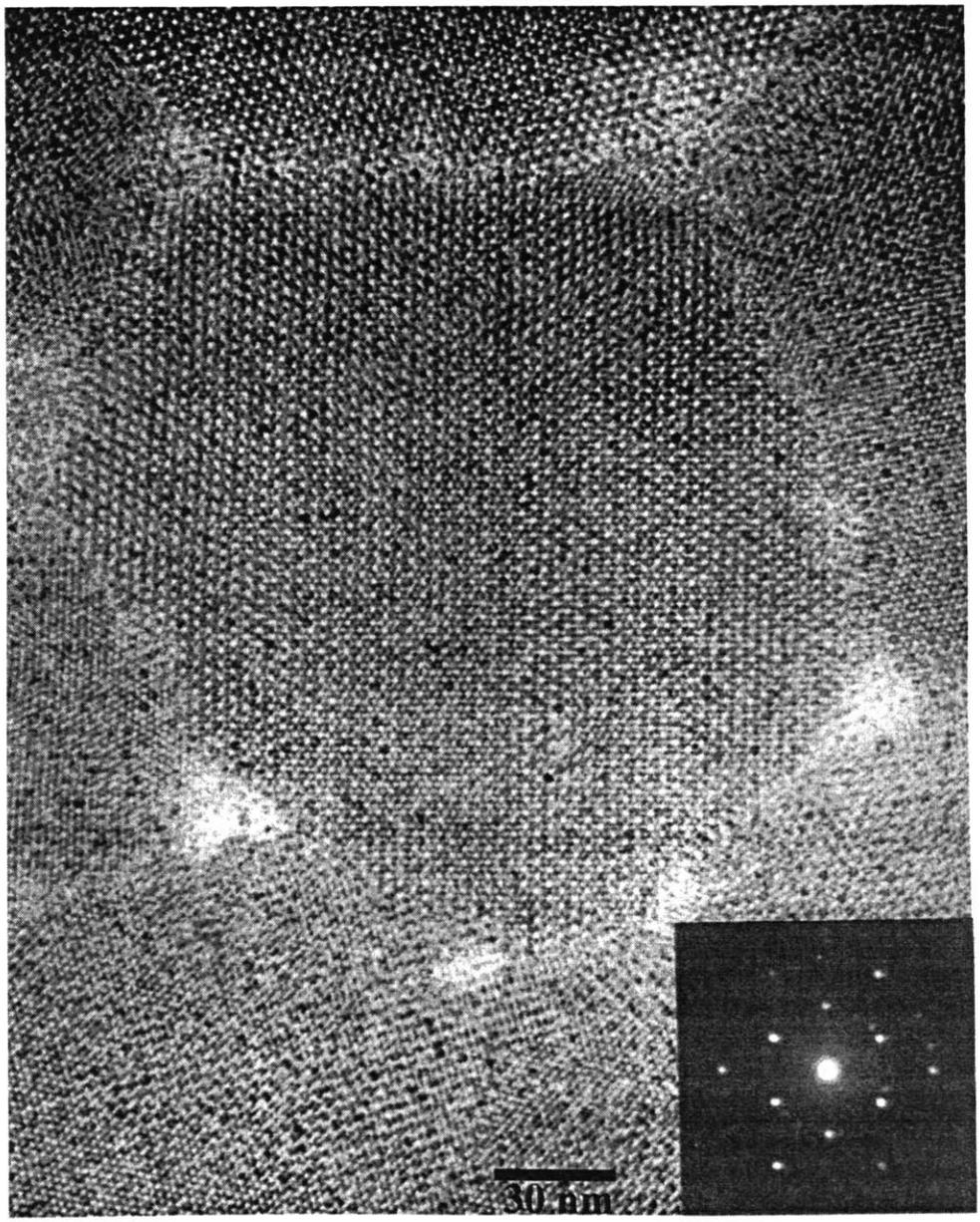

FIG. 6.13 TEM image of an epitaxial film assembled from 48Å diameter QDs. The domains in this image are each oriented with their <111> axis perpedicular to the plane of the substrate but orientation within the plane is random. Small angle electron diffraction pattern probing a 2 μm region surrounding this real space image is inset. The sharp spot pattern of the central domain is seen along with contributions from surrounding domains.

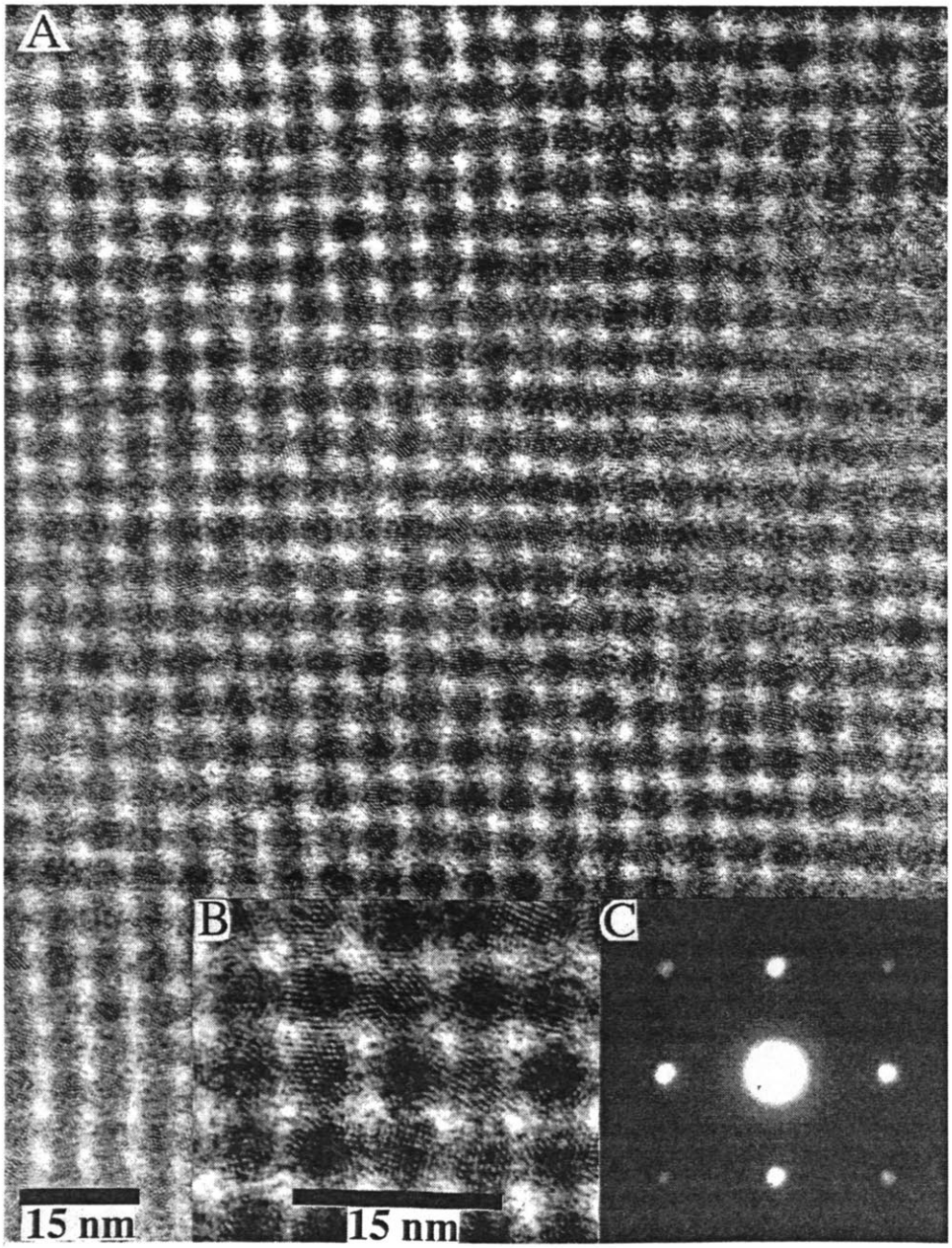

FIG. 6.14 Panel (A): TEM image of a $<100>_{SL}$ projection though a 3D superlattice of 48Å QDs. Panel (B): A high magnification image shows the internal lattice of the individual QDs. Panel (c): The small angle electron diffraction pattern demonstrates the lateral perfection of the domain.

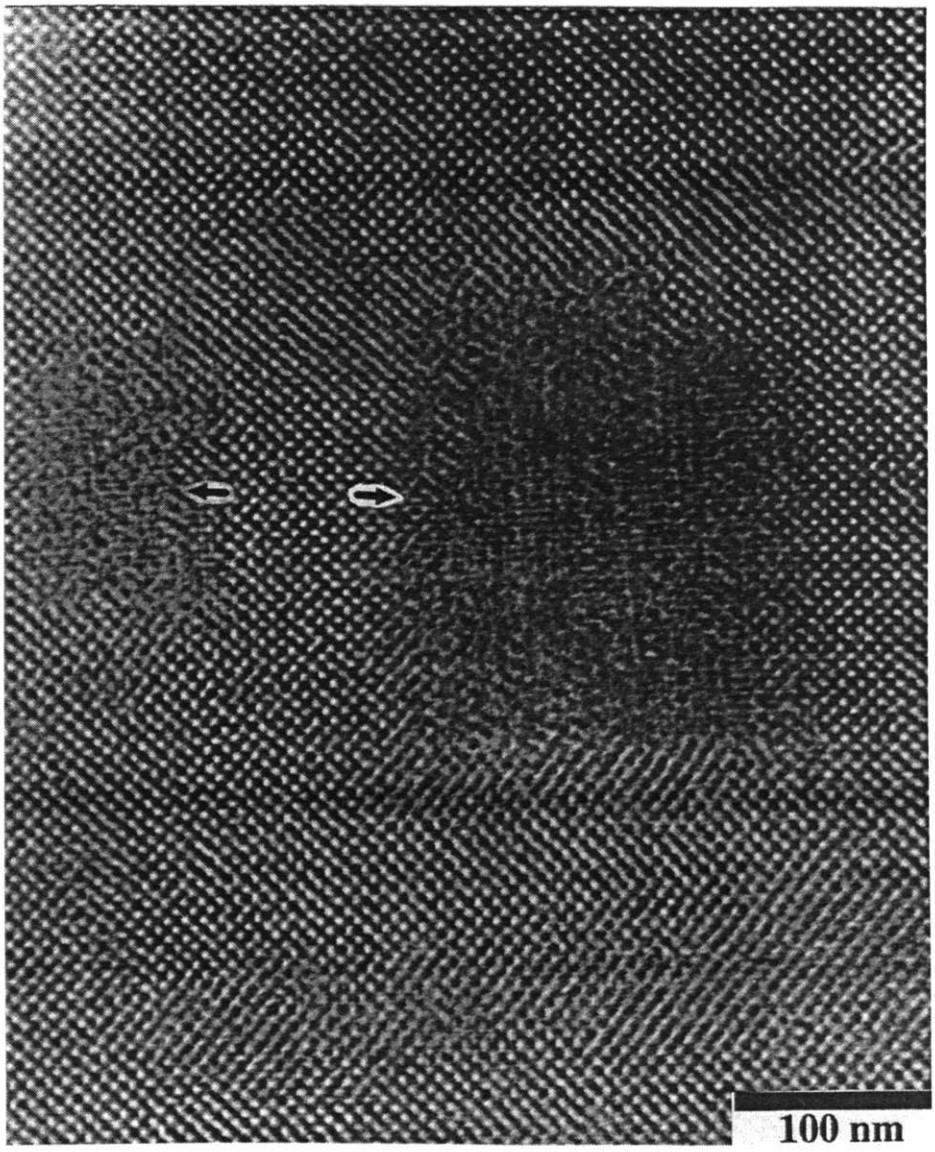

FIG. 6.15 A TEM image of a portion of a $<100>_{SL}$ projection displays the effects of heating the superlattice with the electron beam. Arrows mark the region of the superlattice that has been melted producing close packed glassy regions.

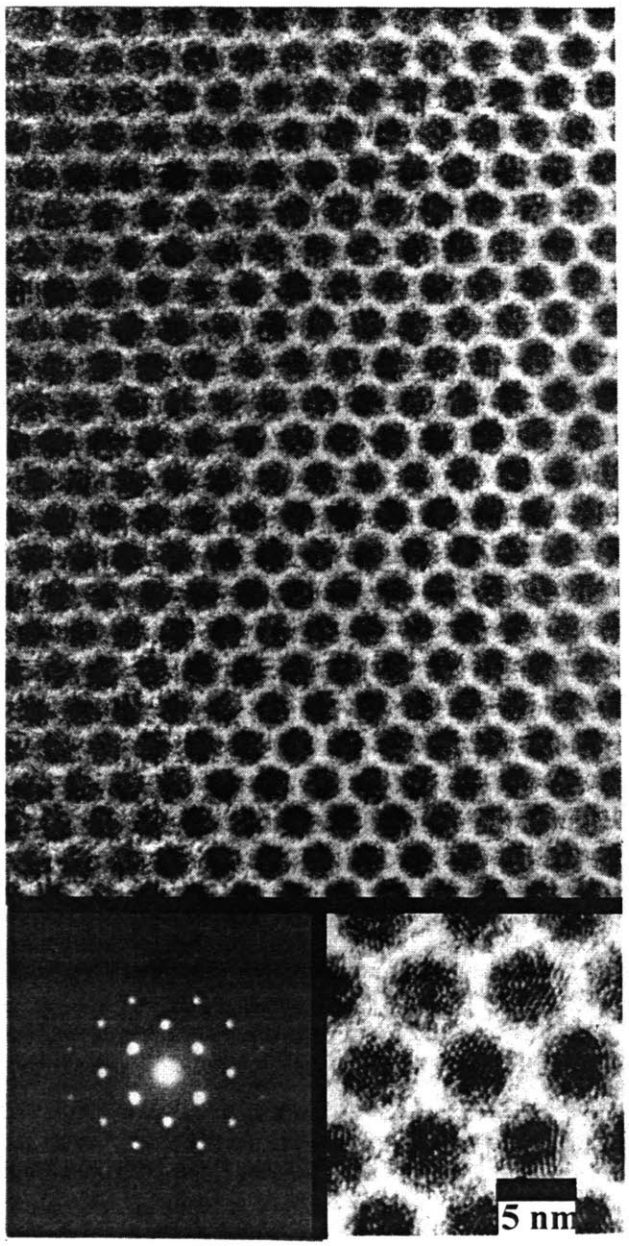

FIG. 6.17 A TEM image shows the $<101>_{SL}$ projection through a 3D superlattice of 48Å QDs. An expanded portion of this image shows the internal lattice of the individual QDs. The sharp small angle electron diffraction pattern demonstrates the lateral perfection of the superlattice.

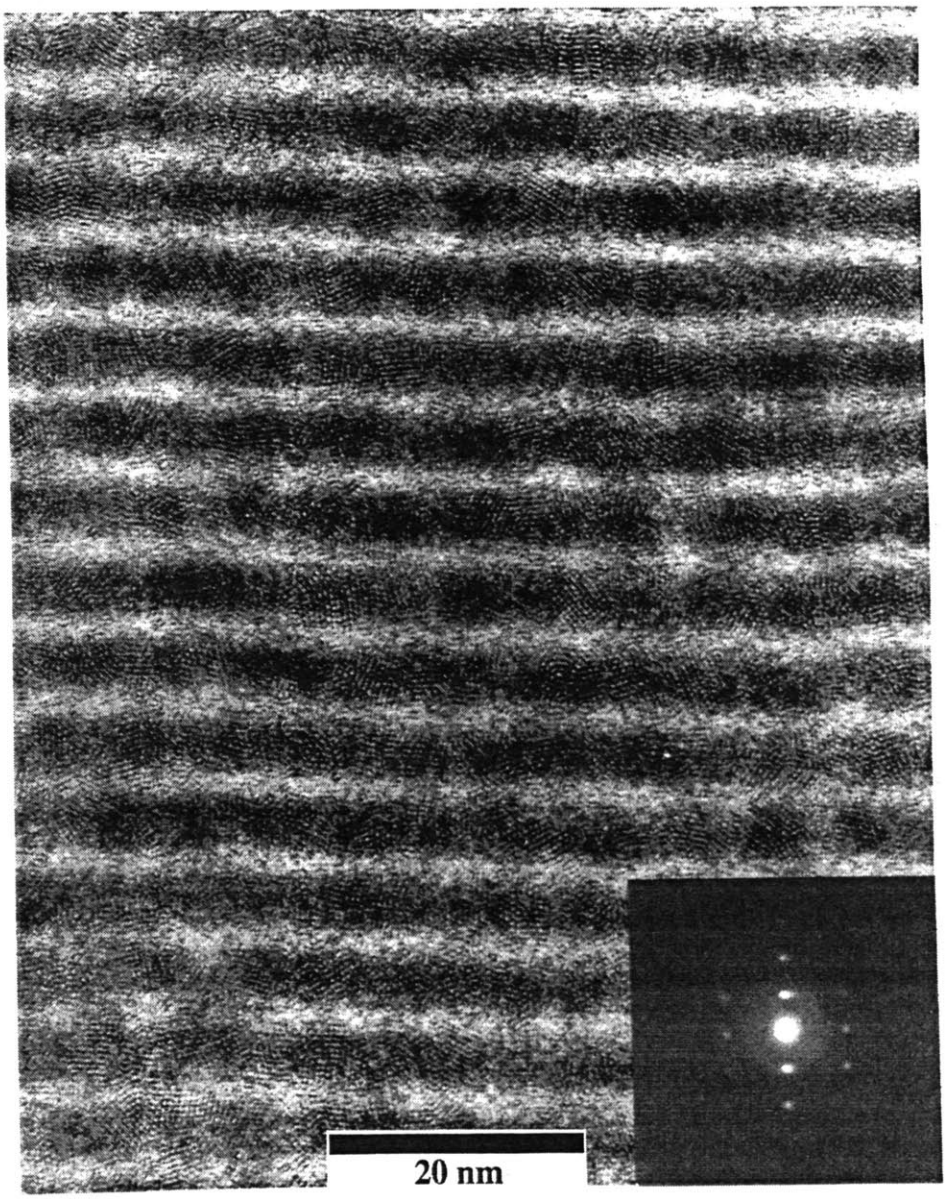

FIG. 6.17 TEM image shows the $<112>_{SL}$ projection through a 3D superlattice of 48Å QDs. The sharp small angle electron diffraction pattern demonstrates the lateral perfection of the superlattice.

These projections are summarized in figure 6.18 which displays a diagram of the 3D fcc lattice. These images are each projections through portions of a film composed of 48Å diameter particles. We prepare TEM cross sections to reveal the 3D structure of the films. Figure 6.19 shows a cross section of a $<111>_{SL}$ oriented island of 100Å diameter CdSe QDs. The film was grown on an ethylene glycol subphase and was cleaved perpendicular to the $<111>_{SL}$ to reveal the characteristic image of the $<101>_{SL}$ orientation. This clean cleavage is in stark contrast to the brittle fracture of the glassy samples.

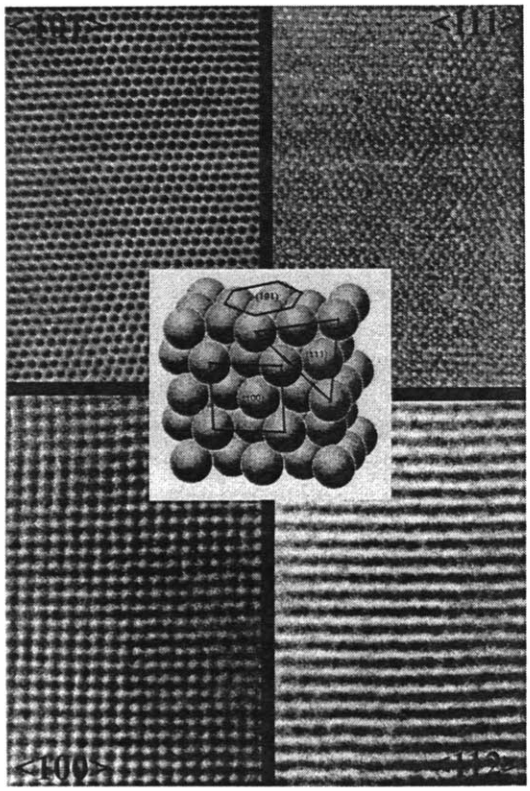

FIG 6.18 Composite of TEM images show each of the major projections through a 3D superlattice of 48Å QDs. A central schematic shows the relation of each projection to the fcc lattice.

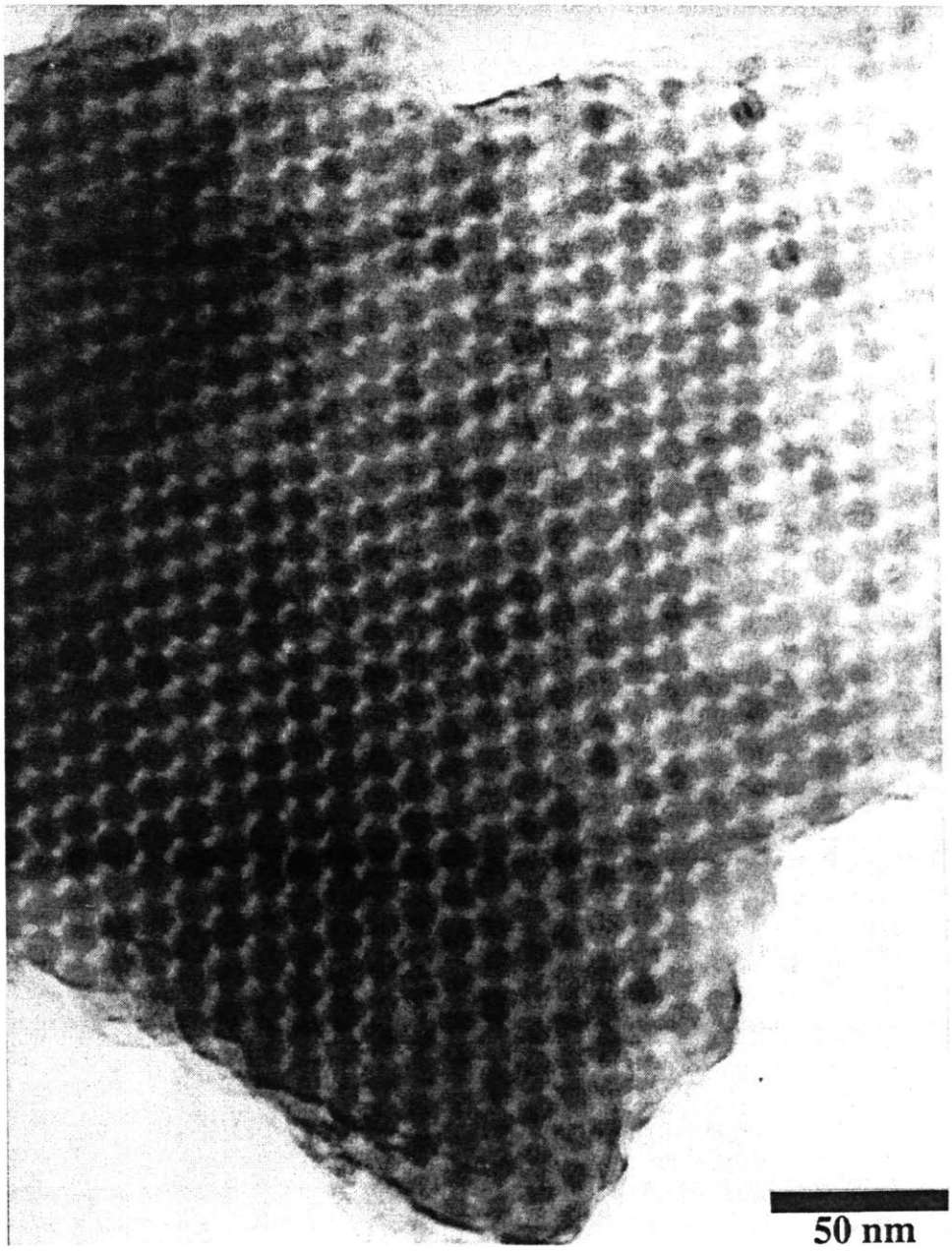

FIG. 6.19 Shows a cross-section through a $<111>_{SL}$ oriented fcc superlattice of 100Å QDs. The structure was cleaved parallel to the $(101)_{SL}$ planes and thus diplays the characteristic pattern of a <101> projection.

To develop a more precise description of the average structure in these epitaxial superlattices we return to SAXS studies. Figure 6.20A shows the sharp superlattice reflection for films assembled from a series of QD sizes. Patterns indicate a strong preferential alignment of the close packed $<111>_{SL}$ parallel to the substrate as seen in TEM surveys. Our QDs become more prolate with increasing dot size. The basic symmetry of the particles is revealed in a careful examination of the peak positions. The position of the $<111>_{SL}$ reflection corresponds to the distance expected if the major axis were oriented parallel to the substrate. In addition, shifts in the position of the $<220>_{SL}$ peak and $<311>_{SL}$ peak relative to the $<111>_{SL}$ peak show an increasing distortion of the fcc lattice with increasing size. This orientation is confirmed in wide angle X-ray studies discussed later in this chapter.

We demonstrate our control over the interdot spacing in these 3D superlattices by derivatizing a single sample of 34Å QDs with 3 different alkylphoshine capping groups. Approximately 200 mg of TOP/TOPO capped CdSe QDs were exchanged with pyridine to produce a common starting material. The pyridine capped QDs were divided into three portions and then exchanged with TCPO (curve (a)), TOPO (curve (b)) , and TBPO (curve (c)). Controlling the steric bulk of the organic capping group allows precise adjustment of the interdot spacing. Figure 6.20B displays the results with TCPO, TOPO, and TBPO providing 17Å, 11Å and 7Å spacings respectively.

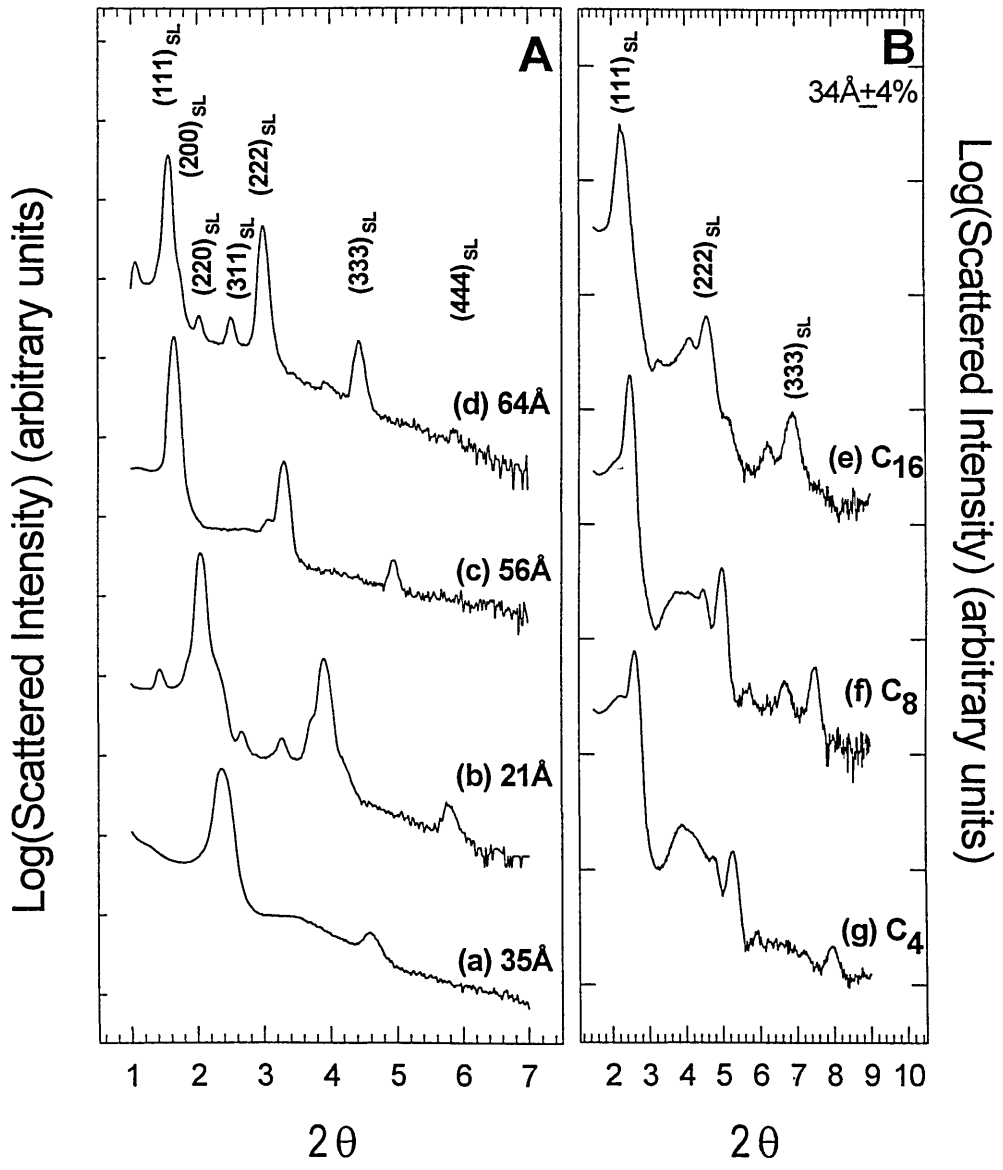

FIG. 6.20A SAXS patterns for epitaxial superlattices assembled with crystallites ranging from 35Å to 64Å in diameter. The fcc superlattice reflections are shown for the 64Å diameter sample.

FIG. 6.20B SAXS patterns for a series of epitaxial films prepared with 34Å CdSe nanocrystallites derivatized with monolayers of different chain length. The tricetylphosphate (TCPO) cap gives a ~17Å spacing (curve e), the native trioctylphospine chalcogenide caps produce a ~11Å spacing (cuve f), tributylphosphine oxide caps produce a ~7Å spacings.

6.3.6 Preferred Orientation of the QDs: During the growth of the epitaxial thin films the quantum dots align themselves with their elongated c-axis parallel to the substrate. This alignment affords the first opportunity to orient the quantum dots in the lab frame and systematically investigate their optical anisotropies as well as their fundamental optical selection rules. Figure 6.21 shows the X-ray scattering patterns for solids organized from 64Å diameter QDs. The small angle region is plotted on a log scale. Curve (a) shows the pattern for glassy thin film the WAXS portion is consistent with a randomly oriented ensemble of QDs. The epitaxial thin film shows a striking enhancement of the wurtzite $<110>_{SL}$ reflection. The intensity of the $<110>_{SL}$ reflection indicates a greater that 95% alignment of the wurtzite c-axis of the individual QDs in the plane of the substrate.

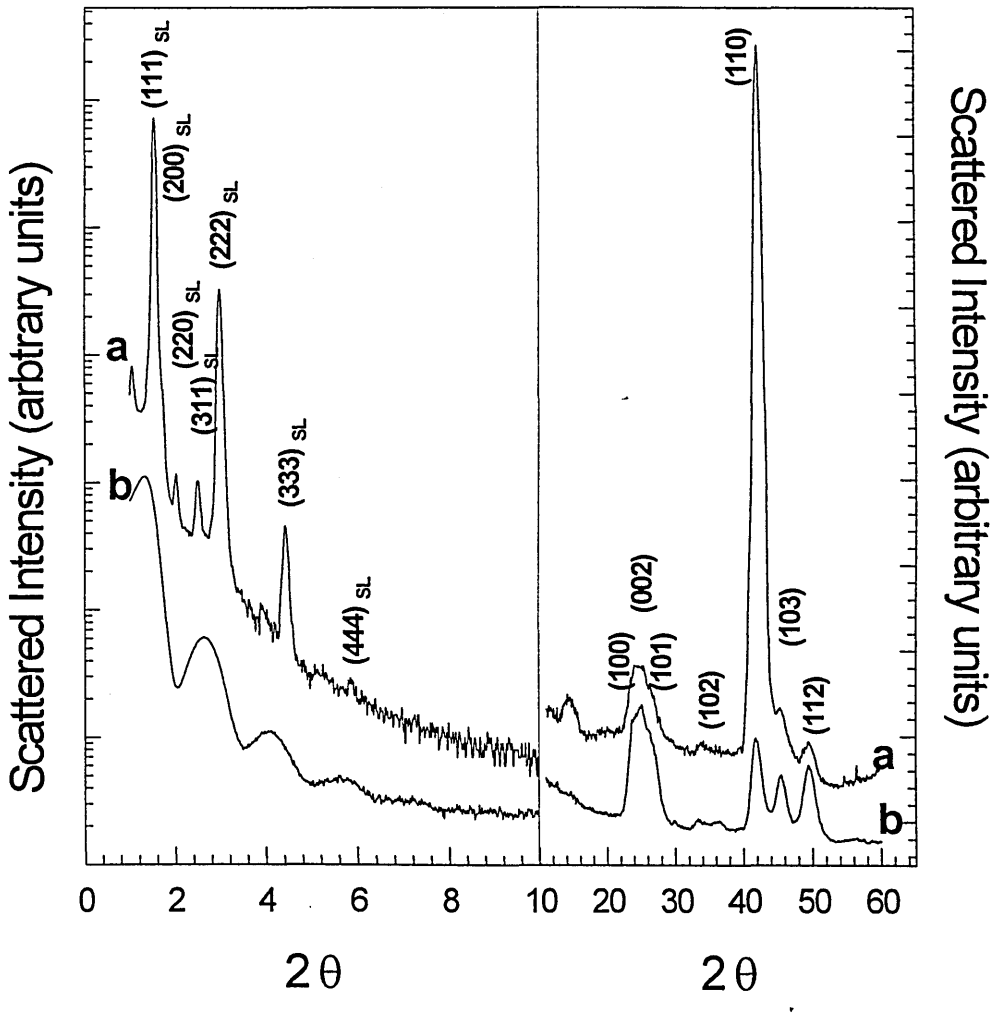

FIG. 6.21 Combined SAXS and WAXS for an oriented epitaxial film (a) and for a glassy thin film (b). Both samples were produced by deposition of 64Å QDs onto Si(100) wafers. Curve (a) the SAXS portion shows the sharp fcc superlattice reflections, while the WAX portion shows a dramatic enhancement of the wurzite <110> reflections. Greater than 95% of the QDs are oriented with their <002> axes parallel to the substrate. Curve (b) shows the characteristic pattern of a glassy solid in the SAXS region and displays a WAXS pattern consistent with the random orientation of the individual crystallites.

The TEM image in figure 6.22 shows even more precise alignment of the QDs. This image shows a projection along the $<111>_{SL}$ of the superlattice of 64Å QDs grown epitaxially on a TEM grid. Clearly visible columns of atoms produce a fine cross-hatched pattern throughout the image. Columns of Cd and Se atoms in a given QD are coherent with those of neighboring QDs. The internal lattice of the QDs and the superlattice are coherent for the 4 planes under observation. This small portion of the epitaxial film is a crystal with over 40,000 atoms in each unit cell of the superlattice. The alignment of the <002> axis of crystallites parallel to the substrate enhances the intensity of the <002> reflection seen in panel B. Hexagonal modulation of the ring intensity is due to the coherent alignment of the individual QD's wurtzite lattice with the fcc superlattice. A blowup of the central beam at lower flux shows the small angle electron diffraction pattern emerging. Panel C shows the electron diffraction pattern of a glassy film prepared from the same sample of QDs and displays the uniform wurtzite ring pattern of an isotropic distribution of QDs. X-ray investigations of single superlattice domains are being pursued to provide a more definitive structure.

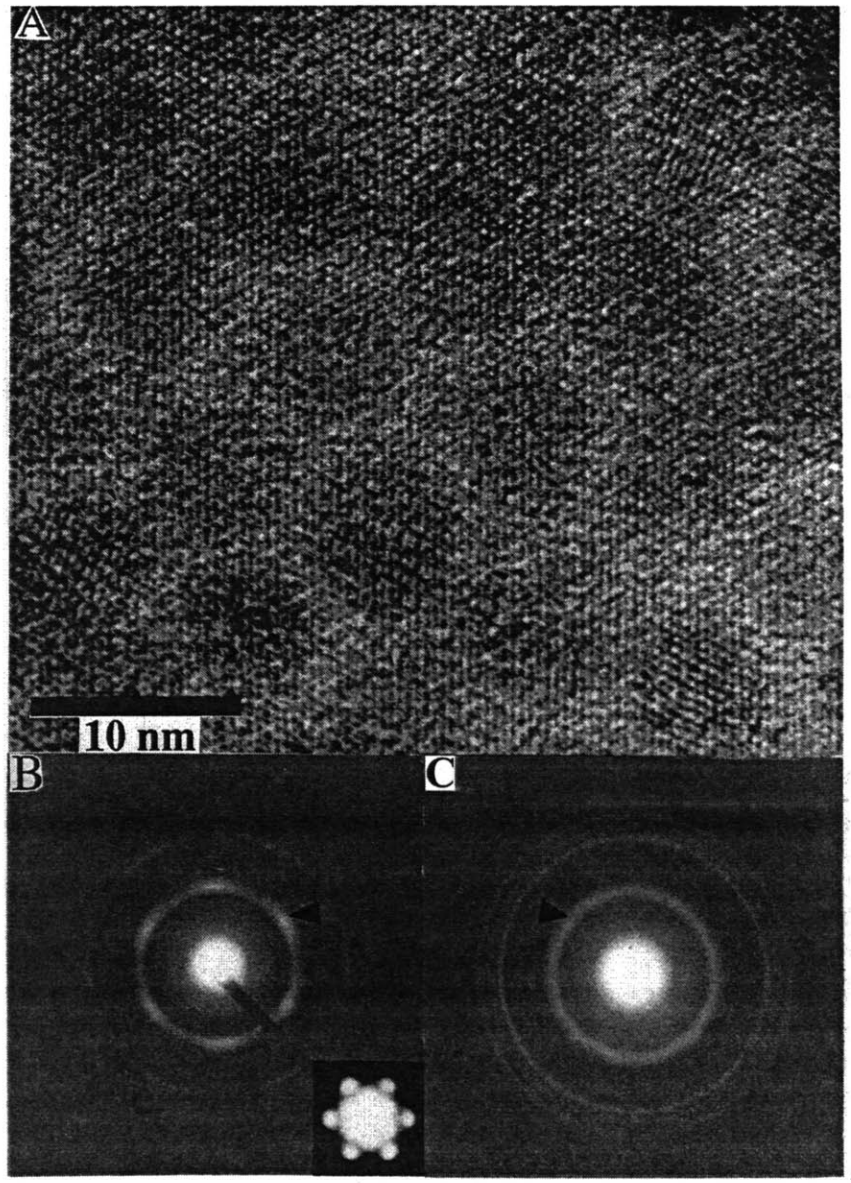

FIG. 6.22 A HRTEM image shows a portion of a $<111>_{SL}$ oriented superlattice of 62Å QDs. The periodic dot pattern running thoughout this image is the coherent image of the columns of Cd and Se atoms in different QDs. Each QD is aligning with the superlattice and the result is a coherence of the atoms in the various layers of QDs. This aligned portion of the sample is a molecular crystal with over 40000 atoms in a unit cell. Panel B shows the wide electron diffraction pattern of an area ~2 μm surrounding the real space image. Strong modulation of the diffraction pattern results from the preferred alignment of the individual crystallite axes with the axes of the superlattice. At lower flux the small angle electron diffraction pattern can be seen to be emerging from the central beam. Panel C shows the unmodulated wide angle electron diffraction pattern of a glassy prepared from the same initial sample.

6.4 References:

(1) T. Takagahara, Optoelectro.--Devices Technol. 8, 545 (1993).

(2) T. Takagahara, Surf. Sci. 267, 310 (1992).

(3) Y. Kayanuma, J. Phys. Soc. Japan 62, 346 (1993).

(4) D. Heitmann and J. P. Kotthaus, Physics Today 46,56 (1993).

(5) (a) B. O'Regan and M. Graetzel, Nature 353, 737 (1991). (b) M. Nazeerudin, A Kay, I. Robicio, R. Humphry-Baker, E. Muller, P. Liska, N. Vlachopoulos, and M. Graetzel, J. Am. Chem. Soc. 115, 6382 (1993).

(6) (a) L. Spanhel and M. A. Anderson, J. Am. Chem. Soc. 112, 2278 (1990). (b) L. Spanhel and M. A. Anderson, J. Am. Chem. Soc. 113, 2826 (1991).

(7) T. Vossmeyer, L. Kasikas, M. Giersig, I. G. Popovic, K. Diesner, A. Chemsedine, A. Eychmuller, and H. Weller, J. Phys. Chem. 98, 7665 (1994).

(8) G. D. Stucky and J. E. Mac Dougall, Science 247, 670 (1990).

(9) B. O. Daboussi, C. B. Murray, M.F. Rubner and M.G. Bawendi, Chem. Mater. 6, 217 (1994).

(10) N. Herron, J. C. Calabrese, W. E. Farneth, and Y. Wang, Science 259,1426 (1993).

(11) M. D. Bentzon, J. van Wonterghem, S. Morup, A. R. Tholen, and C. J. W. Koch, Phil. Mag. B. 60, 169 (1989)

(12) M. D. Bentzon and A. R. Tholen, Ultramicroscopy 38, 105 (1991).

(13) (a) P. Pieranski, Comp. Phys. 25, 25 (1983). (b) C. A. Murray and D. G. Grier, American Scientist 83, 238 (1995).

(14) J.V. Sanders, Acta. Cryst. A24, 427 (1967).

(15) J. W. Goodwin and R. Buscall, Colloidal Polymer Particles (Academic Press, Boston, 1995) Chapter1.

(16) (a) P. N. Pusey, W. van Megen, P. Bartlet, B. J. Ackerson, J. G. Rarity and S. M. Underwood, Phys. Rev. Lett. 63, 2753 (1989). N. A. Clark, A. J. Hurd and B. J. Ackerson, Nature 281, 57 (1979).

(17) C. R. Kagan, C. B. Murray, and M. G. Bawendi (submitted).

(18) J. W. Goodwin, Colloidal Dispersions (The Royal Society of Chemistry, London 1981) Chapter 9.

(19) H. P. Klug and L. E. Alexander, X-ray Diffraction Procedures Second Edition, (Wiley, New York 1974) Chapter 11.

(20) S. A. Majetich, A. C. Carter, R. D. Mccullough, J. Seth, and J. A. Belot, Z. Phys. D. 26, s210 (1993).

Conclusions

We have developed general methods for the preparation and systematic characterization of high quality nanocrystalline systems. To distinguish true size dependent evolution from simple sample inhomogeneities and defects, we have produced a series of homologous samples spanning the size range of interest. Each sample is monodisperse to the limit of atomic roughness and thus the ensemble average of the properties observed is representative of the properties of each individual crystallite. We have systematically synthesized and characterized samples with a combination of chemical and structural probes. The results of these independent investigations have been compared with simple computer models, thus assuring a self-consistent description of the material. General procedures have allowed us to describe the structure and properties of these mesoscopic structures with precision comparable to many conventional macromolecules.

We have organized tailored nanocrystallites into solid superstructures while maintaining and enhancing their novel mesoscopic properties. We have overcome several formidable practical challenges. The materials produced display mesoscopic phenomena at room temperature. They are chemically and mechanically robust and are produced at low cost. We combine the versatility and precision of organometallic synthesis with the established methodology of colloidal self-organization to meet these strict tolerances.

This work has united concepts from organometallic synthesis, classic colloidal science and low dimensional physics to produce a fundamentally new class of opto-electronic materials.

Acknowledgment

This thesis is an important milestone in my journey to become a scientist. From the age of ~2 years a small cloth bag and its mysterious contents became my constant companion. This was my "invention bag". From its treasured bits of string, discarded paper, elastic bands and pieces of wood a new project would rise to fill each day with wonder. The support of many caring people has allowed me to live a life filled with that same sense of wonder and discovery. The greatest reward I have known in my life has been the company of teachers, coworkers, friends and family who truly appreciated good ideas.

I could not have reached this milestone without the support of dedicated instructors and mentors. Sister Carol saw beyond the difficulties of forming letters on a page. Jessie Johnson taught me organize my ideas in a story with a clear purpose and a gave me respect for the importance of context. Alec Hardy showed me that the intellectual and emotional rewards of solving a few difficult problems could be far greater than solving many simple ones. For 3 years Dr. John Young was my advisor and my mentor. He graciously allowed his lab at Saint Mary's to be my invention bag and engrained in me his engineering ethic that a job is not complete until the answer is simple, reliable, and inexpensive.

The support and encouragement of my thesis advisor Moungi Bawendi made this work possible. I have begun my scientific career with the guidance of Moungi's crisp ideas, clear goals, and his respect for originality. From the earliest days, his intellectual strength was tempered with inexhaustible patience to give his research group a sincere sense of purpose and cooperation. He has shown me that individuals with diverse talents can be united by good ideas and personal vision to answer important questions. To me this is the essence of a strong research group.

In my studies have worked with many talented people. All who helped me to move forward have earned my respect and my gratitude. Thanks to David, Manoj, Ann, Cherie, Bashir, Ken and Fred for reaching out steady me when my footing was unsure. David and Manoj, your support was critical in that first year when I was uncertain if "I

should be here at all". Cherie and Ann, you offered the professional strength and personal friendship that sustained me when I was certain "I should not be here any longer". Michael and Lino, it was a pleasure to work with and to learn from each of you. Ken, Fred, and Steve; your talents make me optimistic about future of the group. This faith in the future gives me peace as I leave.

Friendship is one life's greatest gifts. Ted, Marc, David, and Cherie your contributions to my time here have been immeasurable. I will celebrate our common adventures and memories long after this document ceases to see the light of day.

3288-48